# Parametric Instabilities in U.V. Laser-Produced Plasmas

K. Tanaka

Report No. 133
July 1982

## ABSTRACT

Parametric instabilities in UV laser matter interaction experiment were investigated, measuring scattered light from target plasmas. Experiments were classified into two categories: (A) time integrated spectroscopic measurement of the scattered light from parametric instabilities at and below quarter critical density, (B) temporally and spectrally resolved measurement of the scattered light from instabilities at/or below critical density.

Both types of experiments were conducted with the single beam UV laser at $\lambda_L$ = 0.351 μm. On-target intensities ranged from $10^{13}$ to $3 \times 10^{15}$ W/cm$^2$ with 100 and 450 psec pulses. Planar type targets of CH, Ni, and Au were used.

(A). For the first time, spectroscopic measurements between 4000 and 7000 Å clearly differentiated the threshold and saturation behavior between the absolute and convective Raman as well as the two plasmon ($2\omega_{pe}$) instabilities. The observed equal threshold values for the absolute and convective Raman instabilities implied density profile steepening near $n_c/4$ ($n_c$ : critical density). Suppression of the convective Raman instability from 0.2 to 0.25 $n_c$ became clear from comparison between the observed and the model spectra, supporting the

argument of density steepening.

(B). Two spectral components were identified for the scattered light around the laser wavelength. With a target tilted more than $20^{o}$, the backscattered light contained a non-specular component, typically showing increasing spectral shift toward the longer wavelength side with a larger target angle. Strong collimation of this light was observed as well. Both characteristics were indicative of stimulated Brillouin scattering (SBS). From the spectral shift dependence of the SBS component on target angle, the background temperature of 1 - 2 keV from a near sonic plasma flow was deduced. SBS accounted for 1/3 of the total backscattered enegy at normal incidence. Specular components showed large spectral broadening above a certain laser intensity, but no such collimation as SBS was observed. Modulational instability was proposed to explain this component. Observed threshold and spectral broadening near the threshold intensity agreed with linear theory in a homogeneous plasma.

## PUBLICATIONS

The following paper related to this study has been accepted for publication.

" Stimulated Raman Scattering from U.V. Laser-Produced Plasmas." to be published in the Apr. 1982 issue of Physical Review Letters.

K. Tanaka, L. M. Goldman, W. Seka, M. C. Richardson,
E. A. Williams, J. Soures
Laboratory for Laser Energetics, University of Rochester,
Rochester, N.Y., 14623.

The following papers have been published in this study.

"Observations of Brillouin Sidescatter in Laser-Produced Plasmas." Phys. Rev. Lett. 45, 1558(1980)

Kazuo Tanaka and Leonard M. Goldman
Laboratory for Laser Energetics, University of Rochester,
Rochester, N.Y., 14623.

" Search for Shell Disintegration in Laser Implosion Experiments "

Appl. Phys. Lett. 35, 853(1979)

K. Tanaka and E. I. Thorsos

Laboratory for Laser Energetics, University of Rochester,

Rochester, N.Y., 14623.

TABLE OF CONTENTS

TABLE OF CONTENTS (continued)

TABLE OF CONTENTS (continued)

## LIST OF TABLES

## LIST OF FIGURES

LIST OF FIGURES (continued)

LIST OF FIGURES (continued)

# I. INTRODUCTION

As a possible sourse of inexhaustible energy, controlled thermonuclear fusion may be of critical importance. There are two approaches proposed for controlled fusion. One is magnetic confinement fusion(MCF), and the other, inertial confinement fusion (ICF). While MCF is characterized by continuous mode operation and a large confinement device, ICF has a pulse mode operation and requires the burning of (D,T) fuel within the time of target disassembly. This is only possible if the densities are high enough (.2-2 $g/cm^2$)[1,2,3] to give rapid burn. Processes in laser driven fusion may be classified as follows:

(1) Absorption: laser light is coupled into a spherical target surface through different absorption mechanisms.

(2) Energy transfer: target surface is ablated by absorbed energy. The residual target wall starts moving inward, compressing the inside fuel as a repulsion force of ablation.

(3) Thermo-nuclear burn: the compression creates very high densities and temperatures and the thermo-nuclear reaction[4] takes place.

Presented in this thesis is a discussion of parametric instabilities. These instabilities impact the first category above, since most instabilities occur through laser plasma coupling in underdense plasmas. Parametric instabilities, if they were efficient, could significantly affect the consecutive processes such as coupling of laser light, energy transfer, and compression.

A key to the success of ICF is the efficient coupling of laser light to the target. That is, the laser energy should be absorbed such as to generate a thermal plasma. Collisional absorption, for example, generates such a plasma, which contributes to the compression efficiently. In contrast, non-thermal ions and electrons work detrimentally for the compression. As the momentum for compression is inversely proportional to the ion velocity for constant absorbed energy, high speed non-thermal ions transfer less momentum compared to thermal ions, while energy carried away by non-thermal ions goes with the velocity squared. Thus the presence of non-thermal ions of high energy decreases the compression hydrodynamic efficiency. Resonance absorption was shown to generate supra-thermal electrons of long mean free paths through wave-breaking of electrostatic waves excited at the critical density.[60] These hot electrons may penetrate and preheat a target core before compression is completed.[5,6] They are believed to play a dominant role in the explosive type compression experiments of laser wavelengths longer than 1 um with short pulses (~100 ps), and high intensities ($10^{15}$ - $10^{16}$ W/cm$^2$).[7] Because supra-thermal electrons preheat the inside of the target and carry away significant amounts of

the absorbed energy, the explosively driven targets can not reach high enough core density. If a inward-moving target wall is driven by ablating outer surface material instead of being imploded by impulsed pressure in exploding mode, higher compression is possible. This is a so called ablatively driven compression, which may be achieved with long pulses(~ns) and with thicker target wall.[8,9]

An important absorption mechanism in the ablative type of compression is collisional absorption. The long density scale lengths expected for plasmas made with long laser pulses give favorable conditions for the collisional absorption, since this absorption increases exponentially with density scale length. The higher critical density of the plasma created by a sub-micron wavelength laser looks attractive compared to longer wavelength lasers($\geqslant 1$ μm), since the collisional frequency is proportional to the electron density. Resonance absorption, in turn, may become less important in a plasma of long density scale lengths, both because the longer distance between the turning point and the critical density point gives a weaker resonantly driven electrostatic field and because collisional absorption may reduce the amount of light reaching to the turning point.[9,10]

Thus collisional absorption is likely to be a dominant absorption process for short wavelength laser experiments with long pulses, while long wavelength laser experiments with short pulses have shown resonance absorption as a major absorption mechanism.[7] In fact, experiments with sub-micron wavelength laser demonstrated the expected higher absorption

due to collisional absorption.[11] As a consequence of the collisional absorption processes, fewer fast ions and a small amount of super-hard x-ray component from hot electrons were detected in the same experiment.[12]

However, when a large underdense region is formed by a long pulse ( ~ns), the interactions between laser light and the underdense plasma start to play a significant role. These are called parametric instabilities. In these instabilities, an incident electromagnetic (EM) wave parametrically decays into several possible combinations of EM waves and electron plasma (EP) waves, and ion acoustic (IA) waves. In the case of stimulated Brillouin scattering, which has been named in analogy with terminology from molecular physics, incident EM wave decays into a scattered EM wave and an IA wave. Collective stimulated Brillouin scattering (SBS) might turn a plasma into a mirror, reducing absorption drastically, since the scattered photon energy is about equal to the original photon energy (only differing by an IA frequncy of $10^{-3}$; see Chap. II, p. 24.) Study of the SBS has been conducted extensively for the last several years, and numbers of reports have been published.[13-44] From 1.05 μm laser-produced plasmas, we observed more than 50 % of the light incident on target could be reflected out by SBS, when pre-plasmas were made before a main pulse.[43] Almost 100 % reflection of 10.6 μm laser light due to SBS was reported for very long scale length plasmas.[44]

In stimulated Raman scattering, the incident EM wave decays into a scattered EM wave and an EP wave. Stimulated Raman scattering (SRS) can take place at and below quarter critical density, where the frequency matching condition is satisfied. SRS may have the potential to produce supra-thermal electrons. The generation of these electrons results from Landau damping or wavebreaking of the resonantly driven electron plasma waves by SRS. Supra-thermal electrons with energies of several tens of keV can be produced.[45] D.W. Phillion and D.L. Banner[46] observed SRS with strong polarization dependence in 1.06 μm and 0.53 μm laser experiments. R.G. Watt, R.D. Brooks, and Z.A. Pietrzyk[47] reported SRS of $CO_2$ laser light from underdense plasmas formed in a solenoid.

Two plasmon ($2\omega_{pe}$) decay instability, where the incident EM wave decays into two EP waves, is similar to SRS, but is unstable at $n_c/4$ only. Hot electrons from this instability were reported recently in a 10.6 μm laser experiment with the characteristic distribution anisotropy.[48]

In this thesis, these parametric processes in U.V. laser-produced plasmas are investigated. Especially we emphasize two categories:

(1) SRS and $2\omega_{pe}$ instabilities whose scattered light spectra arise between $2\lambda_L$ and $\lambda_L$ ($\lambda_L$: laser wavelength).

(2) SBS and modulational instabilities whose spectra are limited in the vicinity of $\lambda_L$.

Experiments were conducted with $\lambda_L$= 0.351 μm light produced by up-converting a 1.054 μm glass laser output using two TYPE II KDP

crystals. Planar CH, Ni and Au targets were irradiated with 450 psec pulses at intensities between $10^{13}$ and $3 \times 10^{15}$ W/cm$^2$ .

The results of the study can be summarized as follows:

(1) Spectrally resolved measurements between 4000 and 7500 Å have been made of back- and side- scattered light from laser-produced plasmas. The first clear evidence is found of threshold and saturation behavior for both the absolute and convective Raman instabilities as well as the $2\omega_{pe}$ instabilities. Density steepening at $n_c/4$ is suggested from the relative thresholds of absolute and convective Raman instabilities.

(2) Back- and specularly- reflected light around the laser frequency has been measured in time and spectrum. Our results are consistent with a hypothesis that attributes the fairly large blue shifted broadening (~9 Å) to a combination of Doppler effect and modulational instability. When the laser incidence angle was increased, a larger red shift (~3 Å) was observed in the backscattered light. This red shift suggests SBS, whose amount is estimated to be approximately 1/3 of the whole backscattered energy. The maximum of backscattered intensity occurred at the time of incident pulse peak.

In Chapter II, we briefly discuss the theory of parametric interactions, including SBS, SRS, $2\omega_{pe}$ and modulational instabilities. In Chapter III, the laser and experimental system is described as well as experimental procedures. In Chapter IV, detailed results are reported followed by a discussion.

## II. THEORY OF PARAMETRICALLY COUPLED WAVE-WAVE INTERACTION.

### A. GENERAL TREATMENT OF EQUATION.

The object, here, is to present brief procedures for deriving the dispersion equations and, from these, the thresholds of parametric instabilities. The linear and non-linear treatments of these equations can be found extensively in the literature.[49 - 58] The set of equations describing parametric instabilities consists of Maxwell's equations, and the first (continuity) and second (momentum) moment equations of the Vlasov equation. The following equations are used to describe wave-wave interaction.

$$\frac{\partial n_e}{\partial t} + \nabla\cdot(n_e \underline{v}_e) = 0 \qquad (1)$$

$$\frac{\partial \underline{v}_e}{\partial t} + (\underline{v}_e\cdot\nabla)\underline{v}_e + \frac{\gamma_e T_e}{n_e m_e}\nabla n_e + \nu_{ei}(\underline{v}_e - \underline{v}_i) = -\frac{e}{m_e}(\underline{E} + \frac{\underline{v}_e}{c}\times\underline{B}) \qquad (2)$$

$$\frac{\partial n_i}{\partial t} + \nabla\cdot(n_i \underline{v}_i) = 0 \qquad (3)$$

$$\frac{\partial v_i}{\partial t} + (\underline{v}_i\cdot\nabla)\underline{v}_i + \frac{\gamma_i T_i}{n_i m_i}\nabla n_i + \frac{m_e}{m_i}\nu_{ei}(\underline{v}_i - \underline{v}_e) = \frac{e}{m_i}(\underline{E} + \frac{\underline{v}_i}{c}\times\underline{B}) \qquad (4)$$

$$\nabla\times\underline{E} = -\frac{1}{c}\frac{\partial \underline{B}}{\partial t} \qquad (5)$$

$$\nabla \times \underline{B} = \frac{4\pi}{c}\underline{J} + \frac{1}{c}\frac{\partial \underline{E}}{\partial t} \qquad (6)$$

Here C.G.S. (Gaussian) units are used. Equations (1) and (3) are the continuity equations, and Eqs. (2) and (4) are the momentum equations for electrons and ions with the use of $Pn^{\gamma} = \text{const.}$ (P: pressure, n: density), respectively.

$$n_e(n_i), \quad \underline{v}_e(\underline{v}_i), \quad \gamma_e(\gamma_i), \quad T_e(T_i)$$

represent the density, the velocity, the ratio of specific heats, the temperature of electrons (ions). $\nu_{ei}$ is the electron-ion collisional frequency. Equations (5) and (6) are Maxwell's equations. The electron density is assumed to have a steady state value and a first order perturbed term:

$$n_e = n_0 + n_{e_1} \qquad (7)$$

The current is thus defined by

$$\underline{J} = -e\underline{v}_e(n_0 + n_{e_1}) \qquad (8)$$

where only the perturbed electron velocity is considered. For electromagnetic (EM) waves, taking the time derivative of Eq. (6) and curl of Eq. (5) and combining the two give

$$\frac{\partial^2 \underline{E}_T}{\partial t^2} + c^2\nabla\times(\nabla\times\underline{E}_T) - 4\pi n_0 e\frac{\partial \underline{v}_e}{\partial t} - 4\pi e\frac{\partial}{\partial t}(n_{e_1}\underline{v}_e) = 0 \qquad (9)$$

Ion motions are neglected, as Eq. (7) contains a high frequency component, at which the ion can not respond due to its heavy mass.

Combining Eqs. (2) and (7) with $\nabla \cdot \underline{E}_T = 0$, we have

$$\frac{\partial^2 \underline{E}_T}{\partial t^2} - c^2 \nabla^2 \underline{E}_T + \omega_{pe}{}^2 \underline{E}_T = -4\pi n_0 e (\underline{v}_e \cdot \nabla) \underline{v}_e$$

$$- \frac{\omega_{pe}{}^2}{c} (\underline{v}_e \times \underline{B}) + 4\pi e \frac{\partial}{\partial t} (n_{e_1} \underline{v}_e) + \frac{4\pi e \gamma_e T_e}{n_0 m_e} n_{e_1} \nabla n_{e_1} + i \frac{\omega_{pe}{}^2}{\omega_L} \nu_e \underline{E}_T \qquad (10)$$

where $\omega_{pe}{}^2 = \dfrac{4\pi n_0 e^2}{m_e}$ is the square of unperturbed electron plasma frequency.

The right hand side (RHS) includes a non-linear convective term, a Lorentz term, a non-linear current term, a thermal pressure term, and a collisional term. If we neglect all non-linear terms on the RHS, the normal dispersion relation of EM waves in plasmas is obtained.

For electron plasma (EP) waves, Eqs. (1) and (2) with the same procedure give

$$\frac{\partial^2 n_{e_1}}{\partial t^2} - \frac{\gamma_e T_e}{m_e} \nabla^2 n_{e_1} + \omega_{pe}{}^2 n_{e_1} =$$

$$\nabla \cdot \left\{ \frac{\gamma_e T_e}{n_0 m_e} n_{e_1} \nabla n_{e_1} - n_0 (\underline{v}_e \cdot \nabla) \underline{v}_e - \frac{n_0 e}{c m_e} (\underline{v}_e \times \underline{B}) + \frac{\partial}{\partial t} (n_{e_1} \underline{v}_e) \right\} - \nu_e \frac{\partial n_{e_1}}{\partial t} \qquad (11)$$

For ion acoustic (IA) waves, linearizing Eqs. (3) and (4) with $n_i = n_{io}$ (steady term) + $n_{i1}$ (perturbed term), we obtain a linearly coupled equation of ions and electrons on a slower time scale,

$$n_{e_1}^s = \left(1 - \frac{\omega_{IA}^2}{\omega_{pi}^2}\right) n_{i_1}^2 \qquad (12)$$

where $\omega_{IA}$ is the IA frequncy, whose dispersion relation is going to be derived, and $\omega_{pi} = \left(\frac{4\pi n_o e^2}{m_i}\right)^{1/2}$ is the ion plasma frequency. The superscript s denotes the low frequency component. Since ions can respond linearly to electrons as seen in Eq. (12), we can use electrons on the slower time scale for ion motion ($\omega_{IA} << \omega_{pi}$) From Eqs. (1), (2) and Poisson's equation for low frequency terms,

$$\nabla \cdot \underline{E}^s = 4\pi e \left(n_{i_1}^s - n_{e_1}^s\right) \quad , \qquad (13)$$

we obtain

$$\frac{m_i}{m_e} \frac{\partial^2 n_{e_1}^s}{\partial t^2} - \gamma_e \frac{v_{Te}^2}{m_e} \nabla^2 n_{e_1}^s = -\nabla \cdot \left\{ \frac{\gamma_e T_e}{n_o m_e} n_{e_1}^s \nabla n_{e_1}^s \right.$$

$$\left. - \frac{n_o e}{c m_e} (\underline{v}_e \times \underline{B}) - n_o (\underline{v}_e \cdot \nabla) \underline{v}_e + \frac{\partial}{\partial t} (n_{e_1}^s \underline{v}_e) \right\} - \nu_e \frac{\partial n_{e_1}^s}{\partial t} \qquad (14)$$

Here Eq. (11) and $\frac{\omega_{IA}^2}{\omega_{pi}^2} \ll 1$ are used. Simply multiplying Eq. (14) by $m_e/m_i$, leads to

$$\frac{\partial^2}{\partial t^2} n_{e_1}^s - c_s^2 \nabla^2 n_{e_1}^s = -\frac{m_e}{m_i} \nabla \cdot \left\{ \frac{\gamma_e T_e}{n_o m_e} n_{e_1}^s \nabla n_{e_1}^s \right.$$

$$\left. - \frac{n_o e}{c m_e} (\underline{v}_e \times \underline{B}) - n_o (\underline{v}_e \cdot \nabla) \underline{v}_e + \frac{\partial}{\partial t} (n_{e_1}^s \underline{v}_e) \right\} - \frac{m_e}{m_i} \nu_e \frac{\partial}{\partial t} n_{e_1}^s \qquad (15)$$

where $C_s = \left(\frac{\gamma_e T_e}{m_i}\right)^{1/2}$ is the ion sound speed. The normal dispersion

relation for the acoustic waves is acquired by taking the LHS = 0. Now with the three Eqs. (10), (11), and (15), parametric coupling of waves can be described.

## B. STIMULATED RAMAN SCATTERING (SRS).

### 1. SRS in Homogeneous Plasmas.

Two EM waves and an EP wave are involved in SRS. Physically, SRS may be understood as a high frequency density ripple (EP wave) resonantly driven by the pondermotive force of two oppositely propagating EM waves. Equations (10) and (11) are used to describe SRS. The non-linear current $(n_e \underline{v}_e)$ in Eq. (10), non-linear convective $(\underline{v}_e \cdot \nabla)\underline{v}_e$ and Lorentz term $(\underline{v}_e \times \underline{B})$ in Eq. (11) remain as dominant non-linear terms. The assumption is made that for linearized coupled wave equations all waves can be expressed as a product of a slowly varying amplitude and a rapidly changing phase in space and time. Thus the incident and reflected EM waves, and the EP wave are written as

$$\underline{E}_T = R_e\{\underline{\hat{e}}_L \xi_L(\underline{x},t) e^{i(\underline{k}_L \cdot \underline{x} - \omega_L t)} + \underline{\hat{e}}_R \xi_R(\underline{x},t) e^{i(\underline{k}_R \cdot x - \omega_R t)}\} \qquad (16)$$

$$n_{e_1} = R_e\{N_{ep}(\underline{x},t) e^{i(\underline{k}_{ep} \cdot \underline{x} - \omega_{ep} t)}\} \qquad (17)$$

For the incident laser with

$$\underline{E}_L = \underline{\hat{e}}_L \xi_L e^{i(\underline{k}_L \cdot \underline{x} - \omega_L t)}$$

we then have

$$\left(\frac{\partial^2}{\partial t^2} - c^2\nabla^2 + \omega_{pe}^2 - i\,\frac{\omega_p^2 e}{\omega_L}\,\nu_e\right)\underline{E}_L = i\,\frac{4\pi e^2}{m_e\omega_L}\,\frac{\partial}{\partial t}\,(n_e\underline{E}_T) \quad . \tag{18}$$

An operator $D(k_o, \omega_o)$ is defined as:

$$D = \left(\frac{\partial^2}{\partial t^2} - c^2\nabla^2 + \omega_{pe}^2 - i\,\frac{\omega_{pe}^2}{\omega_L}\,\nu_e\right) \quad . \tag{19}$$

We can write Eq. (18) as:

$$D\underline{E}_L = \Gamma\frac{\partial}{\partial t}\,n_e\underline{E}_T \tag{20}$$

where the coupling coefficient is expressed as:

$$\Gamma_1 = -i\,\frac{4\pi e^2}{m_e\omega_L} \quad .$$

We expand the LHS around $(k_o, \omega_o)$ to obtain the second order terms. This expansion may be expressed formally as follws,

$$D = \underset{O(1)}{D(k_o,\omega_o)} + \underset{O(\epsilon)}{i\,\frac{\partial D}{\partial\omega}\,\frac{\partial}{\partial t}} + i\,\frac{\partial D}{\partial k}\,\frac{\partial}{\partial x} + O(\epsilon^2) \tag{21}$$

Here $\left(i\,\frac{\partial}{\partial x}\,,\ i\,\frac{\partial}{\partial t}\right)$ on the slowly varying amplitude is taken to be small quantities. "$\epsilon$" order terms are retained, knowing $D(k_o, \omega_o)=0$ in Eq. (20):

$$\left(i\,\frac{\partial D}{\partial\omega}\,\frac{\partial}{\partial t} + i\,\frac{\partial D}{\partial\underline{k}}\cdot\frac{\partial}{\partial\underline{x}} - i\,\frac{\omega_{pe}^2}{\omega_L}\nu_e\right)\underline{E}_L = i\,\frac{4\pi e^2}{m_e\omega_L}\,\frac{\partial}{\partial t}\,(n_{ep}\underline{E}_T)$$

or

$$\left(\frac{\partial}{\partial t} + \underline{V}_{g,L}\cdot\frac{\partial}{\partial\underline{x}} - \frac{\omega_{pe}^2}{\omega_L^2}\nu_e\right)\xi_L = -i\,\frac{4\pi e^2}{m_e\omega_L}\,N_{ep}\xi_R \tag{22}$$

where

$$\underline{V}_g \equiv \frac{\partial D}{\partial\underline{k}} \Big/ \frac{\partial D}{\partial\omega} \quad \text{and} \quad i\,\frac{\partial D}{\partial\omega} \equiv \omega_L$$

Two more coupled mode equations are derived with the same procedures. We rewrite these three equations as,

$$\left(\frac{\partial}{\partial t} + \underline{V}_{g,L}\frac{\partial}{\partial \underline{X}} + \frac{\omega_{pe}^2}{\omega_L^2}\nu_e\right)\xi_L = -iA_1 N_{ep}\xi_R \qquad (23)$$

$$\left(\frac{\partial}{\partial t} + V_{g,R}\cdot\frac{\partial}{\partial \underline{x}} + \frac{\omega_{pe}^2}{\omega_R^2}\nu_e\right)\xi_R = -iA_2 N_{ep}^*\xi_L \qquad (24)$$

$$\left(\frac{\partial}{\partial t} + \underline{V}_{g,ep}\frac{\partial}{\partial \underline{x}} + \nu_e\right)N_{ep} = -iA_3\xi_L\xi_R^* \quad , \qquad (25)$$

where the coefficients $A_1$, $A_2$, $A_3$ are given by

$$A_1 = \frac{4\pi e^2}{m_e\omega_L}$$

$$A_2 = \frac{4\pi e^2}{m_e\omega_R}$$

$$A_3 = \frac{n_o e^2 k_{ep}^2}{m_e^2\omega_L\omega_R\omega_{ep}} \quad .$$

In the weak coupling limit, $\xi_L$ = constant and $|\xi_L| \gg |\xi_R|, |N_{ep}|$ can be assumed. SRS can thus be examined by using Eqs. (27) and (28). As mentioned earlier, the amplitudes $\xi_s$ and $N_{ep}$ vary slowly as exp $i(\underline{K}\cdot\underline{x} - \Omega t)$ under the initial approximation. Equation (24) and (25) yield the dispersion relation

$$(\Omega - \underline{K}\cdot\underline{v}_{g,R} + i2\gamma_R)(\Omega - \underline{K}\cdot\underline{v}_{g,ep} + i2\gamma_{ep})$$

$$+ A_2A_3|\xi_L|^2 = 0 \quad , \qquad (26)$$

where

$$\gamma_R = \frac{\omega_{pe}^2}{2\omega_R^2}\nu_e \quad , \qquad \gamma_{ep} = \frac{\nu_e}{2}$$

We find the threshold when $\mathrm{Im}\,\Omega = 0$ in the above dispersion relation to be:

$$A_2 A_3 |\xi_L|^2 = \gamma_R \gamma_{ep} \qquad (27)$$

for a time-dependent problem, putting $\underline{k} = 0$.

Thus the minimum threshold is

$$\left(\frac{v_o}{v_e}\right)^2 = \frac{4}{k_{ep}^2 \lambda_d^2} \frac{\nu_e^2}{\omega_{pe}^2} \frac{\omega_{ep}}{\omega_R} \qquad (28)$$

where $k_{ep} \cong 2k_L$ (backscatter case) is taken.

$v_o = \dfrac{e\xi_L}{m_e \omega_L}$ is the peak oscillating velocity of the incident electric field.

The growth rate just above threshold is given by

$$\gamma_o^2 = \frac{1}{4} \frac{\omega_{pe}^2 k_{ep}^2 v_o^2}{\omega_R \omega_{ep} \gamma_R} \qquad (29)$$

## 2. SRS in Inhomogeneous Plasma.

The $\underline{k}$-matching condition (momentum conservation) is only satisfied locally in inhomogeneous plasmas. This inhomogeneity of plasma can be expressed by the wave number mismatch,[57]

$$K = k_{Lx} - k_{Rx} - k_{epx} \qquad (30)$$

This phase mismatch localizes the region of the instability. In the weak coupling limit, we have coupled mode equations slightly modified from Eqs. (24) and (25):

$$\left(\frac{\partial}{\partial t} + \underline{v}_{g,R}\cdot\frac{\partial}{\partial \underline{x}} - 2\gamma_R\right)\xi_R = -iA_2 N_{ep}^{*}\xi_L \exp\left(i\int^{x} K dx'\right) \qquad (31)$$

$$\left(\frac{\partial}{\partial t} + \underline{v}_{g,ep}\cdot\frac{\partial}{\partial \underline{x}} - 2\gamma_{ep}\right)N_{ep} = -iA_3\xi_L\xi_R \exp\left(i\int^{x} K dx'\right) \qquad (32)$$

Liu et al. took the Laplace transform of Eqs. (31) and (32) and solved the equations, reducing them to the standard parabolic cylinder equation, and showed the solution to have the form

$$I = I_0 \exp\left(2\pi\gamma_0^2/v_{g,ep}v_{g,R}K'\right) \qquad (33)$$

where

$\gamma_o$ = homogeneous growth rate given in Eq. (29)

$I$ = intensity of the scattered light

$I_o$ = incident laser intensity,

$K' = \frac{d}{dx} K.$

Substantial amplification may be possible, when

$$\gamma_o^2 / v_{g,ep} v_{g,R} K' > 1 \qquad (34)$$

K' is found from the normal dispersion relations of the three waves (two EM and one EP waves) to be

$$K' = \frac{\omega_{pe}^2}{6 k_L L_n v_e^2} \left\{ \frac{1}{2 \sin^2 \frac{\theta}{2}} + 3 \frac{v_e^2}{c^2} \left( \frac{1}{\cos\theta} - 1 \right) \right\} \qquad (35)$$

where $\cos\theta = k_{Lx} / |k_L|$

The amplification factor for Raman backscatter ( $\theta = \pi$ ) is

$$\frac{\gamma_o^2}{v_{g,R} v_{g,ep} K'} = \left[ \frac{v_o}{c} \right]^2 k_L L \qquad (36)$$

Thus the threshold for the convective Raman instability below $n_c/4$

is defined by

$$\left(\frac{v_o}{c}\right)^2 k_L L > 4 \qquad (37)$$

The Raman instability at $n_c/4$ can grow in time (absolute instability), since the group velocity of the scattered light approaches zero. The WKB approximation used in obtaining the convective Raman threshold may not be valid. The threshold for the absolute Raman instability is found by solving the eigen-value equation obtained by combining Eqs. (10) and (11), where the $T_e$ term in Eq. (11) is neglected (cold plasma assumption). Amplification is possible when the imaginary part of the frequency is larger than zero, and threshold is

$$\left(\frac{v_o}{c}\right)^2 (k_L L)^{4/3} > 4 \qquad (38)$$

where the density scale length reflects the width of the large amplitude region of the instability.

Energy conservation among interacting waves is expressed as a form of frequency matching condition ($\omega_L = \omega_{SRS} + \omega_{ep}$). This, with the use of the normal dispersion relation of EP waves ($\omega_{ep}^2 = \omega_{pe}^2 + 3 k_{ep}^2 v_e^2$), determines the plasma density, at which the instability occurs. The density is given by:

$$n_{SRS} = \left(\frac{\lambda_{SRS} - \lambda_L}{\lambda_{SRS}}\right)^2 n_c - 3\left(\frac{k_{ep}}{k_L}\right)^2 \left(\frac{v_o}{c}\right)^2 n_c \qquad (39)$$

where $\lambda_{SRS}$ is the Raman scattered wavelength, $\lambda_L$, the laser wavelength, $n_c$, the plasma critical density, $\omega_{ep}$, the EP frequency, $k_{ep}$, the EP wave number, $k_L$, the laser light wave number, and $v_e$ the electron thermal velocity. The second term represents a small correction due to the finite temperature.

In consequence of this Raman instability, supra-thermal electrons may be generated. The instability could accelerate electrons through Landau damping or wave breaking of the excited EP waves. In Landau damping, the rate $\gamma$ at which the wave transfers its energy to electron kinetic energy is given by[59]

$$\gamma \propto \omega_{ep} \frac{\omega_{pe}^2}{k_{ep}^2} \frac{1}{n_o} \left.\frac{\partial f_o}{\partial u}\right|_{u=\frac{\omega_{ep}}{k_{ep}}} \qquad (40)$$

where $f_o$ is the electron velocity distribution function, $n_o$, the electron density. The wave energy is converted to the energy of electrons, whose velocities are,

$$u \simeq \frac{\omega_{ep}}{k_{ep}} \qquad \text{(phase velocity of the EP wave).}$$

Landau damping for a Maxwell - Boltzman distribution becomes important, when $k\lambda_d \cong O(1)$. Here $\lambda_d = \left(\frac{T_e}{4\pi n_o e^2}\right)^{1/2}$ is the Debye length of a plasma.

The phase velocty, $v_p$ of EP waves is estimated from the normal dispersion equations of both EM and EP waves, noting $k_{ep} \cong k_L$ at $n_c/4$ to be

$$v_p = \left( \frac{\omega_L^2}{4k_L^2} + \frac{3}{2} v_e^2 \right)^{\frac{1}{2}} \geq \frac{c}{\sqrt{3}} \quad . \quad (41)$$

Wavebreaking, which can generate supra-thermal electrons as well[60], occurs when the excited electrostatic field $E_{ep}$ is large enough to drive electrons to the wave phase velocity. In the cold plasma limit, this point corresponds to the singularity, where the kinetic energy of electrons becomes zero in the wave frame. The kinetic energy of accelerated electrons by these mechanisms up to the EP phase velocity at $n_c/4$ could be of the order of [61,62]

$$\frac{1}{2} \frac{m_e}{\left(1 - \frac{u^2}{c^2}\right)^{\frac{1}{2}}} u^2 = \frac{1}{2} \frac{m_e}{\left(1 - \frac{v_p^2}{c^2}\right)^{\frac{1}{2}}} v_p^2 \simeq 100 \text{ keV} \quad .$$

## C. Two Plasmon ($2\omega_{pe}$) Decay Instability.

When the incident laser decays into two EP waves in a three wave parametric process, the instability is called 2 $\omega_{pe}$ decay instability. The instability grows in time (absolute mode) at $n_c/4$ where the two EP wave frequencies ( $\omega_{ep1}$, $\omega_{ep2}$ ) equally match with the natural mode frequency ( $\omega_{ep1} = \omega_{ep2} = \omega_L/2$ ) and the energy among the waves is conserved ( $\omega_L = \omega_{ep1} + \omega_{ep2}$ ). This instability, like SRS, may produce supra-thermal electrons through wave breaking or Landau damping, and has the lowest threshold among parametric instabilities. Characteristic of the instability is densiy steepening at $n_c/4$. The steepening occurs when the pondermotive forces of the excited EP waves exceed the thermal pressure of the plasmas and displace ions. As shown in the experimental section, the steepening at $n_c/4$ is indicated in our SRS data. This steepening affects the thresholds of the parametric instabilities near $n_c/4$, since these are funtions of the density scale length.

In order to derive the threshold and growth rate, a similar procedure to that used in the SRS case is applicable. As before, the EM (pump) wave and decayed EP waves are expressed by:

$$\underline{E}_L = \mathrm{Re}\{\underline{\hat{e}}_L \xi_L e^{i(\underline{k}_L \cdot \underline{x} - \omega_L t)}\} \qquad (42)$$

$$n_{e1} = \mathrm{Re}\{N_{ep1} e^{i(\underline{k}_{ep1} \cdot \underline{x} - \omega_{ep1} t)} + N_{ep2} e^{i(\underline{k}_{ep2} \cdot \underline{x} - \omega_{ep2} t)}\} \quad . \qquad (43)$$

The second order equations now become:

$$(\frac{\partial}{\partial t} + \underline{v}_{g,ep1}\cdot\nabla + \gamma_{ep})N_{ep1} = \Gamma_2 \xi_L N^*_{ep2} \qquad (44)$$

$$(\frac{\partial}{\partial t} + \underline{v}_{g,ep2}\cdot\nabla + \gamma_{ep})N_{ep2} = \Gamma_1 \xi_L N^*_{ep1} \qquad (45)$$

$$\Gamma_1 = \frac{ek_{ep2}}{4m_e\omega_L}(\underline{\hat{k}}_{ep2}\cdot\underline{\hat{e}}_L)(1 - \frac{k^2_{ep2}\omega_{ep1}}{k^2_{ep1}\omega_{ep2}})$$

$$\Gamma_2 = \frac{ek_{ep1}}{4m_e\omega_L}(\underline{\hat{k}}_{ep1}\cdot\underline{\hat{e}}_L)(1 - \frac{k^2_{ep1}\omega_{ep2}}{k^2_{ep2}\omega_{ep1}})$$

The homogeneous threshold and growth rate obtained from the above equations are,

$$v_o = \frac{4\gamma_e(k_{ep1}k_{ep2})^{1/2}}{k_L|\underline{k}_{ep1} - \underline{k}_{ep2}|}\,|\cos\theta_1\cos\theta_2|^{-1/2} \qquad (46)$$

$$\gamma = \frac{e\xi_L k_L}{4m_e\omega_L}\,\frac{|\underline{k}_{ep1} - \underline{k}_{ep2}|}{(k_{ep1}\cdot k_{ep2})^{1/2}}\,(\cos\theta_1\cos\theta_2)^{1/2} \qquad (47)$$

where

$$\cos\hat{\theta}_{1,2} = \underline{\hat{k}}_{ep1,2}\cdot\underline{\hat{e}}_L.$$

Maximum growth rate in Eq (47) is attained when $\theta_1 = \frac{\pi}{4}, \theta_2 = \frac{3\pi}{4}$ using momentum conservation,

$$\underline{k}_L = \underline{k}_{ep1} + \underline{k}_{ep2}.$$

Since the momentumn has to be conserved, the first and second EP waves thus propagate oppositely but angled at $45^o$ with respect to the laser wave vector.

The procedure to derive the threshold condition of $2\omega_{pe}$ instability in an inhomogeneous plasma is found in Ref. 51 and is the same as that described briefly in the discussion of the Raman instability. The inhomogeneity of plasma results in the wave number mismatch as shown in Eq. (30). In Eq. (30) though (33), two EP waves should be substituted for a scattered EM wave and an EP wave in $2\omega_{pe}$ instability. The threshold is obtained from Eq. (33), and listed in Table II-1.

**4. Stimulated Brillouin Scattering (SBS).**

Stimulated Brillouin scattering, named in analogy with a similar phenomena in molecular physics, like SRS, is also a three wave parametric instability. An incident EM wave ($k_L, \omega_L$), this time, decays into a scattered EM wave ($k_B$, $\omega_B$) and an IA wave ($k_{IA}$, $\omega_{IA}$) at the plasma density where the energy ($\omega_L = \omega_B + \omega_{IA}$) and the momentum ($\underline{k}_L = \underline{k}_B + \underline{k}_{IA}$) are conserved. The photon energy of the Brillouin scattered light ($\omega_B = \omega_L - \omega_{IA}$) is almost equal to that of the incident EM wave, since the ratio $\omega_{IA}/\omega_L$ is usually very small ($\sim 1/10^3$). Because of this condition, the critical density of the scattered light is about equal to that of the incident laser and the instability can be operative in the whole underdense region up to the critical density. In fact, collective SBS has been found in a number of experiments, to scatter away an appreciable amount of the incident laser energy.[13-44] Thus SBS has the potential to play a dangerous role as a reflection mechanism, and has been one of the crucial subjects of study in laser fusion.

One of the main objectives in this work is to determine whether the SBS becomes significant in the case of UV ( $\lambda_L = 0.35$ μm) laser irradiation. The wavelength scaling by Max and Estabrook indicates less strenuous SBS for shorter wavelength laser.[63] In the case of weak coupling limit, the reflectivity due to SBS was shown to be a function of a background noise level and a parameter called "Q" given below. Q is

the number of SBS spatial gain lengths in a plasma of length L given by Tang[64] as:

$$R(1 - R) = B[\exp\{Q(1 - R)\} - R] \quad . (48)$$

Here R is the reflectivity and B the noise level. Q is given by:

$$Q = 2\pi\left(\frac{L}{\lambda_L}\right)\left(\frac{I_L}{10^{16}\ W/cm^2}\right)\left(\frac{n}{n_c}\right)\left(\frac{\lambda_L}{1\ \mu m}\right)\left(\frac{1\ keV}{T_e}\right)D^{-1} \quad , (49)$$

where

$$D = \left(\frac{\nu_i}{\omega_{IA}}\right)\left(1 + \frac{3T_i}{ZT_e}\right)\left(1 - \frac{n}{n_c}\right),$$

$L$ = density scale length

$\lambda_L$ = laser wavelength

$I_L$ = on-target laser intensity

$n$ = density of SBS region

$T_e(T_i)$ = electron (ion) plasma temperature

$\nu_i$ = ion wave damping frequency

$\omega_{IA}$ = ion acoustic frequency

$Z$ = charge state.

One may see that Eq. (48) takes the same form as Eq. (33) of the convective Raman instability for small R and "Q" corresponds to the

convective gain in an inhomogeneous plasma. When Q is 15 and the noise level is 0.1 % of the incident intensity, the reflectivity is estimated to be ~ 50 %. Q was shown in Ref. 63 to be proportional to $\lambda_L{}^n$, where n is dependent on the dominant absorption the mechanisms:

$$Q \propto \lambda^{7/3} \quad \text{(collisional absorption limit)}$$

$$Q \propto \lambda_L \quad \text{(resonance absorption limit)}$$

Thus quality factor Q which affects the reflectivity due to SBS may vary strongly with $\lambda_L$.

The threshold is obtained, using the same principle shown in the theory of SRS (i.e. Chap. II - A, B). The formula of the threshold is shown in Table II-1.

## E. MODULATIONAL INSTABILITY.

Even though the three wave processes are the lowest order among parametrically coupled instabilities, higher order non-linear terms can become importantant under certain conditions. For example, in the case of the modulational instability, an EM wave starts exerting its pondermotive force, expelling plasma, when the force is comparable to the thermal plasma pressure. Induced plasma density variations (IA waves) now affect the phase of the EM wave, since the refractive index is a function of the plasma density. This process can be described by taking non-resonat terms into account in the SBS equations.[38,65] To briefly show the origin of the instability, we consider two oppositely propagating EM waves. The waves form a standing wave and each of the waves can couple to another EM wave and IA wave above the threshold intensiy. The pertinent equations for use are similar to those for SBS. Equatuions (10) and (15) for an EM wave and IA wave are

$$\left(\frac{\partial}{\partial t}^2 - c^2\nabla^2 + \omega_{pe}^2\right)\underline{E}_T = -4\pi n_o e(\underline{v}_e\cdot\nabla)\underline{v}_e - \frac{\omega_{pe}^2}{c}(\underline{v}_e\times\underline{B})$$

$$+ 4\pi e\frac{\partial}{\partial t}(\underline{n}_{e1}\underline{v}_e) + \frac{4\pi e\gamma_e T_e}{n_o m_e} n_{eo}\nabla n_{e1} + i\frac{\omega_{pe}^2}{\omega_L}\nu_e\underline{E}_T \qquad (10)$$

$$\left(\frac{\partial}{\partial t}^2 - c_s^2\nabla^2\right)n_{e1}^s = -\frac{m_e}{m_i}\nabla\cdot\{\frac{\gamma_e T_e}{n_o m_e} n_{eo}\nabla n_{e1} - \frac{n_o e}{m_e c}(\underline{v}_e\times\underline{B})$$

$$- n_o(\underline{v}_e\cdot\nabla)\underline{v}_e + \frac{\partial}{\partial t}(n_{e1}^s\underline{v}_e)\} - \frac{m_e}{m_i}\nu_e\frac{\partial}{\partial t}n_{e1}^s \quad . \qquad (15)$$

The electromagnetic waves are again assumed to be a product of a slowly varying amplitude and a plane wave defined by the linear dispersion relation. A standing pump wave, which is a sum of two oppositely traveling waves, is given by

$$\underline{E}_{TL} = \mathrm{Re}\{\xi^{+}_{TL} e^{i(\underline{k}_L \cdot \underline{x} - \omega_L t)} + \xi^{-}_{TL} e^{i(\underline{k}_L \cdot \underline{x} + \omega_L t)}\} \qquad (50)$$

and the excited backscattered EM waves are

$$\underline{E}_{T1,2} = \mathrm{Re}\ \xi_{T1,2}(\underline{x},t) e^{i(\underline{k}_{1,2} \cdot \underline{x} - \omega_{1,2} t)} \quad . \qquad (51)$$

$\underline{E}_{T1}$ is the backscattered wave from the decay of the $\xi^{+}_{TL} e^{i(\underline{k}_L \cdot \underline{x} - \omega_L t)}$, while $\underline{E}_{T2}$ comes from $\xi^{-}_{TL} e^{i(\underline{k}_2 \cdot \underline{x} + \omega_L t)}$.

Here the dispersion relation of the excited EM waves are given by:

$$\omega^2_{1,2} = \omega^2_{pe} + c^2 k^2_{1,2} \quad . \qquad (52)$$

The density perturbation we consider is

$$n^{s}_{e1} = N_{IA}(\underline{x},t)\ e^{i\underline{k}_{IA} \cdot \underline{x}}$$

where the time variation of the density perturbation is assumed to be dominated by the non-linear interaction. Taking the second order in Eq. (10), we obtain the mode coupling equation

$$\left(\frac{\partial}{\partial t} + \underline{v}_1 \cdot \frac{\partial}{\partial \underline{x}} + \gamma_T\right) \xi_{T1} = -iC_{so} N^{*}_{IA} \xi^{+}_{L} e^{-i\delta t} \quad , \qquad (54)$$

where

$$C_{so} = \frac{e^2\pi}{m_e\omega_L}$$

$$\delta = \omega_L - \omega_1 \text{ (or 2)}$$

$$\gamma_T = \frac{\nu_e\omega_{pe}^2}{2\omega_T^2}$$

$v_1$ = group velocity of $\xi_{T1}$.

Similarly we can obtain the mode coupled equations for $\xi_{T2}$ and $N_S$,

$$\left(\frac{\partial}{\partial t} + \underline{v}_2\cdot\frac{\partial}{\partial \underline{x}} + \gamma_T\right)\xi_{T2} = iC_{so}N_{IA}^{*}\xi_o e^{i\delta t} \qquad (55)$$

$$\left(\frac{\partial}{\partial t}^2 + \gamma_s\frac{\partial}{\partial t} - c_s^2\frac{\partial}{\partial x}^2 - 2ic_s\underline{k}_{IA}\cdot\frac{\partial}{\partial \underline{x}} + k_{IA}^2c_s^2\right)N_{IA}$$

$$= -C_{01}\left\{\xi_L^{+}\xi_{T1}^{*}e^{-i\delta t} + \xi_L^{-}\xi_{T2}^{*}e^{i\delta t}\right\} \quad , (56)$$

where $\gamma_s$ is the effective damping for density fluctuation and

$$C_{01} = \frac{n_o e^2 k_{IA}^2}{2m_e m_i \omega_L \omega_1} \quad .$$

Assuming the pump amplitude is constant, namely

$$|\xi_L^{+}| = |\xi_L^{-}| = |\xi_L| \quad ,$$

and the other higher order amplitudes, $\xi^{+}_{T1}e^{-i\delta t}$, $\xi^{*}_{T2}e^{i\delta t}$, and $N_{IA}$ change as $\exp i(Kx-\Omega t)$, the dispersion equation is given by

$$(\Omega - Kv_{1x} + \delta + i\gamma_T)\cdot(\Omega - Kv_{2x} - \delta + i\gamma_T) \times$$

$$(\Omega^2 - k_{IA}^2c_s^2 + i\Omega\gamma_s - K^2c_s^2 - 2k_{IA}Kc_s^2)$$

$$+ 2C_{01}C_{so}|\xi_L|^2\delta = 0 \qquad . \quad (57)$$

A purely growing mode (i.e. $\Omega = iy$) for $K = 0$ is possible for the case $\delta < 0$. This is the condition, for which the density perturbation grows for time,

$$N_{IA} \propto e^{-i\Omega t} = e^{yt} \qquad . \quad (58)$$

The minimum threshold for this instability is obtained by setting Im $\Omega$ = $y = 0$ in the above Eq. (57) as

$$\left(\frac{v_o}{v_e}\right)^2 = -\frac{c_s^2k_{IA}^2m_e\omega_L^2}{2C_{01}C_{so}\delta e^2}T_e(\delta^2+\gamma_T^2) \qquad . \quad (59)$$

The growth rate well above the threshold is

$$\frac{\gamma_g}{\omega_L} = -\frac{\gamma_T}{\omega_L} + K_s(K_o - K_s)^{1/2} \qquad , \quad (60)$$

where

$$K_s = \frac{ck_{IA}}{\sqrt{2}\omega_L} \quad , \quad K_o = \frac{\omega_{pe}^2}{4\omega_L^2}\frac{v_o^2}{v_e^2} \quad .$$

Since $\gamma_g$ above the threshold allows various values of $k_s$, the frequency

of the modulated EM wave is broadened. A possible maximum width of the broadening is given by

$$\frac{\Delta\lambda}{\lambda_L} = \frac{1}{4}\left(\frac{\omega_{pe}}{\omega_L}\right)^2\left(\frac{v_o}{v_e}\right)^2 \quad , \quad (61)$$

Table II-1

| INSTABILITY | DENSITY | THRESHOLD | THRESHOLD [W/cm$^2$] |
|---|---|---|---|
| SRS (abs.) | $n_c/4$ | $\left(\frac{V_o}{c}\right)^2 (k_L L_n)^{4/3} > 4$ | $\frac{5 \times 10^{17}}{L_\mu^{4/3} \lambda_\mu^{2/3}}$ |
| SRS (conv.) | $< n_c/4$ | $\left(\frac{V_o}{c}\right)^2 k_L L_n > 4$ | $\frac{4.4 \times 10^{17}}{L_\mu \lambda_\mu}$ |
| $2\omega_{pe}$ decay | $n_c/4$ | $\left(\frac{V_o}{V_e}\right)^2 k_L L_n > 12$ | $\frac{5 \times 10^{12} T_e}{L_\mu \lambda_\mu}$ |
| SBS | $\leq n_c$ | $\left(\frac{V_o}{V_e}\right)^2 \left(\frac{\omega_{pe}}{\omega_L}\right)^2 k_L L_U > 1$ | $\frac{4.3 \times 10^{11} T_e n_c}{n_e L_\mu}$ |
| Modulational | $\leq n_c$ | $\left(\frac{V_o}{V_e}\right)^2 > 8 \frac{\nu_{ei}}{\omega_L}$ | $\frac{1.67 \times 10^{15} n_e}{\lambda_\mu T_e^{1/2} n_c}$ |

$V_o$ = electron oscillatory velocity
$V_e$ = electron thermal velocity
$k_L$ = laser wave number
$L_n$ = density scale length
$L_U$ = velocity scale length ($\sim L_n$)
$c$ = speed of light
$\omega_{pe}$ = electron plasma frequency
$\omega_L$ = laser frequency
$\nu_{ei}$ = electron-ion collision frequency
$\lambda_\mu$ = laser wavelength (μm)
$L_\mu$ = density scale length (μm)
$T_e$ = background electron temperature (eV)
$n_c$ = critical density
$n_e$ = plasma density of the instability

# III. EXPEIMENTAL SET-UP and PROCEDURES.

## A. INTRODUCTION

In this chapter, two different types of experiments are described, one for the SRS and $2\omega_{pe}$ instabilities, the other for the SBS and modulational instabilities. Differences between these experiments arise in the diagnostics method used and in the spectral range of the scattered light. Both experiments were performed with the one beam UV laser irradiation facility. In the following sections, we shall call the former class of experiments Raman experiments and the latter Brillouin experiments.

## B. FUNDAMENTAL SET-UP AND PROCEDURES.

### 1. GDL ( frequency up-converted laser facility ).

The whole experimental layout is shown in Fig. III-1. The laser used in this study was a frequency tripled Nd:phosphate glass laser (GDL) which delivers UV pulses at $\lambda_L$=0.35 μm of up to 22 J at 90 psec and 60 J at 450 psec. Prepulse energy was suppressed well below $10^{-6}$ of the main pulse. The frequency was tripled by two type II KDP crystals.[66] While the first crystal gave a 2:1 ratio of the second harmonic (GR) to the fundamental (IR), the second crystal combined the two photons to generate the third harmonic (UV). The UV beam was guided by high reflectance UV mirrors, (1), (2), (3) in Fig. III-1, to a target through a focusing lens. Transmitted light (UV/IR/GR) through one of these mirrors, (1) in the figure, was used for the beam diagnostics: calorimeters and a streak camera. A rejection rate, UV/(GR and IR), of $10^3$ was obtained by the UV mirrors. The typical intensity ratio of UV/(GR and IR) on target became higher than $10^4$ due to the large chromatic shift through the focusing lens. The backscattered energy through the focusing lens was monitored by a calorimeter as well. Half of the diagnostic beam transmitted through the UV mirror, (1) in the figure (T = 5 % at $\lambda$ = 3500 Å), was utilized to monitor the far field pattern and focusable energy after a

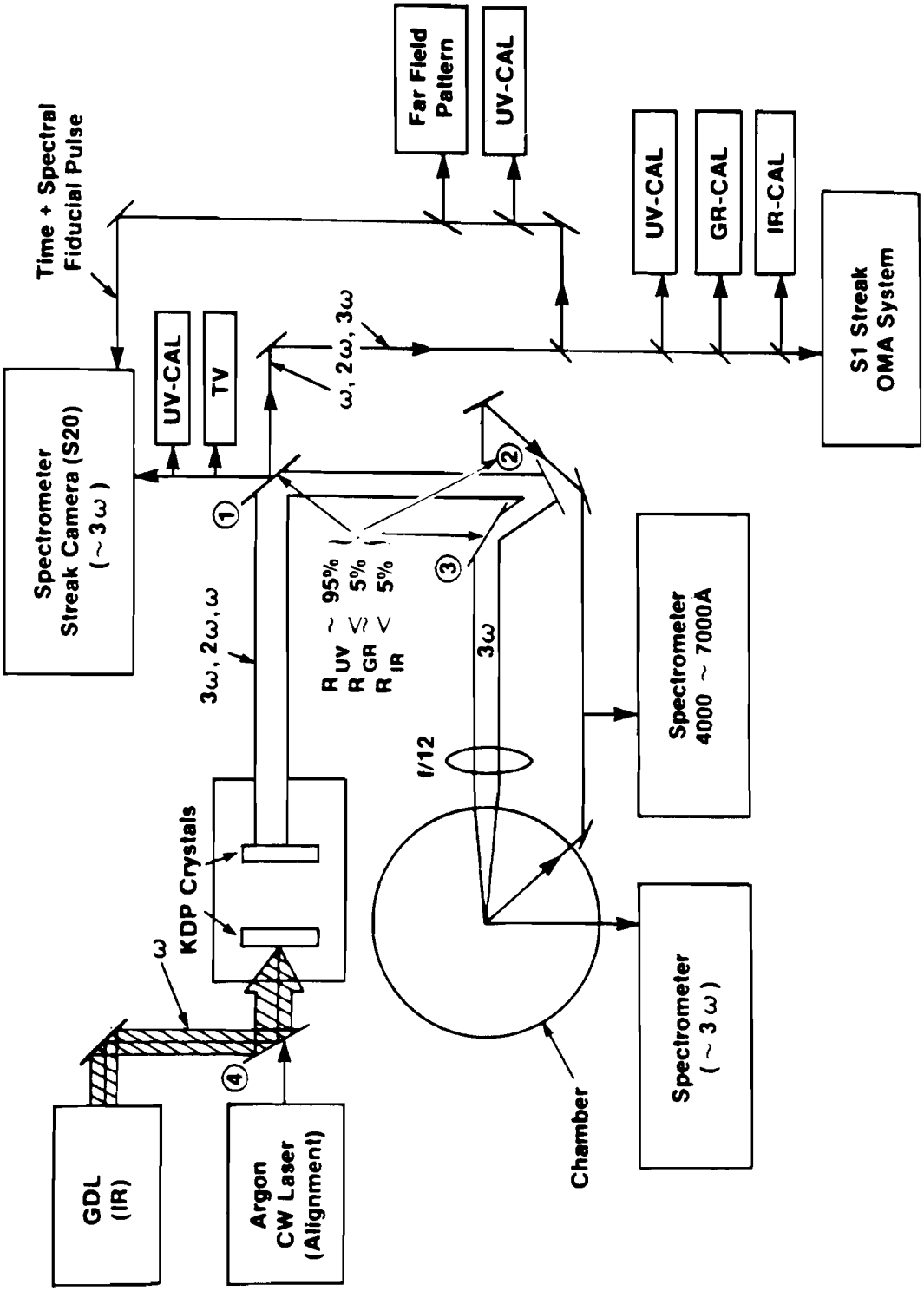


FIGURE III-1 Layout of UV irradiation facility

spatial filter. This beam was also used for the temporal and spectral fiducial mark of the backscattered light measurements. A CW Argon-Ion laser ( $\lambda$ =3511 Å) was used for the UV optical alignment. The Ar-Ion laser was injected through an IR mirror, (4) in the figure, before the crystal box and lined up to the main UV beam axis.

## 2. Target and Focusing Lens.

Targets used throughout our experiment were planar CH, Ni, and Au. Typical dimensions were 1 mm dia. and 50 μm thickness. A target suspended in a vacuum chamber, was viewed by two orthogonally placed TV cameras with telescopes, one directly behind (180°) and the other at 90°. Placement accuracy of the targe was ± 10 μm along the laser axis (X) with comparable accuracy in the other two directions (Y,Z). A slow focusing lens (f/12, Fl = 1764 mm) was chosen, mainly because the narrow cone angle of the beam could allow well defined angular distribution measurement of the scattered light. This was a single element fused silica lens. The marginal cone angle determined by the actual beam size was about ± 1.8° (f/16). Mechanical accuracy of the lens movement was within ±25 μm, while the depth of focus was estimated to be of the order of 1 mm.

### 3. Focal Spot Measurement.

It was important know the focal spot intensity distribution, as this could affect the data interpretation such as the definition of parametric instability threshold. Focal spot sizes were measured by two methods: an x-ray pin hole camera and a telescopic magnifier with a 35 mm SLR camera.

The picture taken by the x-ray pin-hole camera represented the focal pattern of thermal x-rays, which gave an upper limit of the laser beam inprint on a target. Several combinations of Be (25-100 μm) and Al (25 μm) filters were used to obtain the x-ray window of energy from 1 to 2 keV. Typically CH coated glass planar targets were used to observe the spatial distribution of the Si-line emission (≅1.8 keV), since CH coating helped to suppress the blow-off pattern of the plasma along the target normal.

In order to measure the transmitted beam quality, a telescope was set up on the backside of the target. Without the target, the telescope relayed the focal spot image of the equivalent target plane. This relayed image was viewed by a 35 mm SLR camera. Pictures taken with different telescope focal positions gave the spot images at varying x axis positions. Film exposure was taken with a weak UV laser shot.

In both cases, the spatial distribution of the focussed beam was shown to be non-uniform. This non-uniformity introduced an uncertainty in determining the laser intensity on target. For example, if a perfect

Gaussian focal spot is assumed, the laser intensity calculated from the area which contains 90 % of the beam energy is equal to the average intensity. However actual focal spot images taken by either method showed intensity fluctuations ($I_{peak}/I_{ave}$) of 4 - 5 compared to the average intensity. Average intensity is used in this thesis, which is obtained by the total energy on target devided by the pulse width and the measured focal area, and multiplied by 1.5. The focal area was determined by the outside of the x-ray image. This factor 1.5 was suggested by W.Seka[67] to account for the larger equivalent area of higher intensities.

## C. EXPERIMENTAL SET-UP AND PROCEDURES: RAMAN TYPE.

### 1. Back- and Side- Scatter Spectroscopy.

Figure III-2 shows a simplified diagram of the SRS experiment. Spectroscopic measurements were made for back- and side- scattered light. Absolutely calibrated diodes were used to measure the scattered light quantitatively. For 45° targets, magnified focal images were also photographed through an interference filter ( $\lambda$ = 7000 Å).

Backscattered light (4000-7000 Å) was collected and collimated by the f/12 focusing lens. It was then transmitted through the first UV mirror, (3) in Fig. III-1, outside the vacuum chamber, and guided to one of the two grating spectrometers. Low dispersion (63 Å/mm) gratings were chosen to cover the spectral range between 4000 and 7000 Å. The transmission of the optics beyond the focusing lens to the spectrometer was 35 ± 5 % over this 3000 Å spectral range. The output spectrum from the spectrometer was recorded on a Kodak High Speed Infrared (HSI) film, using a 35 mm SLR camera with a 1:1 macro lens. The spectral sensitivity curve of this film, available from Kodak Co., is shown in Fig. III-3. Spectroscopic measurements were also conducted through a 45° port to the incident laser axis, using the other identical spectrometer. In most of

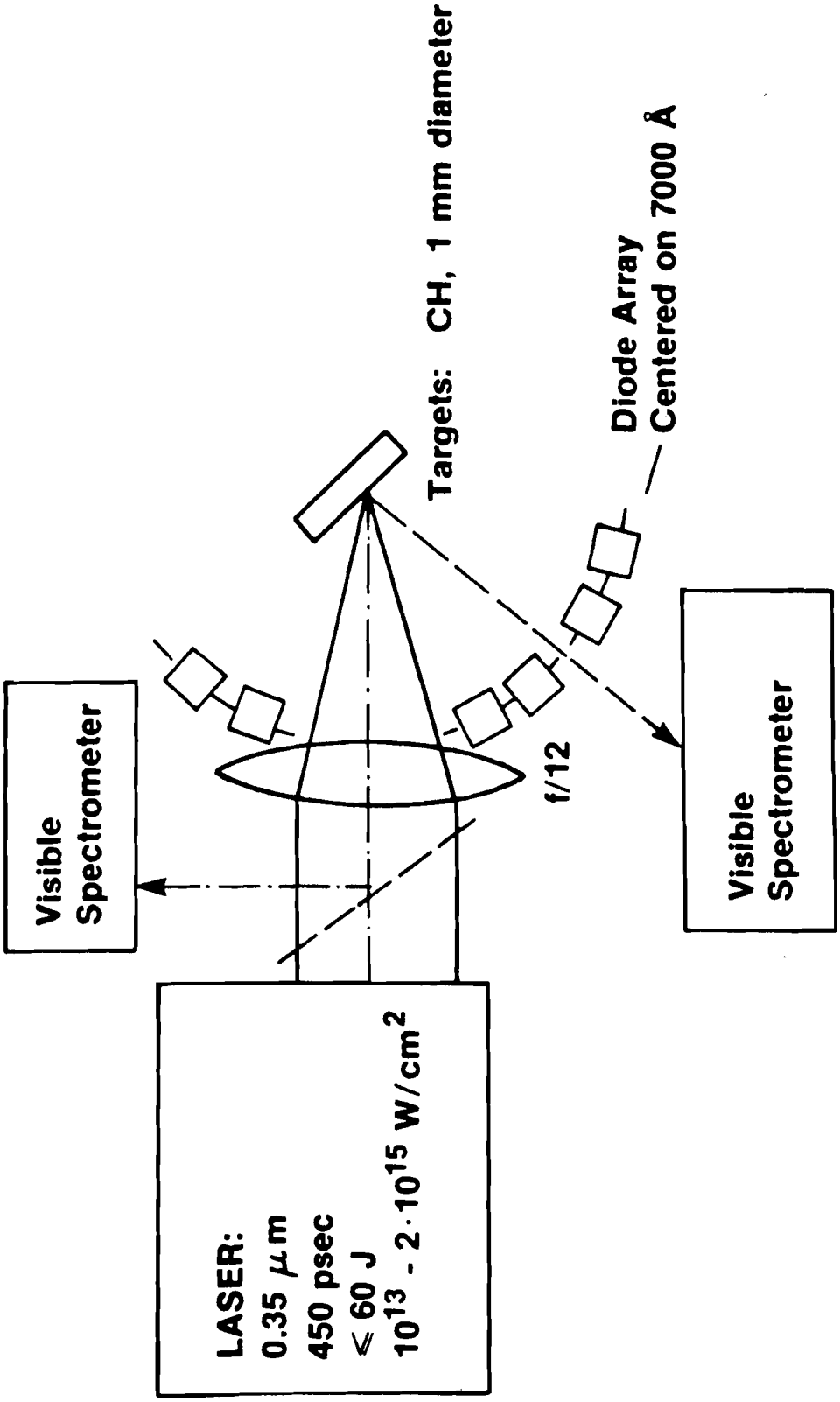


FIGURE III-2 Arrangement for SRS experiment

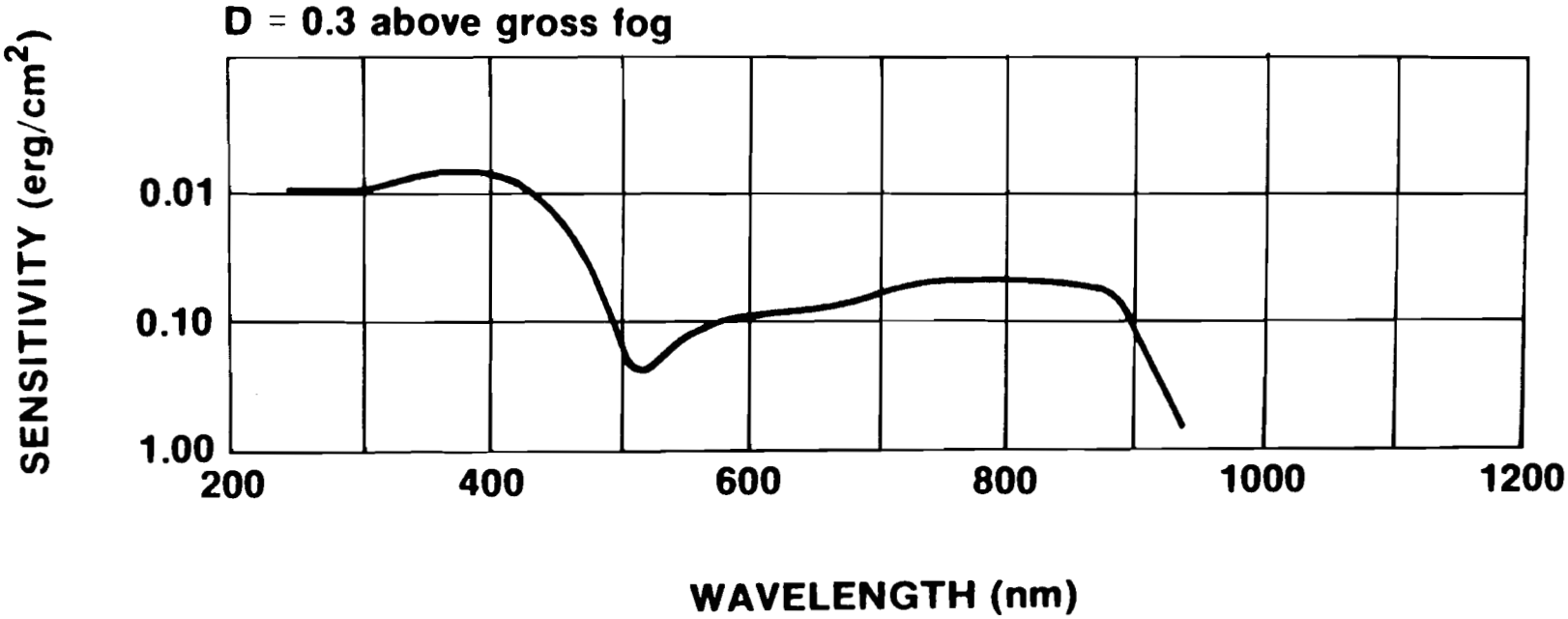


FIGURE III-3 **Spectral sensitivity of Kodak High Speed Infrared film**

these cases, a 45° angled target, facing this port, was used. A SLR camera with a 1:1 macro lens was attached to the spectrometer output.

Spectrometers were aligned with a He-Ne laser. For the backscattered light, a He-Ne laser was located on the backside of the target and aligned to the UV alignment laser axis. The He-Ne laser thus defined the backscatter path and transmitted through the UV mirror, (3) in Fig. III-1. The He-Ne laser beam brought to the spectrometer was focused onto the 25 μm slit by an f/4 quartz lens (Fl = 100 mm) to about a 5 mm dia. For the sidescatter light, an f/2.3 lens (Fl = 100 mm) was placed at 45° to the laser axis, 15 cm from the target. The He-Ne laser irradiated the front of the target, and this reflection was used for the alignment. UV cut-off filters (GG-395/Schott, 3-74/Hoya) were used to eliminate the second order signals arising from residual UV light. The filter rejection rate was more than 60 db.

A plastic polarizer (HN38) was used to examine the polarization of the scattered light.[68] According to the calibration table, the transmission was 38 ± 5 % from 4000 to 7000 Å for unpolarized light. Before a real target shot, we exposed a HSl film to a Hg or Cs lamp with a mask in front of the spectrometer slit to obtain spectral reference lines on the film. The mask was designed to have the reference lines on the top and bottom sides of the frame, leaving a blank area at the middle for the scattered light spectrum. Cs spectral lines are shown in Fig. III-4. The spectral axis was calibrated based on these known lines by using both quadratic and least square fits.

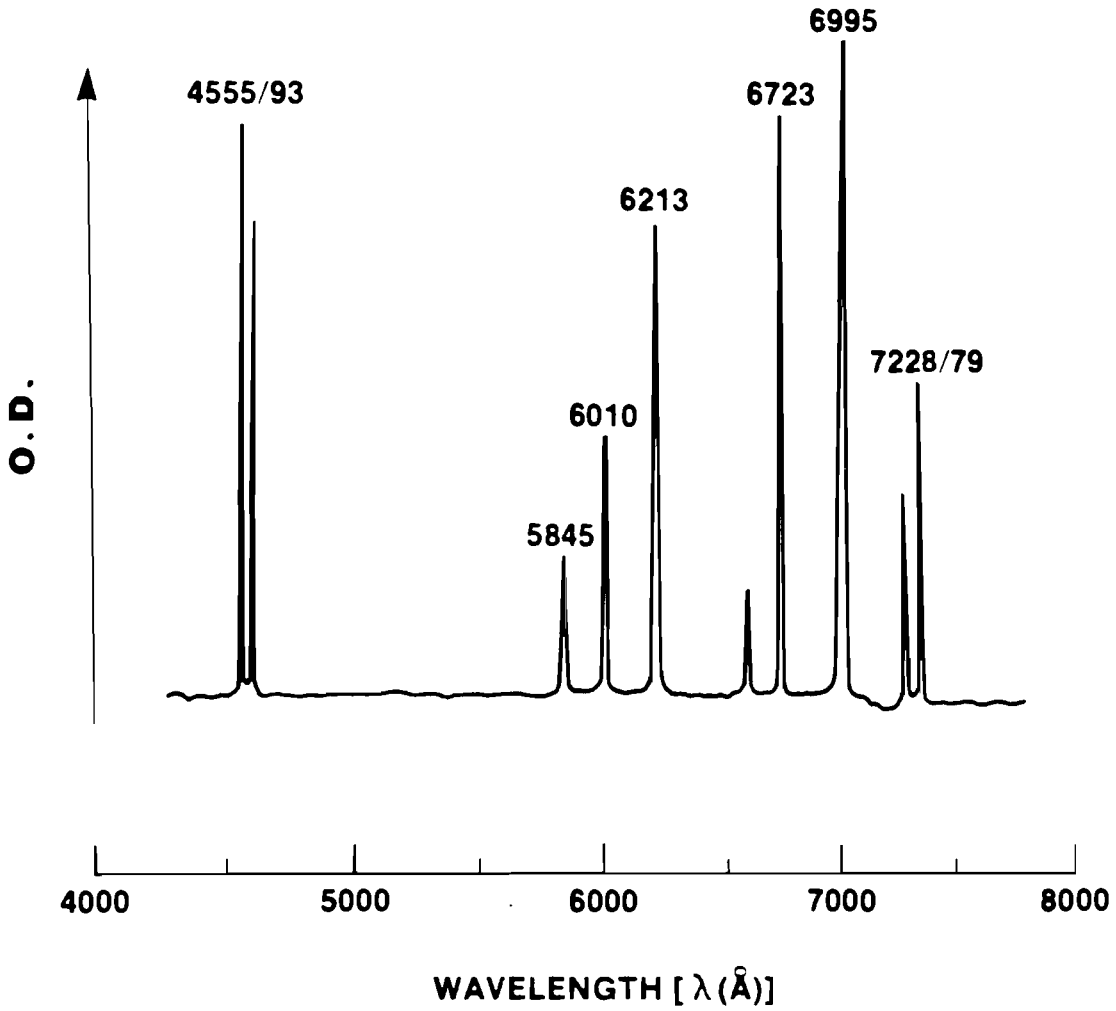


FIGURE III-4 **Cesium spectral lines**

A total number of six photodiodes absolutely calibrated at $\lambda = 7000$ Å ($=\omega_L/2$) were used to obtain the scattered light distribution and energy.* Typically the target (CH) was tilted by 22° in the horizontal plane. The diodes were located 8° apart with respect to the target normal, and in the horizontal plane.

## 2. Focal Spot Photography.

Magnified pictures of the scattering region were taken through an interference filter ( $\lambda = 7000$ Å). In the vacuum chamber, a relay lens (f/2.3, Fl = 100 mm) was placed at 15 cm from the target at 45° to the laser axis. The relayed focal spot image from the 45° target was magnified by a microscope objective lens (10x), and was photographed by a 35 mm SLR camera with a HSI film. Overall magnification, 50x, was obtained.

---

* This part of the experiment was mainly performed by W. Seka and L.M. Goldman, LLE, University of Rochester.

## D. EXPERIMENTAL SET-UP and PROCEDURE: BRILLOUIN TYPE.

### 1. Temporally Resolved Backscatter Spectroscopy.

A layout of the Brillouin experiment is shown in Fig. III-5. Backscattered light near the laser wavelength (3513 ± 20 Å) was spectrally and temporally resolved. Specularly reflected components from 45°-angled target were also spectrally resolved.

Backscattered light transmitted through one of the UV mirrors, (1) in Fig. III-1, was properly reduced in size by an inverse telescope and guided to a 1 m Czerny-Turner grating spectrometer as was a pick-up (2 %)of the incident laser for the temporal and spectral fiducial mark. Backscattered and incident light went through etalons of different spacing (R= 70 % each), giving multiple reflections with a 1/2 intensity step at each reflection. One of these pulses effectively gave proper exposure within the relatively narrow dynamic range (~100) of a streak camera. The time separation between pulses after the etalon was determined by $T = 2L/c$, while c is the speed of light, and L is the distance between the etalon mirrors. The time separation between backscattered pulses was 900 psec, where L was 13.5 cm. Succesive backscattered and incident pulses recorded on the film thus gave a self

- Time Resolution: 40 psec
  (S-20 Streak Camera)
- Spectral Resolution: 1 Å

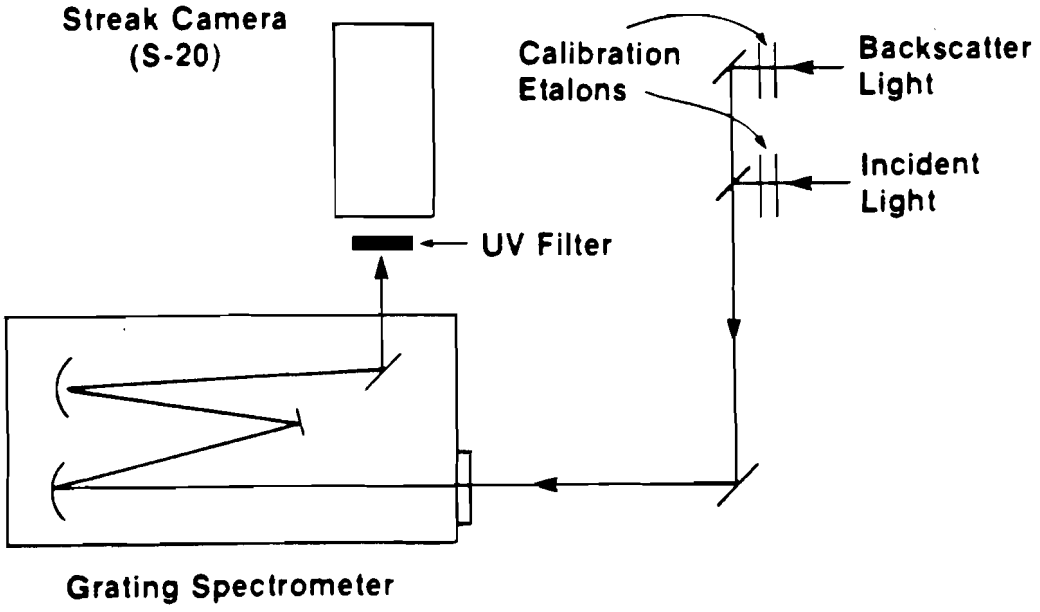


FIGURE III-5 Arrangement for SBS experiment

calibration in time and intensity for each shot. The 1-m (f/10) spectrometer had a 5 cm, 1200 lines/mm grating.

Temporal and spectral resolutions determined by the spectrometer were 40 psec and 0.7 Å, respectively. Time can be broadened for the light diffracted by a grating, since any two adjacent grooves introduce one wavelength of the difference in path length, producing the total path difference of $N\lambda$ .[69] Here N is the total number of grooves and $\lambda$ is the wavelength. Since the spectral resolution is inversely proportional to N, the relation between the spectral and temporal resolution becomes

$$\Delta T \cdot \Delta \nu = 1 \qquad . (1)$$

For example, if $\Delta\lambda$ of 0.1 Å is required, the above relation shows that the upper limit of the temporal resolution is no better than 40 psec. Signal beam was focused onto the input slit of the spectrometer with a quartz lens (Fl = 300 mm). A quartz diffuser was placed in front of the slit to obtain the uniform illumination. The slit opening was 100 $\mu$m wide, which corresponds to $\Delta\lambda$ = 0.7 Å resolution. Half of the grating (50 mm wide) was covered by a mask. The resolving power of the covered grating was given by

$$\frac{\Delta\lambda}{\lambda} = \frac{1}{N} = \frac{1}{25 \times 1200} \qquad . (2)$$

This resolution was $\Delta\lambda$ = 0.1 Å.

The overall spectral resolution was based on the square root of the sum of the square of $\Delta\lambda$ = 0.1 Å (grating) and $\Delta\lambda$ = 0.7 Å (slit width), and was about $\Delta\lambda$ = 0.7 Å.[70] Temporal resolution, which was limited by the $\Delta\lambda$ of the grating, was 40 psec.

The signal after the spectrometer was then temporally resolved by an S-20 photo-cathode streak camera. The built-in slit and the lens housing of the streak camera were removed because of the poor UV transmission capability of the normal optical glass ($T \leqq 1$ % at $\lambda = 3500$ Å). Unnecessary light (room light etc.) was cut by a filter (UG11/Schott) placed in front of the cathode for protection. A 50 μm slit was placed in the output plane of the spectrometer perpendicular to the input slit image. This slit served as a temporal window for the streak camera. The spectrally resolved signal through the time slit was relayed onto the photocathode by a quartz lens (Fl = 300 mm). The magnification at the image intensifier of the streak camera was 0.625 compared to the output of the spectrometer. The signal spectrum on the intensifier was recorded on a Kodak 2475 Recording film (ASA 1000-1600).

The streak camera was triggered by a low voltage biased (45 V) Si-switch. This switch was activated by half of the 1 % pulse picked up after the spatial filter of the second 64 mm dia. amplifier in the GDL laser bay. The transmission cable used between the Si-switch and the streak camera was FM-8 ($R = 50\ \Omega$) to avoid unnecessary signal attenuation and degradation of the trigger rise time.

The alignment of the backscatter diagnostic system was performed with the CW UV alignment laser. A retro-reflecting aluminum coated mirror was placed in front of the f/12 focusing lens and this reflection defined the backscattered light path.

## 2. Time Scale Calibration.

Since an absolute time history of the backscatter data was required, the relative timing between the incident and backscattered pulses was calibrated by two means: using a short UV pulse, and using a long one. In both methods, we measured the time separation between an incident and a backscatter pulse temporal peak. To avoid any drastic change of the backscatter pulse temporal behavior, a low laser intensity was used.

In the former case, a CH planar target was irradiated with 100 psec (FWHM) pulses at low intensities of $10^{13}$ W/cm$^2$, and the backscattered and incident pulses were recorded without changing any streak camera setting from that for the actual target shot. The positions of backscatter peaks in time corresponded to the peak of the incident pulse in the backscatter time history.

As an alternative way of timing calibration, the focusing lens (f/12) was removed and an Al mirror was placed at the target plane. The Al mirror was irradiated by a long pulse (450 psec) UV laser at a low intensity, and the incident and backscattered light was recorded. The time of the backscatter pulse came closer to the incident pulse by the amount of 2Ln/c sec, where L is the lens thickness, n is the refractive index of the lens, and c is the speed of light. From this data, the corresponding incident laser peak on the backscatter pulse could be determined, considering the time difference mentioned above.

From the results of both measurements, the corresponding incident laser peak on the first backscattered signal was deduced to be 750 ± 20 psec from the incident peak. A typical result from the short pulse timing calibration is shown in Fig. III-6 (note: data is presented in the form of iso-intensity contours; see p 52).

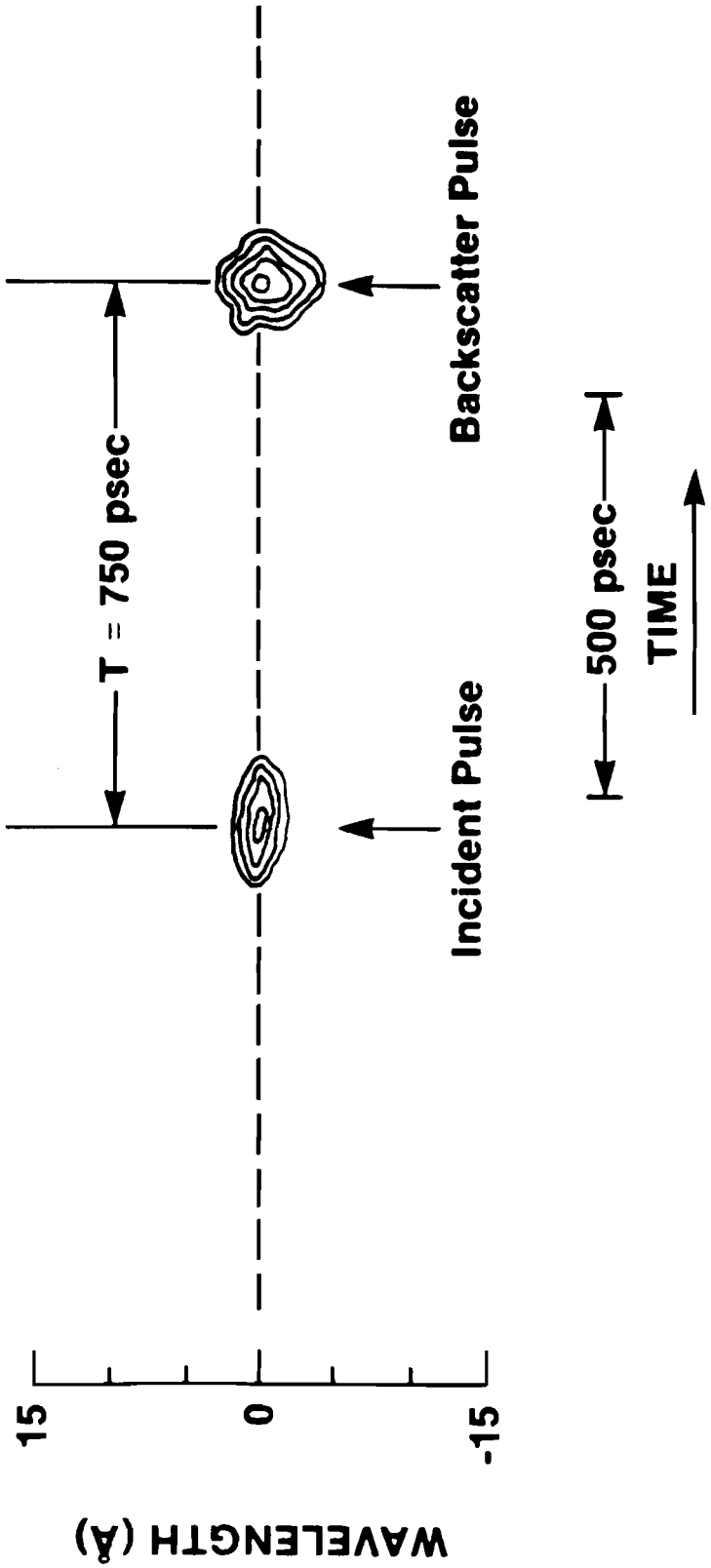


FIGURE III-6 Time calibration with short pulse

### 3. Specularly Reflected Light Spectroscopy.

Specularly reflected light from a 45° angled target was spectrally resolved by the same 1-m grating spectrometer as used in the time resolved spectroscopy. The reflected light was collected by an f/4 quartz lens at 90° and guided to the spectrometer. For this experiment no attempt was made to resolve the reflected light temporally. A 4 in. x 5 in. HSI film, sensitive at $\lambda = 3510$ Å, was placed at the output plane of the spectrometer. The same spectrometer setting was used; the spectral resolution was 0.7 Å.

### 4. Outline of Data Processing.

The film data of Brillouin experiment was digitized by a I I S digitizer. The digitized data was then processed by a Cyber 175 computer with the appropriate programs to eliminate certain spatial distortions,[71] and convert the recorded optical density (O.D.) to intensity (I). The data was then presented in the form of iso-intensity contours. This routine was developed by Dr. W. Friedman, LLE, University of Rochester. Overall "O.D. versus Log I" relation of the film through the streak camera was measured by making use of the multiple backscatter pulses of 1/2 intensity step. This data was utilized to convert the O.D. of the film to the intensity during the computer data processing. All the temporally and spectrally resolved data were thus converted to the form of iso-intensity contours.

# IV - I. EXPERIMENTAL RESULT : RAMAN SCATTERING.

## A. SYNOPSIS OF RAMAN SCATTERING EXPERIMENT.

Scattered light between 4000 and 7000 Å was studied from UV laser-produced plasmas. Measurements clarified differences between the absolute and convective Raman and the $2\omega_{pe}$ instabilities through their threshold and saturation behavior. Evidence was found of density profile steepening near $n_c/4$ from the relative thresholds of the absolute and convective Raman instabilities. Comparison between the predicted and the observed spectral shapes supported the profile steepening argument. It is shown in the model spectra that spectral peak position is a function of the coronal temperature.

## B. EXPERIMENTAL RESULT : RAMAN SCATTERING.

The dependence of the backscatter spectra on the laser inensity is shown in Fig. IV-1. CH targets ($10^{o}$) were irradiated with UV 450 psec pulses. Curves (a) and (b) correspond to near threshold intensity and 3 times threshold, respectively. Two distinct spectral components can be seen in the spectrum at a laser intensity of $4.4 \times 10^{14}$ W/cm$^2$ (10 % above the SRS threshold) in curve (a). The small bump at $\lambda$ = 7026 Å, corresponds to the $\omega_L/2$ spectral emission generated at $n_c/4$ by the absolute Raman instability. Other spectral features develop from 5000 to 5500 Å, which we attribute to the emission from the convective Raman instabilities. As the laser intensity is increased to $1.2 \times 10^{15}$ W/cm$^2$ in curve (b), the spectrum in the 7000 Å region grows about the initial spectrum. The spectrum between 4500 and 6100 Å illustrates that the convective Raman instabilities grow further. The noticeable emission at 4500 Å can be related to the lower bound of the plasma density where the SRS is still operative, by using the frequency matching condition ($\omega_L = \omega_{SRS} + \omega_{ep}$). The corresponding plasma density to $\lambda_{SRS}$ = 4500 Å is 0.05 $n_c$ ($n_c$ : critical density). The spectra in this figure were confirmed to have the same polarization as the incident laser as will be shown ; see Fig. IV-5. This strong polarization dependence is attributable to the direct scattering process from the SRS.

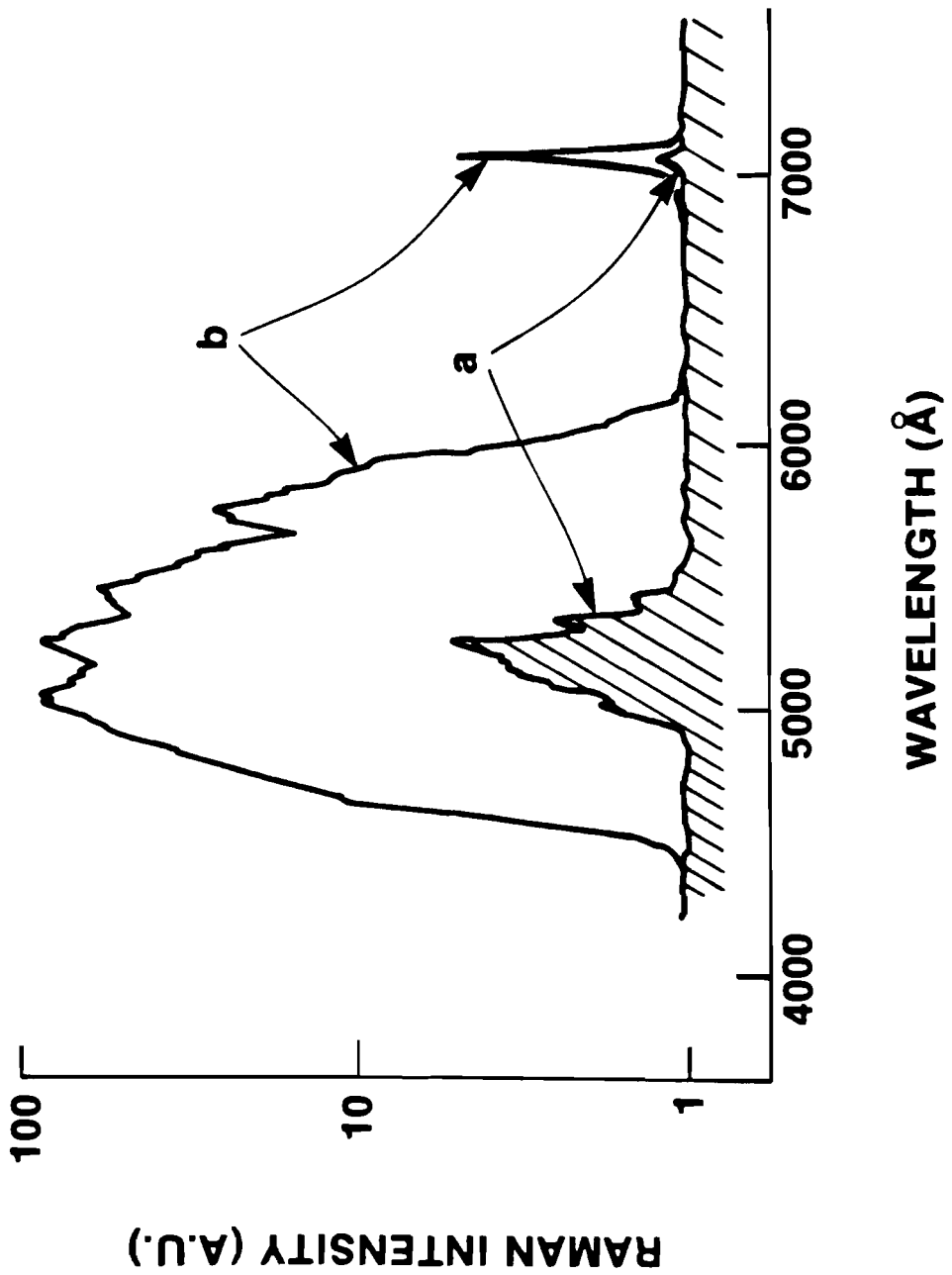


FIGURE IV-1 **Spectra of stimulated Raman backscattering from CH target**

The dependence of the Raman signal on the laser intensity is shown in Fig. IV-2. Curve (a) and (b) corresponds to the signal intensities at 7000 Å (absolute Raman instability) and 5000 Å (convective Raman instability). These data points have been deduced from the spectra recorded on film. Two curves exhibit the sharp threshold behavior for both absolute and convective Raman. Both Raman instabilities have the same threshold intensity of 4 $x10^{14}$ $W/cm^2$, and saturate at about 1.4 times the threshold laser intensity. The relative thresholds of the absolute and convective Raman instabilties will be discussed in terms of profile steepening in the next section (Chap. IV-C). At present no applicable theory has been found to explain the observed saturation.

The backscattered spectrum for Ni (Z = 28) as a function of the laser intensity is shown in Fig. IV-3. The cut-off at 4000 Å is due to the UV absorbing filter used to eliminate the secondary reflection of the laser light in the spectrometer. During the initial exeriments, when this data was taken, the residual GR intensity on target from the frequency up-conversion was $10^{-3}$ compared to the UV intensity. More importantly, the GR polarization plane was slightly tilted by $7^{o}$, even though the plane was supposed to be in the horizontal plane and to be perpendicular to the one of the UV beam for the maximum frequency up-conversion efficiency.[72] This GR light could become the seed for convective Raman instabilities, having the same polarization as the incident laser. In fact the residual GR is seen at $\lambda$ = 5270 Å in curve (a) taken at near the threshold intensity of $I_L = 8 \times 10^{14}$ $W/cm^2$. The convective instabilities appeared to start growing around the GR line.

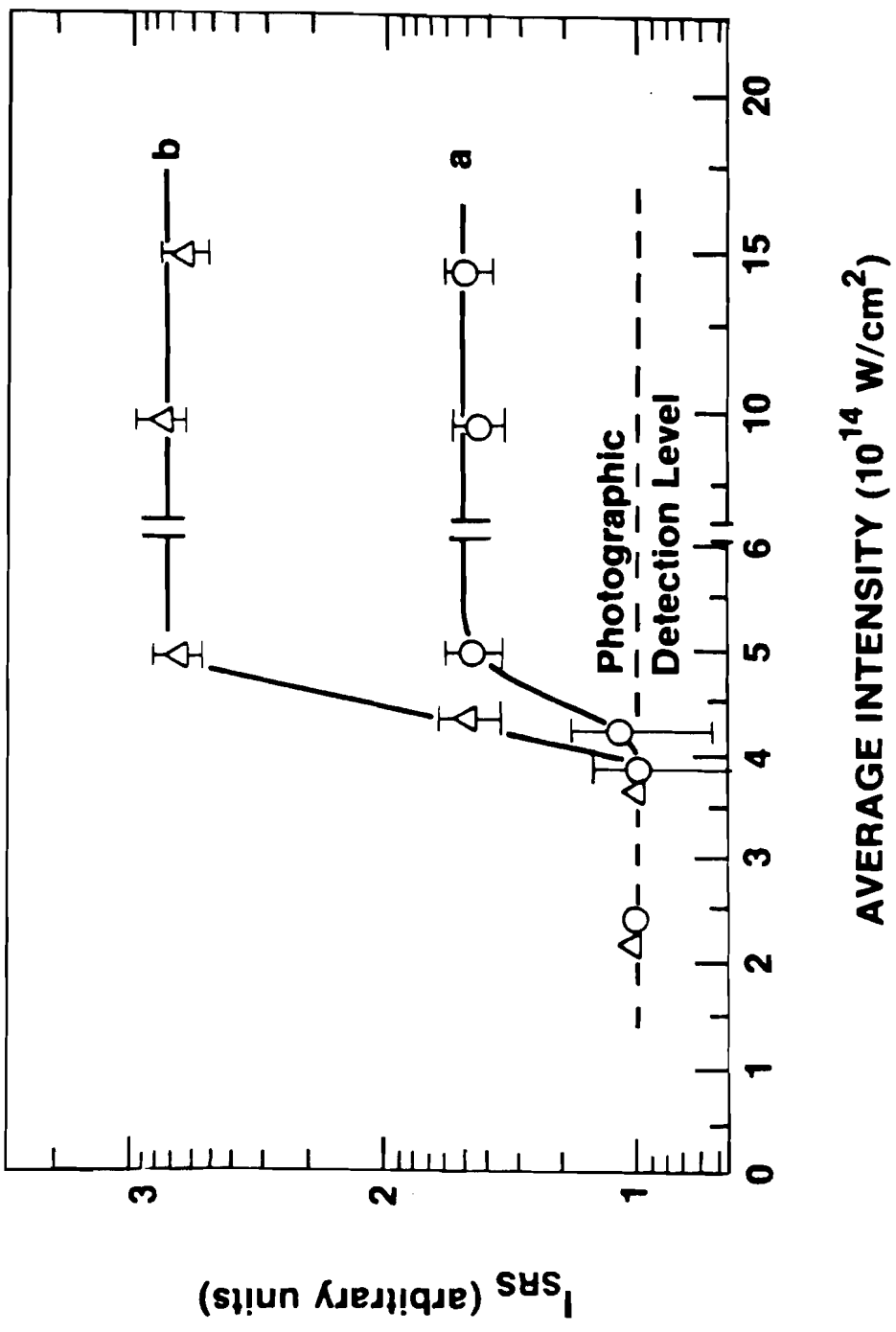


FIGURE IV-2 Spectral intensity versus laser intensity

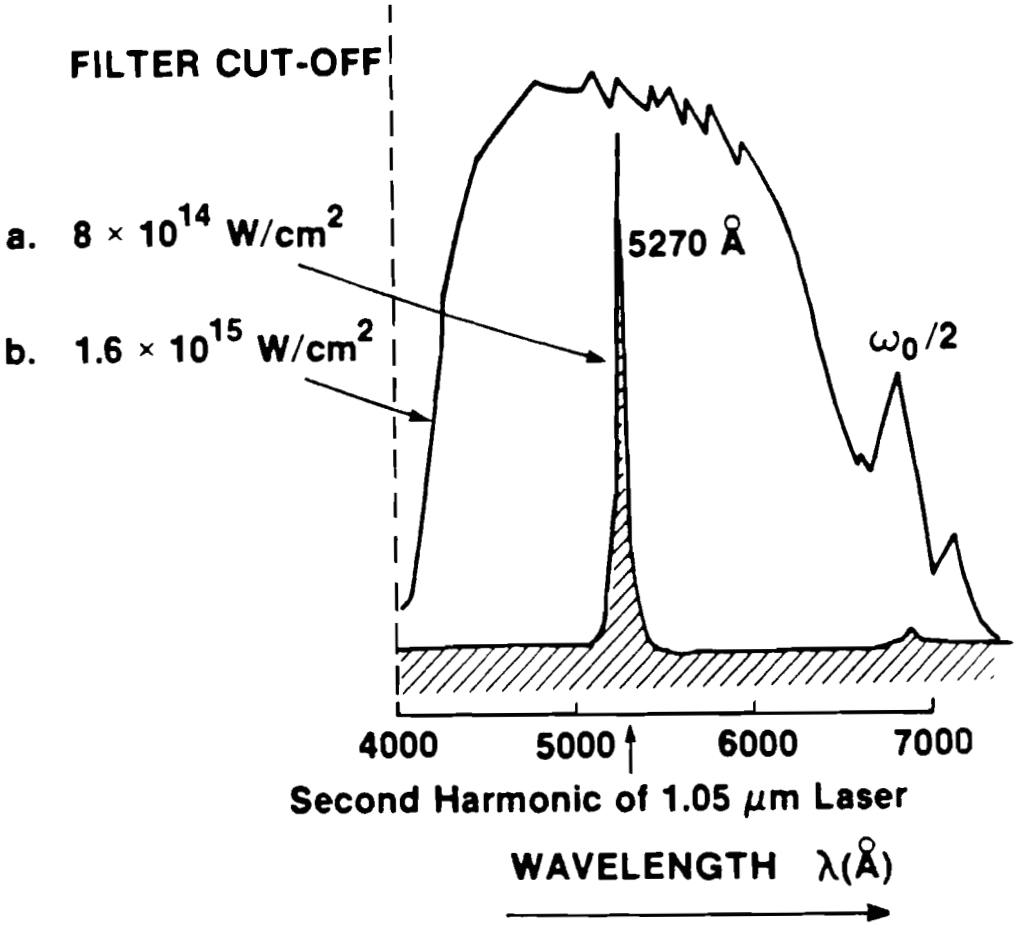


FIGURE IV-3 Spectra of stimulated Raman backscattering from Ni target at normal incidence

Curve (b) shows the spectrum at twice the threshold intensity. The convective Raman scattering no longer shows its dependence on 5270 Å line, but indicates the instabilities occuring in broad region below $n_c/4$.

Higher threshold intensities were observed for larger atomic number. No Raman spectrum was observed for Au targets. Since theory predicts higher threshold values for shorter density scale length,[57] our observations suggest shorter scale lengths for higher Z targets. This is consistent with hydro-dynamic simulations[73] which demonstrate slower expansions and thus shorter density scale lengths for higher Z. Since the possible existence of the artificially seeded convective Raman instability might complicate our interpretaion, one more UV mirror was added to increase the extinction ratio of UV/GR on target. In addition, the GR polarization plane was corrected not to have any parallel component to the UV. No difference was observed in the threshold intensity with the improved extinction.

To see the refraction of the Raman emission, the backscattered light from 45° target was spectrally resolved. Figure IV-4 shows the spectra for 0° and 45° angles of incidence. Laser intensities of $1.5 \times 10^{15}$ $W/cm^2$ on CH target were approximately the same for both cases. The spectrum from 6100 Å to 7000 Å disappeared for the 45° target, and this can be explained by evaluating the stronger refractive effect for the longer wavelength. The cut-off wavelength, i.e. the maximum wavelength observed at any particular angle is determined by evaluating the

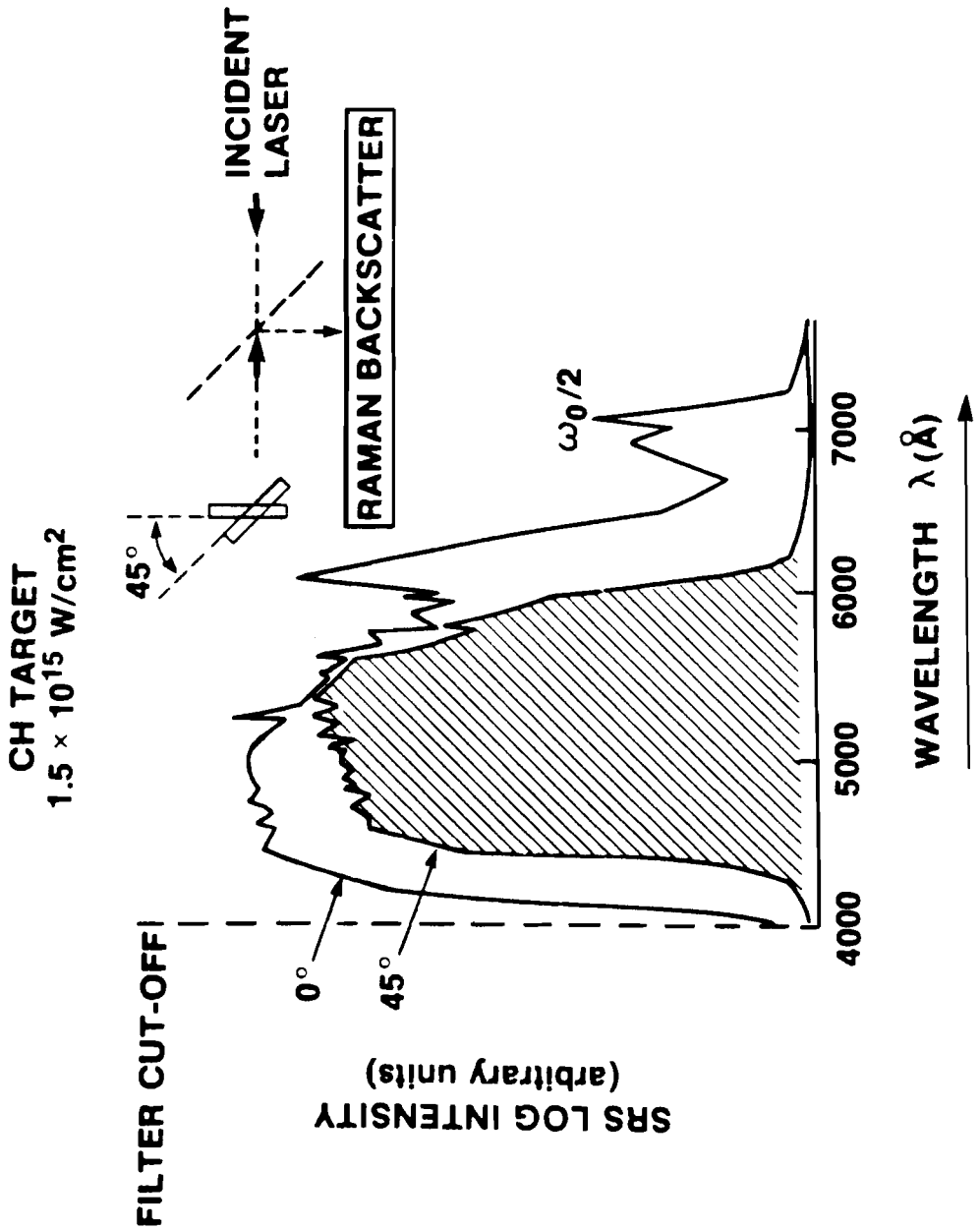


FIGURE IV-4 Raman backscatter spectra for 0 and 45 degree angle of incidence

dispersion relation of EM waves in both vacuum and plasmas; see APPENDIX 1. This leads to the relation :

$$\lambda_{SRS} = \lambda_L \cdot [\, 1 + \cos\theta \,] \qquad (1)$$

where $\theta$ is the observation (or incidence) angle with respect to the density gradient, and $\lambda_L$ is the laser wavelength. For $\theta = 45^o$, we calculate the cut-off wavelength $\lambda_{SRS}$ to be 6000 Å, which is in good agreement with the one shown in this figure. The observed decrease of the spectrum width on the shorter wavelength side was most likely due to the shot-to-shot fluctuation. A typical fluctuation of the order of 200 Å was observed in this region on several backscatter spectra from the $0^o$ targets.

Figure IV-5 shows the polarization dependence of the backscattered light spectra from CH target at an intensity of $8 \times 10^{14}$ W/cm$^2$. The polarization of the light was measured by inserting a 3" Al coated mirror into the main UV beam and reflecting the backscattered light directly to the spectrometer just as shown in Fig. IV-2. Two orthogonally oriented polarizers (HN 38) covered each half of the input slit of the spectrometer. The entire spectrum from 4000 to 7000 Å shows a strong polarization dependence. The observed polarization is the same as the incident polarization within the experimental contrast of 10 : 1, being consistent with the SRS. The pondermotive force in the SRS becomes maximum when both incident and scattered light has the same polarization. The depolarized light at 5270 Å is due to the GR light left over from the frequency up-conversion.

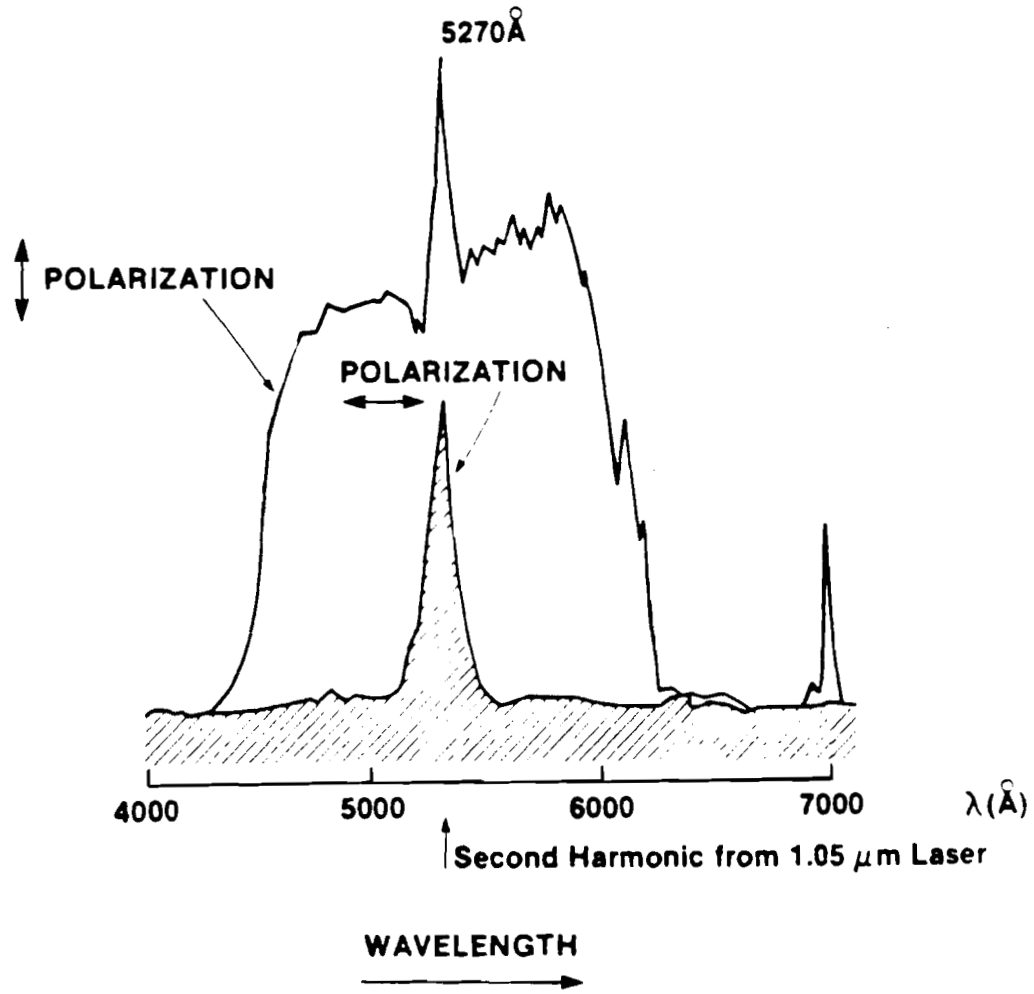


FIGURE IV-5 **Polarization dependence of Raman backscatter**

In accord with Snell's law, the angles of incidence ($\theta_1$) and refraction ($\theta_2$) are related by $n_1 \sin \theta_1 = n_2 \sin \theta_2$, where $n_1$ is the index of refraction of the first medium and $n_2$ is that of the second medium. If the first medium is taken as a region where light is generated and the second as vacuum, $\theta_1$ and $\theta_2$ correspond to the generated angle and the angle of observation, respectively. The observation angle $\theta_2$ of light generated at its own critical density becomes independent of the generated angle $\theta_1$ and should be normal to the target, since $n_1$ is zero. This should be true for $\omega_L/2$ emission at $n_c/4$. This was checked on the 45° target. The polarization was checked at the same time as shown in Fig. IV-6. The scattered light normal to the target (CH) was collected by an f/3 quartz lens. The polarization is the same as the incident laser for the spectrum from 4500 to 6800 Å, consistent with the polarization expected for the convective Raman instability. This portion of the spectrum disappears with a crossed polarizer, while the $\omega_L/2$ component is somewhat supressed. This implies that a significant portion of the $\omega_L/2$ light emitting normal to the target was depolarized.

The observed depolarization at $\omega_L/2$ in this experiment may be due to the increased collection efficiency. Since the collecting angle was changed from ± 2.4° (f/12) in the backscatter measurement to ± 9.4° (f/3), this increased efficiency could allow measurement of the depolarized light with improved sensitivity over that in the backscatter measurement. This assumption was supported by polarization measurements made with high sensitivity photodiodes at 7000 Å.

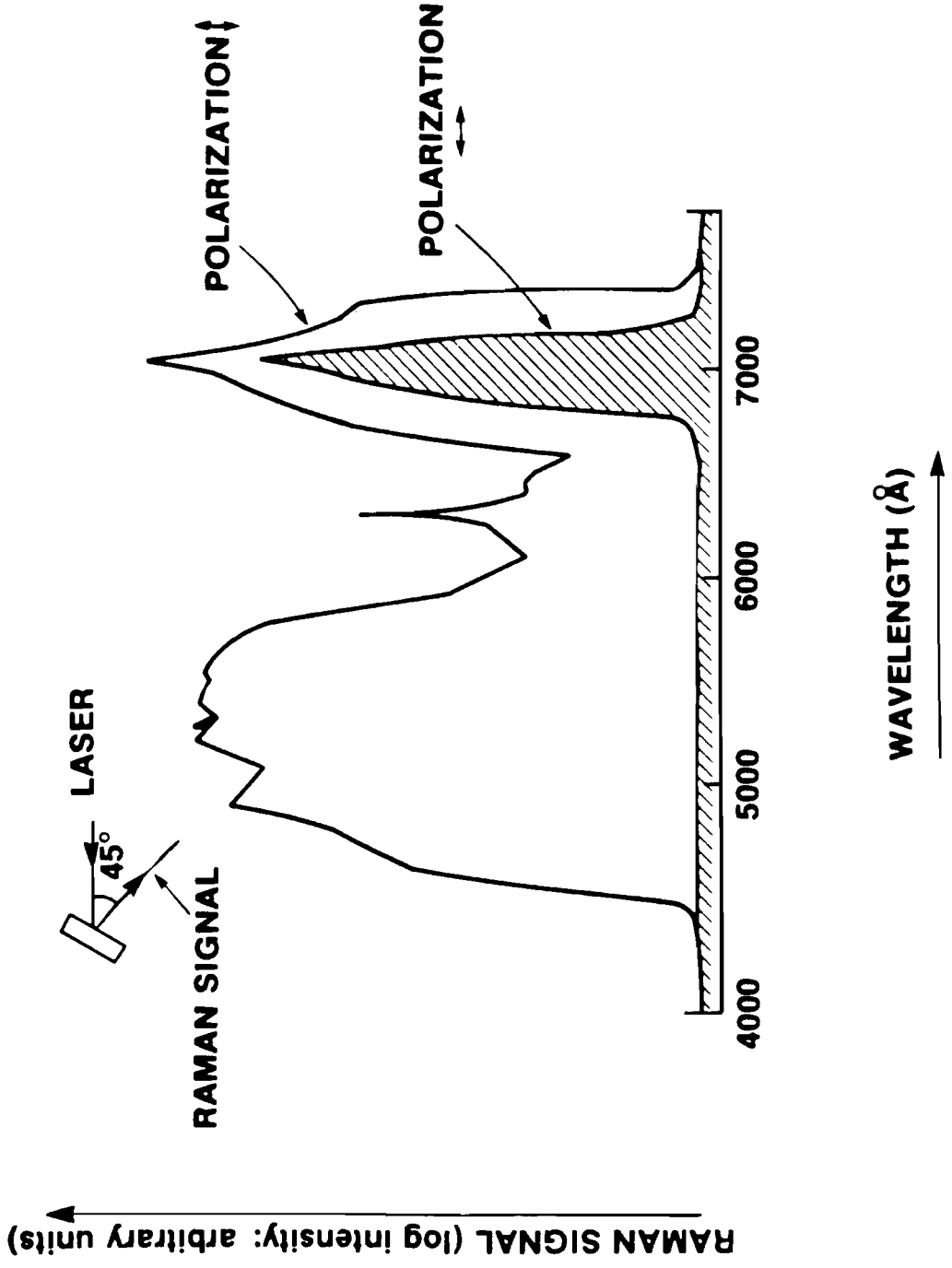


FIGURE IV-6 **Polarization dependence of Raman scattering from tilted CH target**

Figure IV-7 shows the intensity dependence of the fractional scattered light energy obtained with photodiodes absolutely calibrated at 7000 Å ($\omega_L/2$).[74] The photodiodes measured the angular distribution of the scattered light. The scattered energy was integrated over the observed angular distribution and then was normalized with the incident laser energy and the solid angle. Curve (a), linking the solid points, represents measurements of the scattered light with polarization parallel to the incident laser polarization. Curve (b) which links the open square, represents observations with opposite polarization. Two separate sharp increases are evident in curve (a) at $4 \times 10^{13}$ W/cm$^2$ and $4 \times 10^{14}$ W/cm$^2$, while curve (b) shows only the first rise. The laser intensity of the second rise coincides with the threshold of the absolute Raman instability shown earlier in Fig. IV-2. However the limited film sensitivity for the backscatter measurement did not allow one to see the first rise in curve (a) nor could it show the depolarization in curve (b) in this figure or in Fig. IV-6.

This first rise was attributed to the re-emission from the $2\omega_{pe}$ instability. The depolarization of the scattered light may be explained as follows. The $2\omega_{pe}$ light arises from a two-stage process, where the original photon decays into two plasmons of frequency very near $\omega_L/2$, which could then reconvert into photons with frequency $\simeq \omega_L/2$. Possible re-emission processes include direct conversion (the inverse process of resonance absorption[75]) and various three-waves scattering processes.[76] The excited EP waves in the $2\omega_{pe}$ instability are reflected in the plasma and then may lose their polarization dependence.

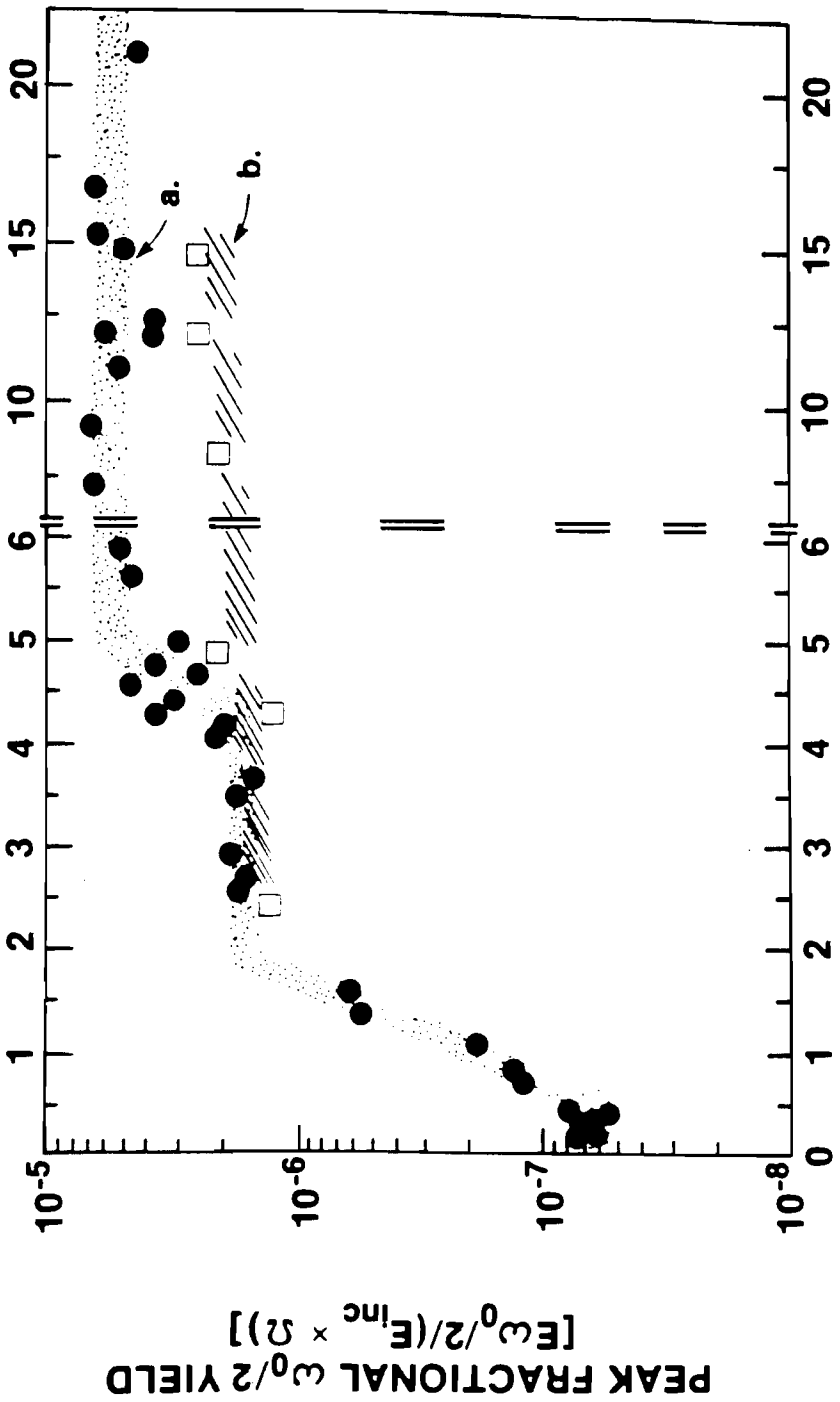


FIGURE IV-7 **Fractional backscatter energy at 7000 Å as a function of laser intensity**

This depolarized EP waves, when converted to EM waves, could lead to the observed scattering. The amount of scattered light at the saturated level was $6 \times 10^{-6}$ of incident energy.

All the laser intensities quoted so far are spatially and temporally averaged intensities. However the actual beam had hot spots. Magnified spatial images of a focal area were taken normal to a target, using the procedures described in Chap. III - C - (2). CH target was angled $45^{\circ}$ to the laser axis. Photographs were taken at near the Raman threshold of $4 \times 10^{14}$ W/cm$^2$ through a 7000 Å interference filter.

It demonstrated $\omega_L/2$ light originating from the localized regimes of the beam interaction region as shown in Fig. IV-8. This intensity distribution approximately corresponds to the intensity peaks observed in the laser beam.


FIGURE IV-8 Focal plane image of 7000 Å light

## C. DISCUSSION.

### 1. Comparison of Thresholds.

The convective Raman which grows in space as well as in time is a continuously increasing function of laser intensity. The threshold could be defined arbitrarily; Liu, for example, defined the threshold as the laser intensity which can give a Raman signal intensity of $e^{2\pi}$ (~535) times the noise level. In contrast, the absolute Raman instability mode, which is only unstable at its own critical density and consequently grows in time, has a clearer definition for the threshold. The threshold is the laser intensity at which the imaginary part of the frequency becomes larger than 0.

According to Liu[57], the intensity of convective Raman instability is given by

$$I_{SRS} = I_N \cdot \exp(2\pi G) \qquad (2)$$

where $I_N$ = background noise source and G = growth rate ; see Eq. II-(36) in Chap. II. E. Williams [77] has calculated the growth rate including the effect of Landau damping and as a noise level, assuming the black body emission from a typical 1 keV plasma. This result was corrected for opacity. Curves of the growth rate and the noise are shown in Fig. IV-9.

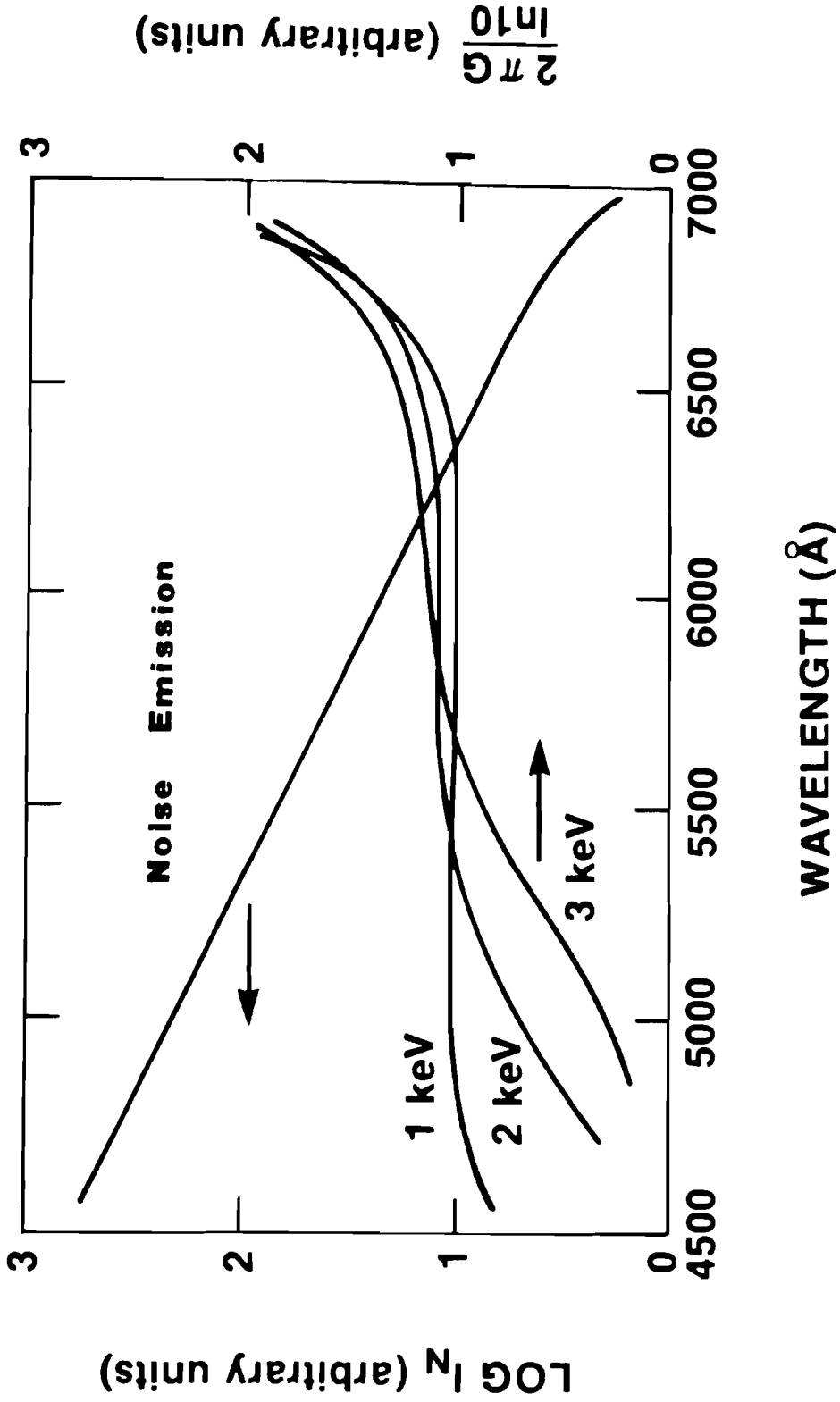


FIGURE IV-9 **Noise from black body thermal spectrum and gain for convective Raman instability**

In the figure, log $I_N$ and $2\pi G/\ln 10$ with three different electron temperatures are shown. The density scale length of 50 um and the intensity $I_L = 10^{15}$ W/cm$^2$ were used for the growth rate calculation. Landau damping becomes important when $k\lambda_d$ approaches 1; see Chap. II. With $\lambda_d \propto \sqrt{T_e}/n_e$, this implies that EP waves would be damped when density decreases or temperature increases. With the assumption of an iso-thermal condition in the corona region, Landau damping always starts from the underdense side for a certain temperature. This effect is seen as the quenching of the growth rate toward the shorter wavelength side in the figure. Here the growth rates are plotted for three different temperatures of $T_e$ = 1 - 3 keV. The opacity effect included is based on the inverse-Bremsstrahlung (IB) absorption nomalized to the measured absorption rate at the laser wavelength ($\lambda_L$ = 0.35 $\mu$m). The IB absorption increases exponentially with plasma density. This effect slightly enhances the slope of the black body emission vs. wavelength which is $1/\lambda^4$ in the Rayleigh-Jeans limit.[78]

In order to have a self-consistent calculation of the density scale length, the threshold for the convective Raman ($I_{conv}$) is defined as the laser intensity required for a convective gain of $e^{2\pi G} \simeq 50$ (ie. $G \simeq 0.6$), our best estimate of the instrumental detection threshold above the noise level; see APPENDIX 2. The constant factor in $I_{conv}$ in Table II - 1 is slightly modified for our use, since Liu (Ref. 57) has defined $I_{conv/Liu}$ to be the laser intensity for a convective gain of $G \geq 1$. The relation between re-defined $I_{conv}$ and $I_{conv/Liu}$ becomes

$$I_{conv} = 0.6\ I_{conv/Liu} \qquad (3)$$

By taking the threshold expression from Table II-1, we devide $I_{conv}$ by the absolute Raman instability theshold ($I_{abs}$) as follows.

$$\frac{I_{conv}}{I_{abs}} = 0.4 \quad \lambda_L^{-1/3} \quad \frac{L_{abs}^{4/3}}{L_{conv}} \qquad (4)$$

A factor 0.4 results from taking account the constant in the threshold expressions in the right column in the table.

Figure IV-2 indicates both absolute and convective instabilities have become equally measurable at the laser intensity of $4 \times 10^{14}$ W/cm$^2$. This simultaneous onset of the instabilities predicts $L_{abs}/L_{conv}$ to be $\cong$ 1/3 from Eq. (3), indicating significant profile steepening near $n_c/4$. The density profile steepening near $n_c/4$ could occur as a consequence of both $2\omega_{pe}$ and/or absolute Raman instabilities. Such steepening due to the pondermotive force generated by the intense plasma wave fields, was observed in $CO_2$ laser experiments by Baldis et al.[79] Mizuno et al.[80] showed the steepening at $n_c/4$ in microwave experiments. Langdon et al.[81] in their computer simulation found the density scale length to be 5 times steeper than the initial one due to this locally exerted pondermotive force.

## 2. Examination Of Spectral Distribution.

Additional evidence for profile steepening at $n_c/4$ can be obtained from a close examination of the spectrum shown in curve (b) of Fig. IV-1. We calculated model spectra based upon the gain and the noise curves in Fig. IV-9. These are shown in Fig. IV-10. The spectral intensity plotted in this figure may be compared directly with Fig. IV-1, whose ordinate is also plotted logarithmically. Curve (a) shows a spectrum near the detection threshold and curve (b), at 2 x the threshold. The dotted spectrum is the convective part of the observed spectrum at three times threshold; see Fig. IV-1. The observed spectrum produced well above the threshold (the dotted curve in the figure) shows significant difference from the model spectrum curve (b), particularly in the spectral region between 6100 and 7000 Å. We interpret this minimum in the convective spectrum as due to a suppression of the convective Raman between 0.2 and 0.25 $n_c$. This could arise from a steeper density gradient in this region compared to the lower density region.

As another feature, the model spectrum shows a spectral peak which is a function of the background temperature. This is shown in Fig. IV-11. These three curves parametrized by temperature are near the detection threshold. Our observed peak at 5200 Å in Fig. IV-1 suggests that the coronal temperature is between 1 and 2 keV. Electron

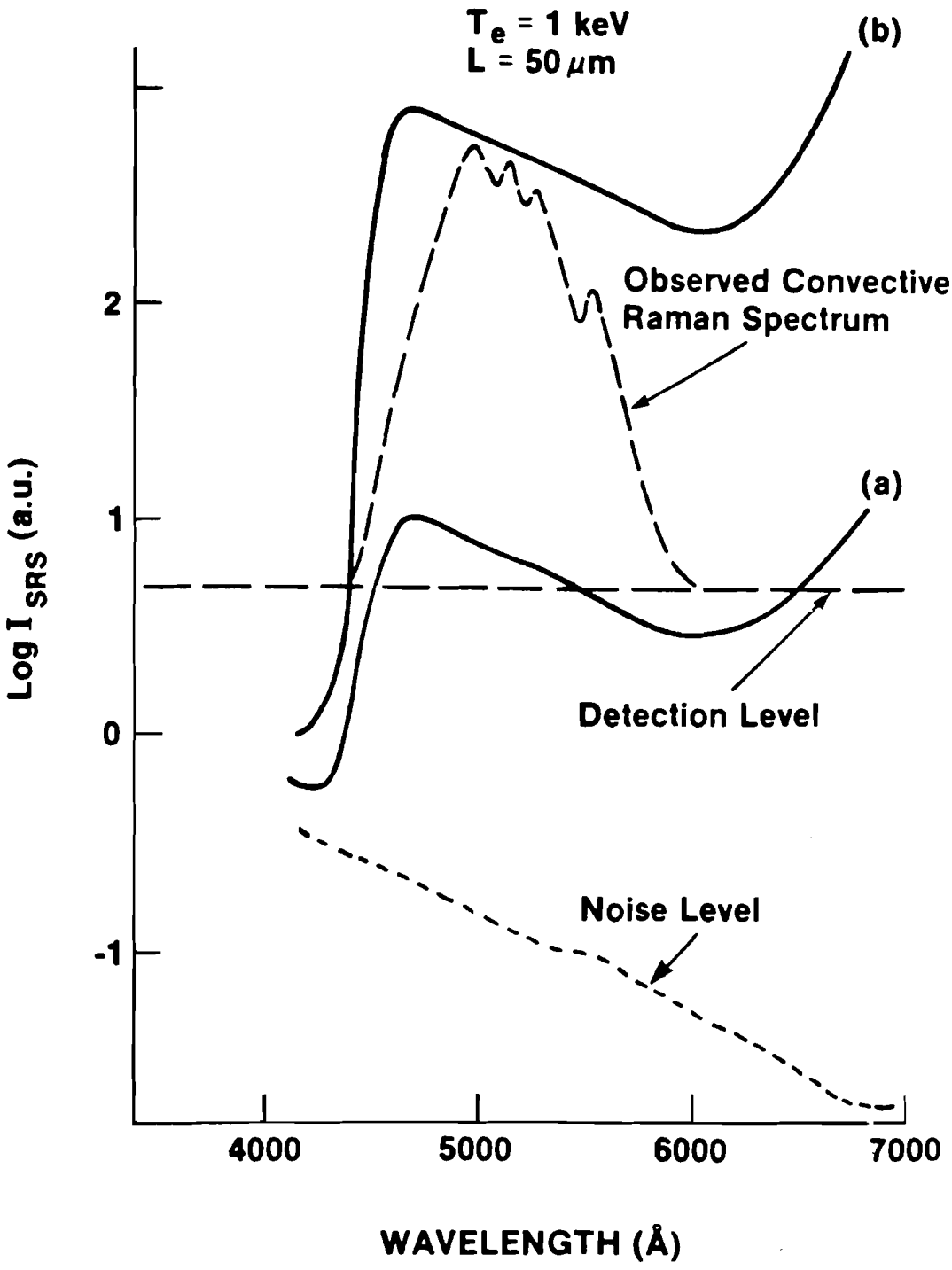


FIGURE IV-10 **Convective Raman model spectra**

temperature measured from the x-ray line ratio of Si 1s-2p/$1s^2$-1s2p showed the typical of $T_e$ = 1 keV under the similar experimental condition.[82] Two dimensional computer simulation predicted the coronal temperature ranging from 1 to 2 keV for these UV laser intensity regions.[83] This temperature range is also consistent with the interpretation of our Brillouin scattering described in the next section.

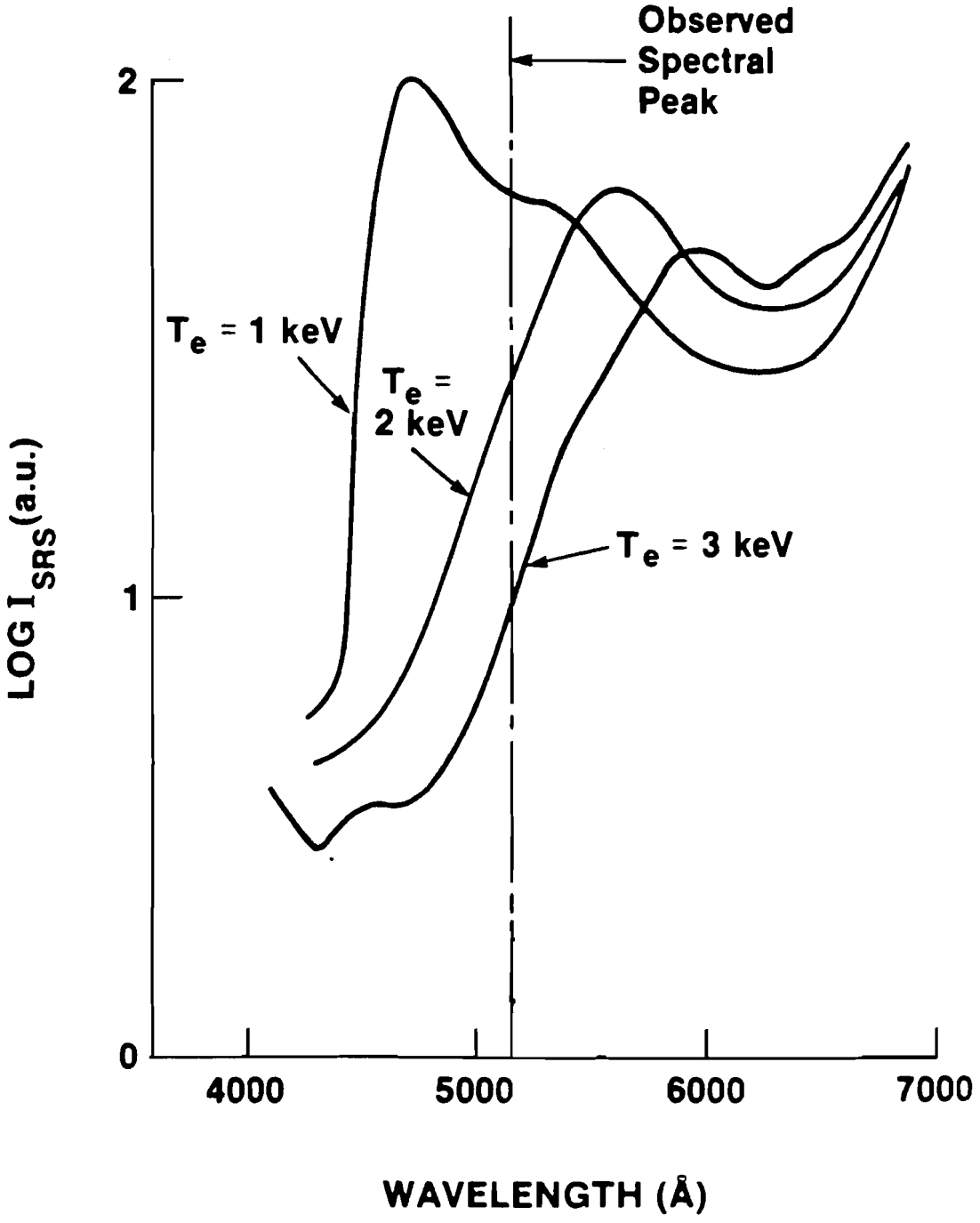


FIGURE IV-11 **Model Raman spectra near threshold**

### 3. Theoretical and Observed Thresholds.

Our observed threshold values for the $2\omega_{pe}$ and the SRS instabilities are $4 \times 10^{13}$ W/cm$^2$ and $4 \times 10^{14}$ W/cm$^2$, respectively. Here the laser intensities are average values, while the instabilities will grow from the peak intensities within the focal spot as shown in Fig. IV-8. These peak intensities were estimated from x-ray pin hole camera images to be four or five times higher. Thus using peak intensities and a temperature typically, of $T_e$ = 1 keV, the threshold equation for the $2\omega_{pe}$ from Table II - 1,

$$I_{2\omega_{pe}} = 5 \times 10^{12} \frac{T_{eV}}{L_\mu \lambda_\mu} \qquad (5)$$

gives

$$L_{2\omega_{pe}} = 60 \sim 70 \quad \mu m \qquad (6)$$

$L_{abs}$ = 100 - 140 μm and $L_{conv}$ = 270 - 400 μm are obtained similarly applying the observed threshold values of both absolute and convective Raman instabilities to the formulae in Table II-1. Two-dimensional hydro-code calculations predict the scale lengths at $n_c/4$ to be between 50 and 70 μm. Thus scale lengths from the $2\omega_{pe}$ instability tend to be shorter and be in more reasonable agreement with the hydro-code calculation than those of SRS. There should not be a strong enough pondermotive force to cause density steepening, at the $2\omega_{pe}$ instability

threshold. Comparison of the observed data and existing theory for the Raman instabilities requires scale lenghs twice as long as hydrodynamic model predicted at $n_c/4$ and even longer ones (5 - 8 x) below $n_c/4$.

Filamentation in the plasma could be an attractive candidate to explain higher effective intensities and longer scale lengths inside the plasma. In our experiments, the strongly collimated light from tilted targets was observed at the target normal within $\pm 12^{o}$ for the absolute Raman instability, and within $\pm 20^{o}$ for the $2\omega_{pe}$ re-emission.[74] This is inconsistent with the filamentation, since filamentation would be expected to have scattering more dependent on the incidence angle of laser beam than on the observation angle to target normal.

GDL U.V. laser system was converted for longer pulses of 1 nsec after a series of experiments with 450 psec pulses. When the angular distribution of the 7000 Å scattered light from tilted targets was observed, however, two independent lobes were indentified[74]: one normal to the target, and other along the backscatter path. This latter lobe of the 7000 Å light, strongly dependent on the incidence angle of laser beam, may originate from filamentation. Filamentation may be more easily formed under the condition of longer scale lengths expected for longer pulses.

Here we consider an alternative plausible model to explain the scattered light normal to the target with the long density scale lengths estimated. This is based on the fact that the instabilities at and below $n_c/4$ have growth regions of length " $\ell$ " such that

$$\ell^2 \cdot K' \geq \pi \qquad (7)$$

"$\ell$" can be expressed as;

$$\ell \simeq \lambda_d \cdot \left( 6\pi \, k_L L_n \right)^{1/2} \qquad (8)$$

$$\left( K' = \frac{dK}{dx} \;, \; \because K = k_{0x} - k_{1x} - k_{2x} \right)$$

and "$\ell$" is estimated to be a few microns for $L_n$ = 50 - 70 μm ( $\ell \ll L_{abs}$, $L_{conv}$). We postulate much shorter local regions than the typical scale lengths. There the density gradients are shallower than implied by the overall scale length. Such modulated density could easily arise from density fluctuations produced near $n_c$ which then propagate down the density gradient through the region at $n_c/4$.

## D. CONCLUSION

Scattered light from parametric instabilities between 4500 and 7026 Å was measured with the use of photodiodes and spectrometers. Laser intensities ranged from $10^{13}$ to 3 x $10^{15}$ W/cm$^2$ with 450 psec pulses.

The $2\omega_{pe}$ instability was found to have its threshold at 4 x $10^{13}$ W/cm$^2$. The convective and absolute Raman instabilities, which could be distinguished by the spectral range of the scattered light, had the same threshold intensiy at 4 x $10^{14}$ W/cm$^2$. This equal threshold for both Raman instabilities implied the density profile steepening at $n_c/4$. Comparison between the predicted and the observed Raman spectral shapes showed the suppression of the convective Raman instabilities from 0.2 to 0.25 $n_c$, indicating that the suppression was due to the steeper density scale length in this region. It was shown also in the model spectra that the spectral peak position was a function of the background coronal temperature. From the observed spectral peak around 5000 Å, a temperature of 1 - 2 keV was suggested.

## IV - II. EXPERIMENTAL RESULT : BRILLOUIN SCATTERING

### E. SYNOPSIS OF BRILLOUIN EXPERIMENT.

Backscattered light was resolved temporally and spectrally from UV laser-produced plasmas at intensities of $10^{13}$ to 2 x $10^{15}$ W/cm$^2$ and a pulse duration of 450 psec. Targets were planar CH, Ni, and Au. The combination of a 1 - m spectrograph and a picosecond streak camera gave a spectral resolution of 1 Å with a temporal resolution of 40 psec.

In the backscatter spectra, we identified two distinct contributions: a stimulated Brillouin scattering (SBS) component clearly seen from tilted targets and a second component seen in specular reflection, which we attributed to modulational instability.

Backscatter measurements at 5 x $10^{14}$ W/cm$^2$ on CH targets tilted more than 20$^o$ to the laser beam showed relatively narrow, red shifted spectra (typically 5 Å FWHM with 1 to 3 Å red shift). The data were consistent with SBS from a region of plasma flowing with approximately Mach 1 with a temperature of 1 to 2 keV.

The backscattered spectra from targets normal to the laser, which includes a specular component, showed much larger widths (13 - 15 Å FWHM) near 2 x $10^{15}$ W/$cm^2$. Similarly broadened spectra were observed from specular reflection from 45° oriented targets. This broadening was attributed to modulational instability.

## F. EXPERIMENTAL RESULT: BRILLOUIN SCATTERING.

Typical data in our backscatter measurements are shown in Fig. IV-12. CH target angled $10^{o}$ to the laser axis was irradiated by UV laser ($\lambda_L$ = 0.35 μm) at a laser intensity of $1.6 \times 10^{15}$ W/cm$^2$. The figure consists of three temporally and spectrally resolved pulses. The first one (left) is an incident pulse. The first (middle) and the second (right) backscatter pulses are the same except the intensity is reduced by 1/2 between them. These two backscatter pulses were created with the use of an etalon consisting of two partially reflecting mirrors; see Chap. III, p 45. They are separated by the time required for the light to travel between two mirrors. The incident pulse was introduced ahead of the backscatter pulse to give a spectral and temporal fiducial mark. The spectral fiducial is seen as the distinctively narrow spectrum of the incident pulse. The temporal fiducial can be addressed in each backscatter pulse by means of the time calibration scheme described in Chap. III - D - (2). The corresponding position of the incident peak is indicated in the backscattered pulses.

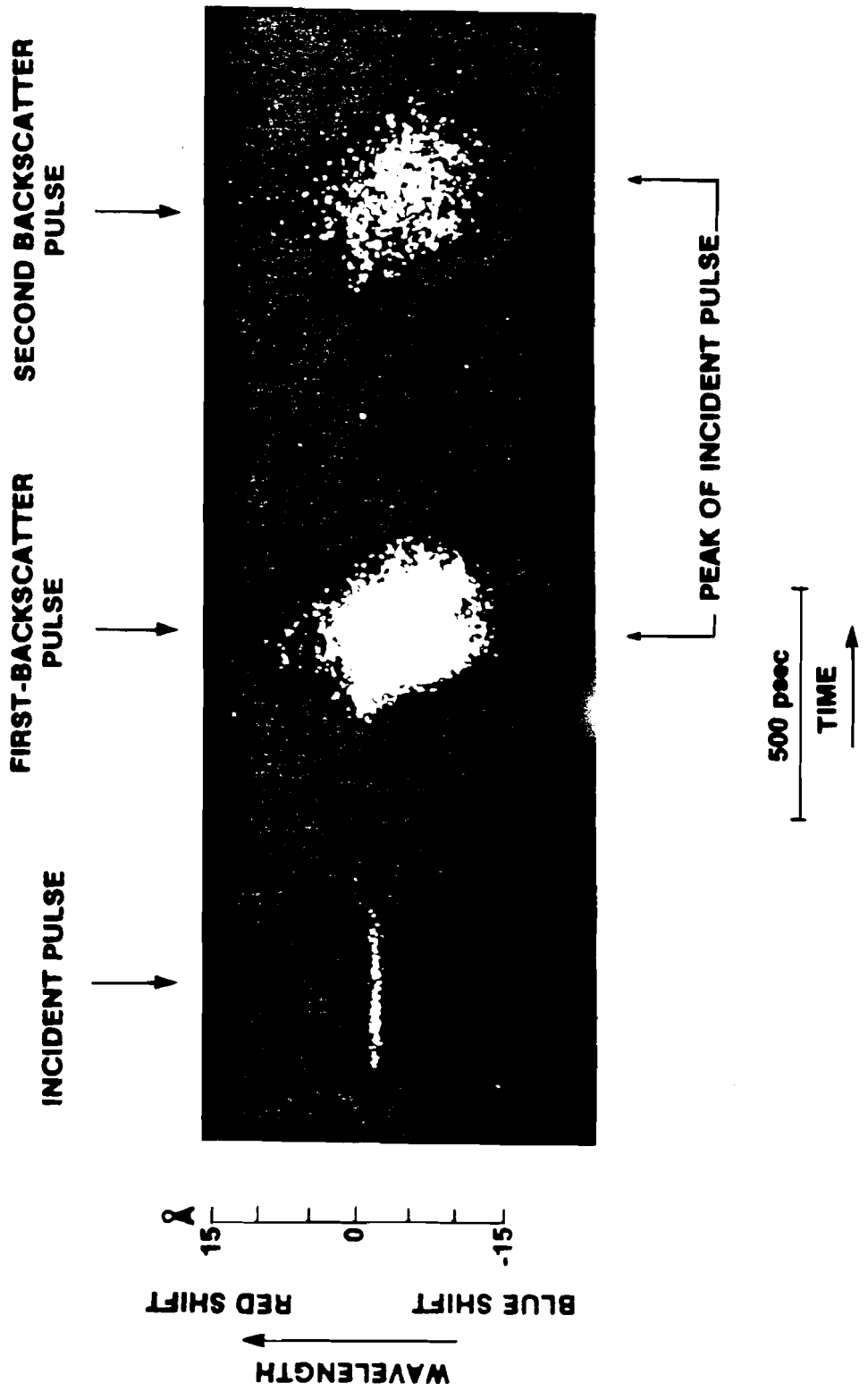


FIGURE IV-12 Typical time resloved backscatter spectra

Figure IV-13 shows the backscatter spectra from CH targets at different angles. These were taken at laser intensities of $2 - 5 \times 10^{14}$ W/cm$^2$. Optical densities in the raw data have been converted to intensties according to the procedures in Chap. III - D - (4), and are displayed as an iso-intensity contour plot. The backscattered pulses in this figure are from three different target shots. The positions of the peaks of the incident pulses are indicated by arrows, while the broken line indicates the original laser wavelength.

Backscattered light from the $0^o$ target shows a gradual broadening around the spectral peak in time. The broadening as well as the spectral shift becomes maximum at the time of the incident pulse peak. Maxima of 9 - 10 Å broadening and 7 - 9 Å peak shift toward the short wavelength side were typically observed.

In this thesis, we would like to define the verb of "shift toward the short wavelength side" as "blue-shift", and vice versa as "red-shift" to avoid a lengthy sentence.

When the target angle is increased from $0^o$ to $22.5^o$, the spectrum changes noticeably. The spectral component largely blue-shifted in the $0^o$ case vanishes for the $22.5^o$ case. The spectral peak on the $22.5^o$ target is even slightly red-shifted by $\cong$ 1 Å. The $45^o$ case is similar to the $22.5^o$ case, but the entire spectrum is red-shifted further by 0.5 - 3 A. Data from both $22.5^o$ and $45^o$ targets also show narrower spectral widths compared to the $0^o$ targets. If the spectral peak (the centroid)

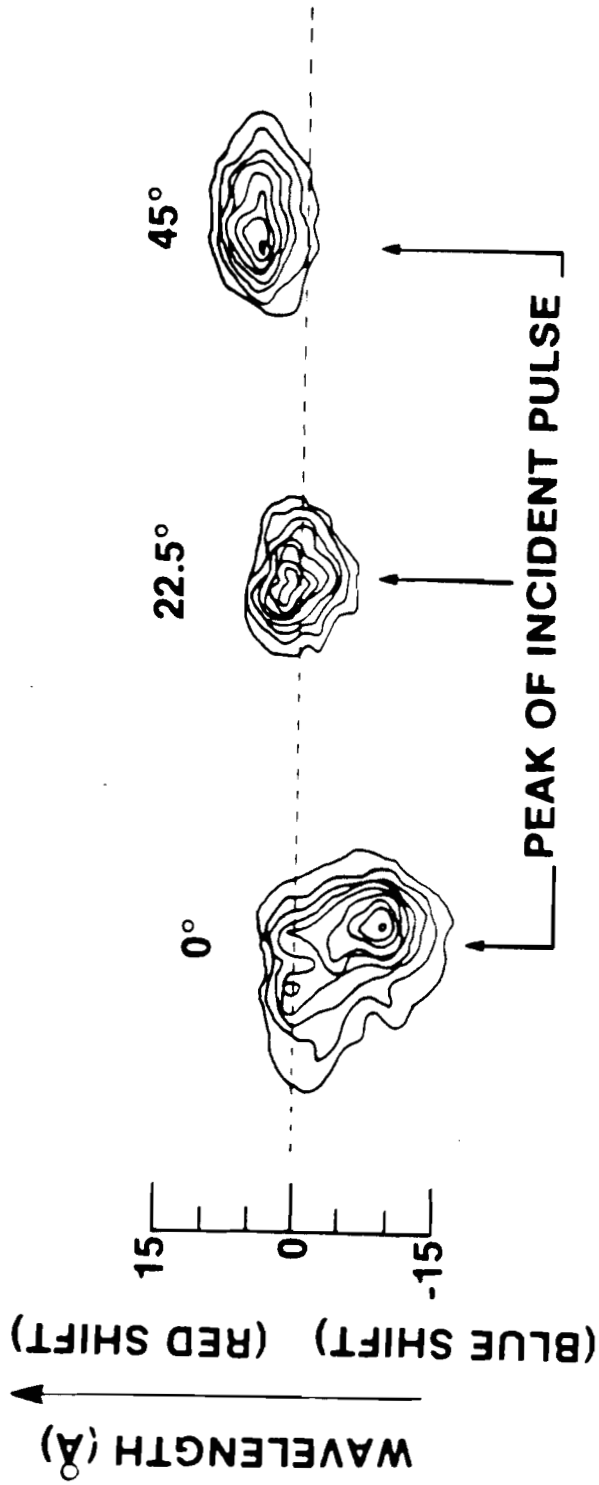


FIGURE IV-13 **Backscatter spectral dependence on target angle in iso-intensity plot**

and the width (FWHM) of Fig. IV-13 are re-plotted with a 100 psec interval, one may see the trend described above more clearly. This is shown in Fig. IV-14. No red-shift is observed for the $0^{o}$ target in Fig. IV-13 or Fig. IV-14, while the other two cases show a larger red-shift with increasing target angle. This invokes the Doppler shifts, which decrease as $\cos\theta$ ($\theta$: target angle) for one-dimensional plasma expansion. The red-shift may be reduced by the Doppler effect from an outward moving plasma. Since the plasma blow-off in our experiment is likely to be one-dimensional and normal to the target surface within length comparable to the focal size (typically 100 - 300 μm dia.), the larger target angle should show less Doppler effect, which is consistent with the figures.

A qualitative measurement of the angular distribution of the backscattered light was made using a photosensitve paper placed around the focusing cone, 5 cm from the target. A strongly collimated ($\pm 11^{o}$) pattern of the direct backscattered component was exposed on the paper when a CH target tilted more than $22^{o}$ was irradiated at a laser intensity above $2 \times 10^{14}$ W/cm$^2$. The spectral red-shift and the strong collimation of the backscatter from angled targets are considered to be characteristic of SBS.[24]

Dependence of the SBS component on target atomic number (Z) is shown in Fig. IV-15. CH (Z = 4) and Au (Z = 79) targets, oriented $45^{o}$ were irradiated at a laser intensity of $I_L = 1.2 \times 10^{14}$ W/cm$^2$ with 450 psec pulses. Backscattered pulse durations are 190 psec (FWHM) for the Au

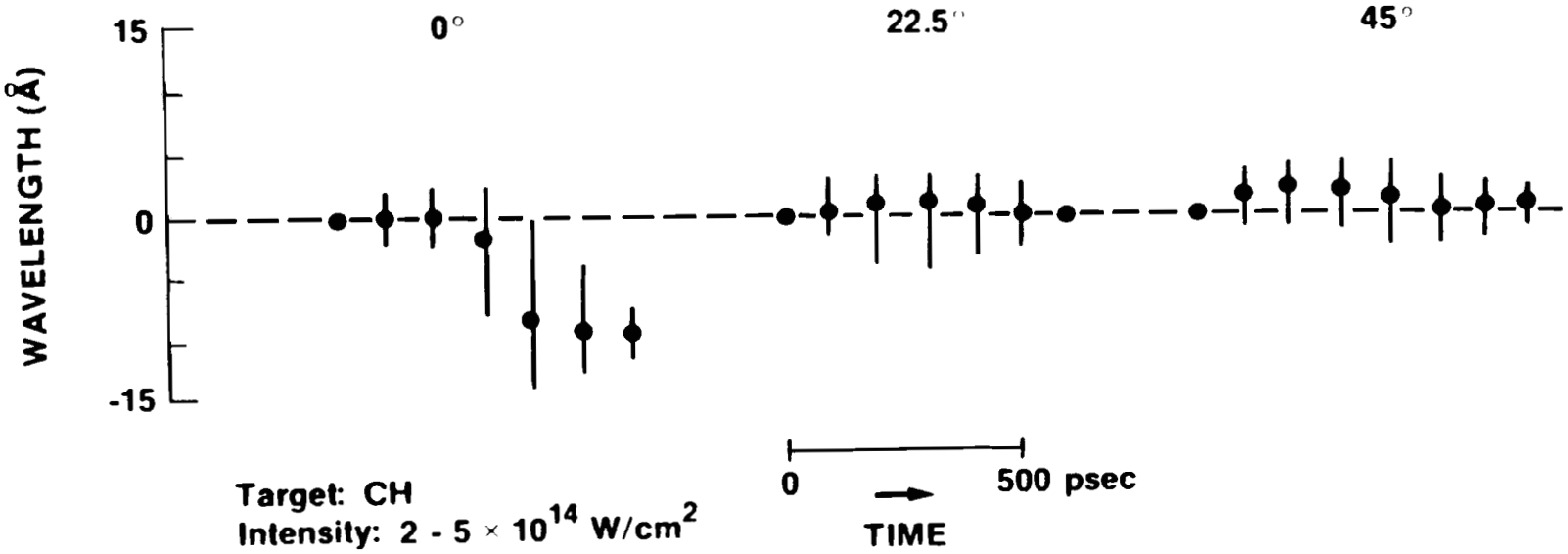


FIGURE IV-14 **Backscatter spectral dependence on target angle**

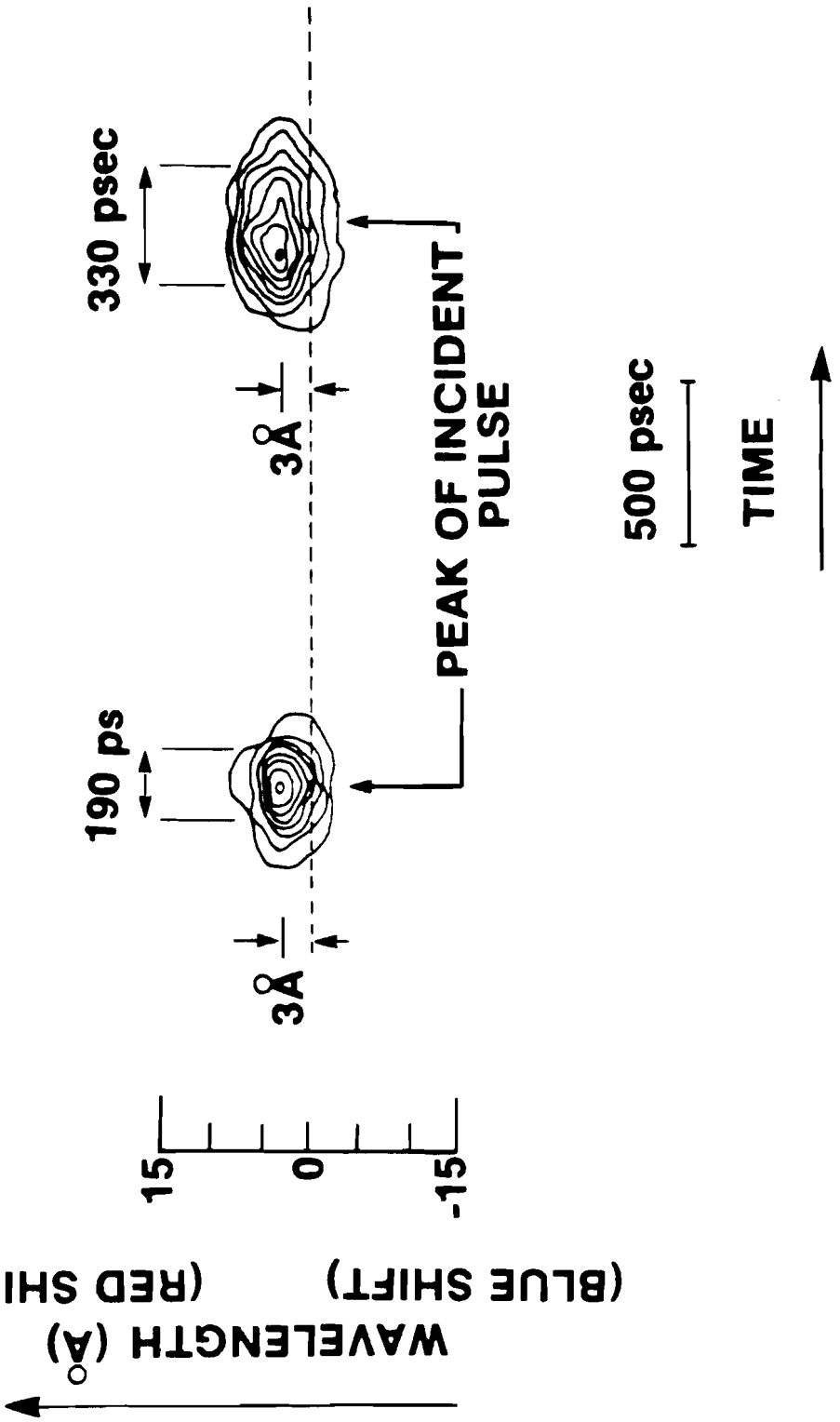


FIGURE IV-15 Backscatter spectral dependence on target atomic number

target and 330 psec for the CH, both showing a 3 Å red-shift. The intensity peaks of these backscattered pulses coincide with that of the incident pulse. The characteristic, shorter pulse duration of the SBS component for higher Z number was quite reproducible.

This may be consistent with the observed higher absorption of UV laser light in plasmas for higher Z target.[84] Seka et al. concluded that the dominant absorption mechanism was inverse-Bremsstrahlung (IB), which increases with Z. IB becomes maximum at the plasma critical density, where SBS has the lowest threshold. The pump (incident) laser intensity for SBS may become more absorbed and thus weaker for higher Z around the critical density. Another plausible explanation for the Z dependence is based on the computer simulation which has predicted a shorter density scale lengths for higher Z targets.[73] The SBS threshold is inversely proportional to the scale length. Consequently the SBS onset time for higher Z could be delayed and be cut off earlier because of the predicted shorter scale length. In the above arguments, a combination of these mechanisms could well be responsible for the shorter duration of the SBS component.

Figure IV-16 (intensity contour plot) and IV-17 (plot of the centroid and spectral width at 100 psec time intervals) show a typical development of the backscatter spectrum, including a specular reflection as a function of laser intensity. CH targets were oriented at 10°.

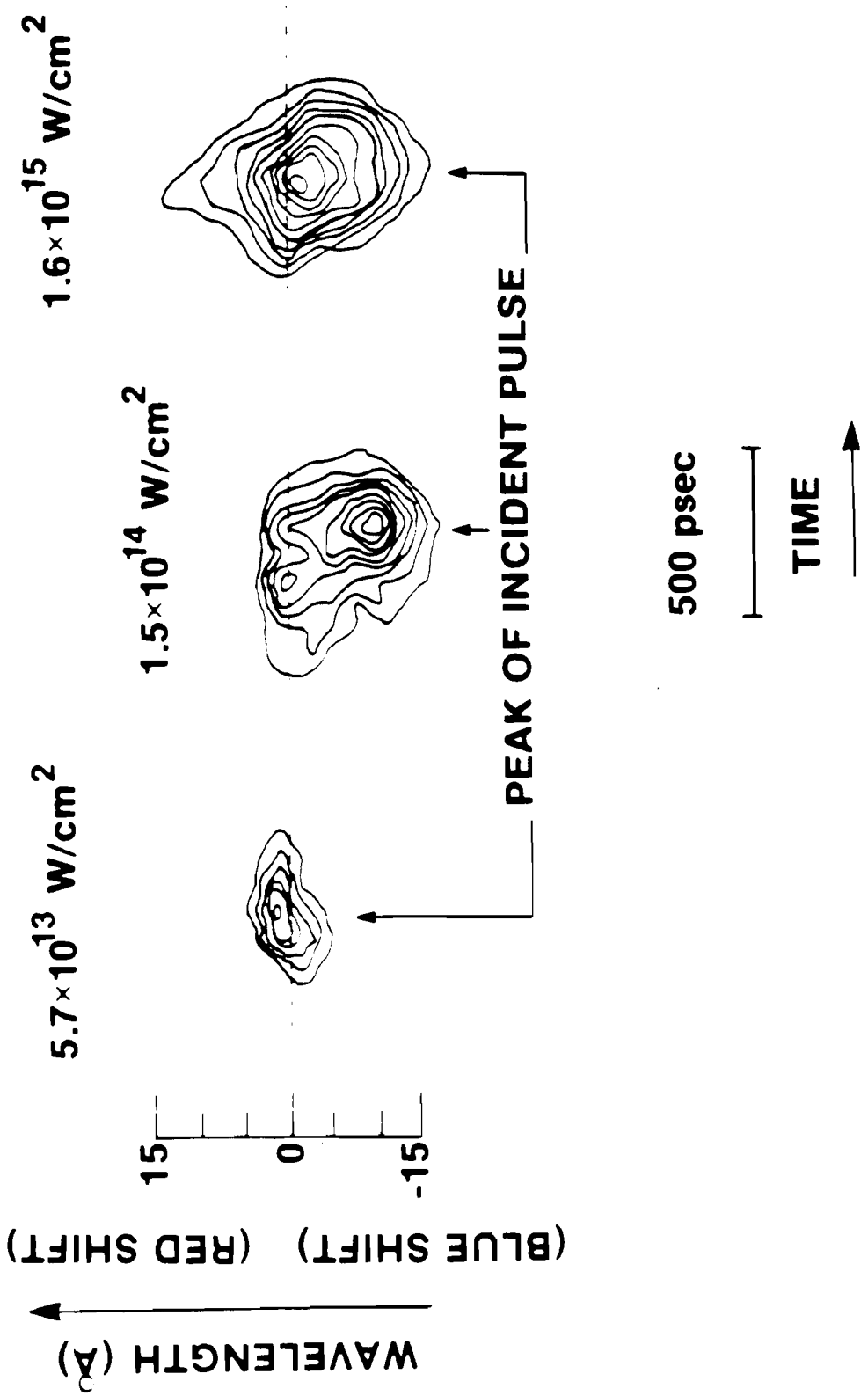


FIGURE IV-16 Time resolved backscatter spectra (iso-intensity plot) as a function of laser intensity

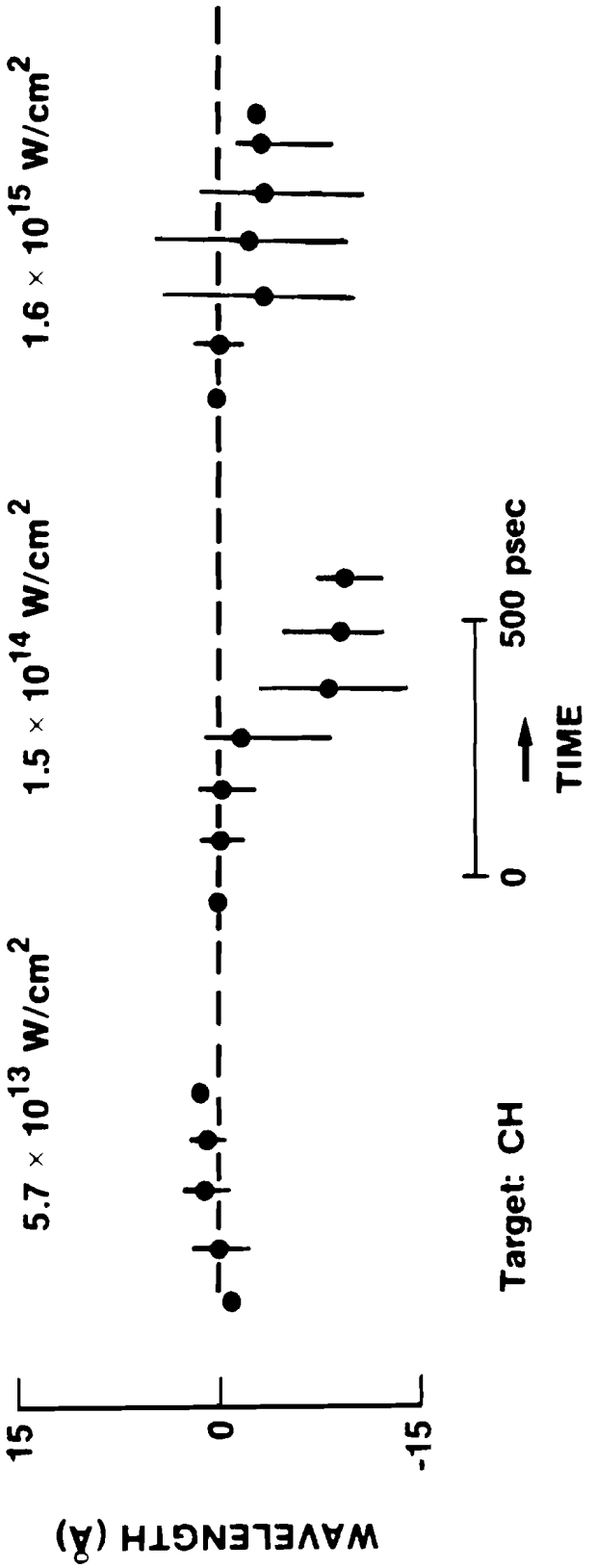


FIGURE IV-17 Time resolved backscatter spectra as a function of laser intensity

For a low intensity of $5.7 \times 10^{13}$ W/cm$^2$, the spectrum shows 2 - 3 Å broadening with a slight blue-shift at early times indicating a Doppler effect. The spectral peak then returns to the original wavelength at the time of the incident pulse peak and finally moves to the red side. The peak red-shift may be due to the SBS which could occur around the incident peak. At an intermediate intensity of $1.5 \times 10^{14}$ W/cm$^2$, the spectral change is prominent, showing a gradual broadening to the blue side from the beginning of the pulse and a blue-shifted peak (9 Å) at the incident peak.

As will be discussed in the next section, the blue-shift peak implies a Doppler effect. This produces a blue-shift due to reflection from a moving critical density region as well as the change of the plasma density region. However the broadening around the peak (9 Å FWHM) is hardly explained by the Doppler shift, because it would give a relatively narrow spectral width such as shown at $5.7 \times 10^{13}$ W/cm$^2$ or in the spectra seen in the figure of Ref. 85. The spectrum at $1.6 \times 10^{15}$ W/cm$^2$ is similar to the preceding one, but is not as blue-shifted (1 - 2 Å) and shows further broadening (13 - 15 Å FWHM). A possible explanation for this large broadening of the specular component is the presence of a modulational instability.[58, 65] Threshold and broadening are discussed later.

Time integrated spectra were taken at 90° from a CH target oriented at 45°, using the procedures stated in Chap. III - D - (3). The scattered light in the 90° direction should contain only a specular

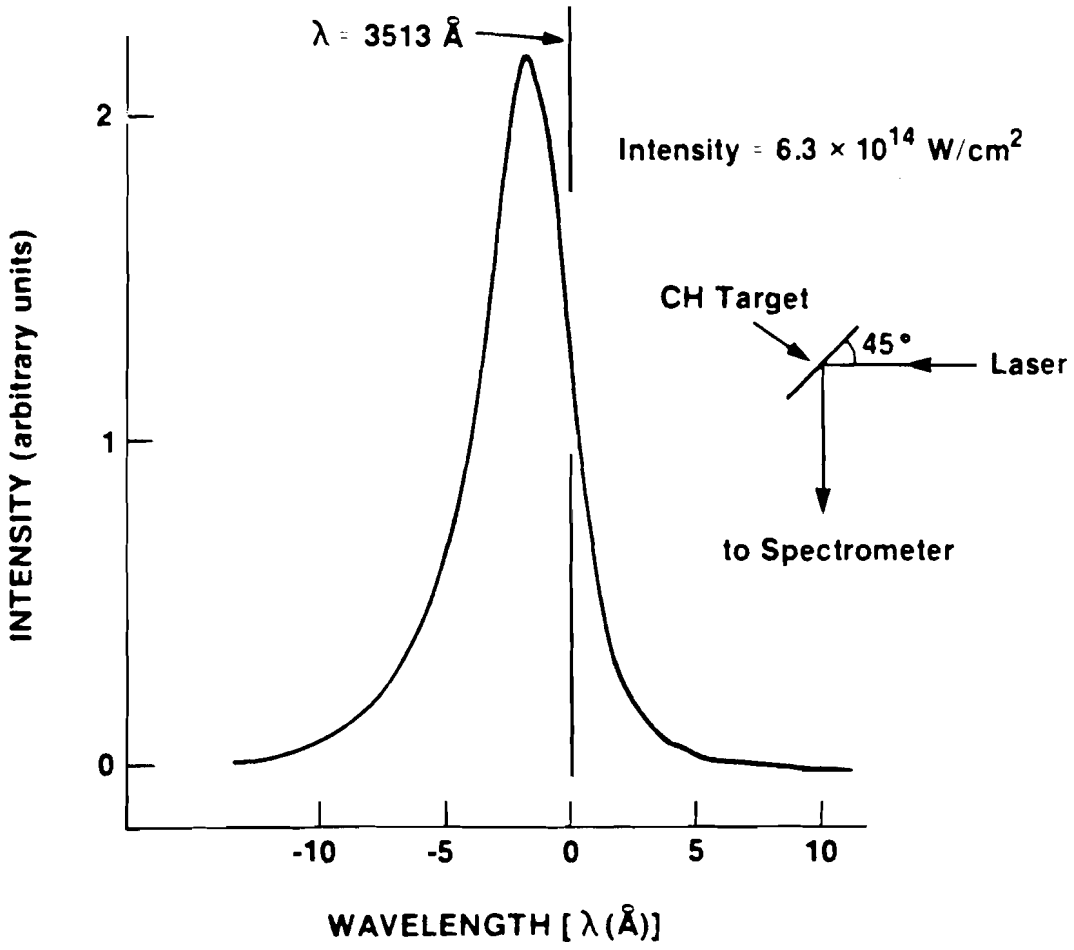


FIGURE IV-18 Time integrated spectrum at specular direction of CH 45 degree target

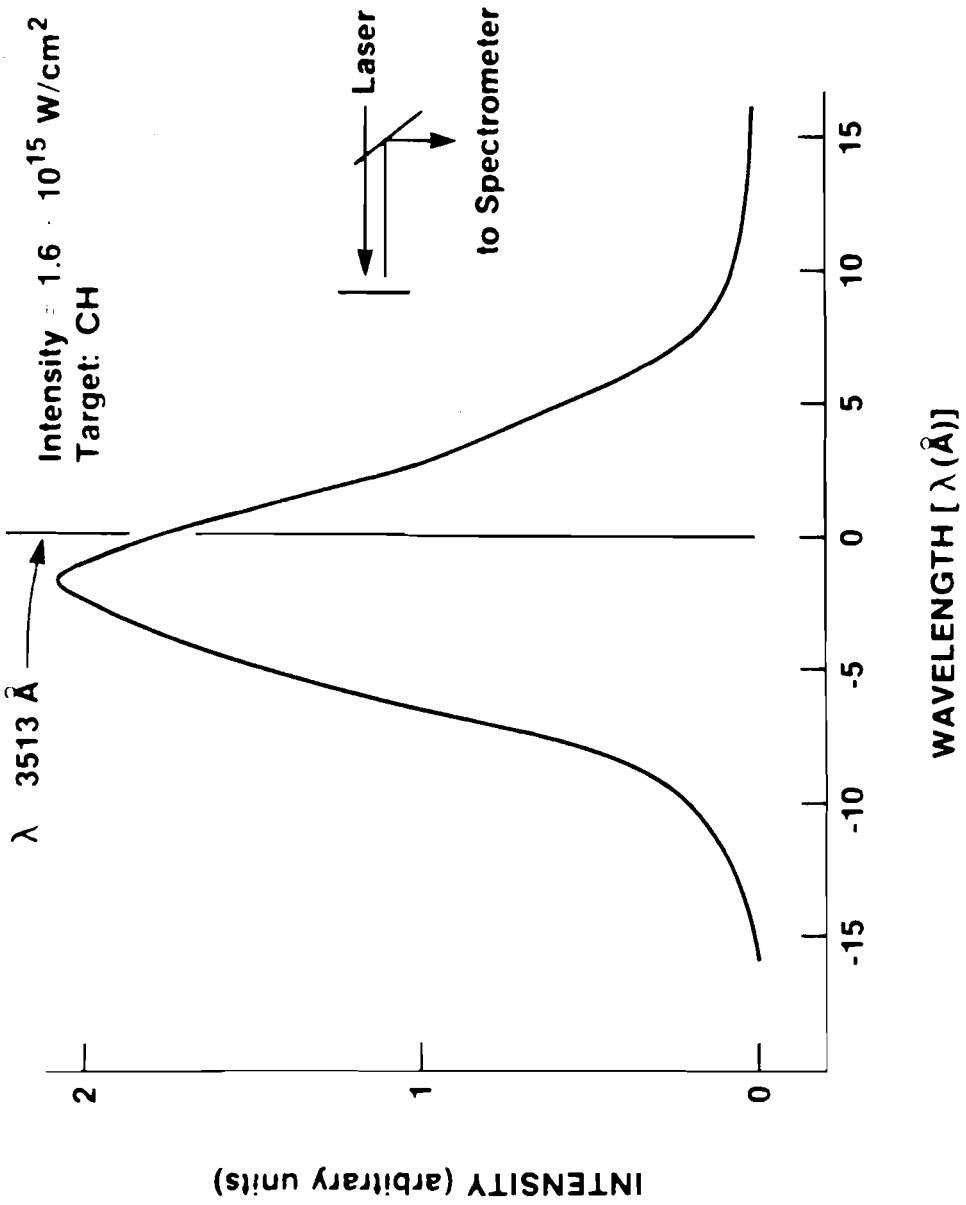


FIGURE IV-19 Time integrated backscatter spectrum of CH 0 degree target

reflection. In fact, broadened spectra were observed as in Fig. IV-18, which were similar to the ones observed in the backscatter from $0^{o}$ targets of Fig. IV-19.

At an intensity of $I_L = 6.3 \times 10^{14}$ W/cm$^2$, the specularly reflected laser light shows a symmetrical broadening. Its spectral peak is blue-shifted by 2.5 Å, and it has a spectral width of 5 Å.

In order to have simple comparison between the spectrum in this figure and the spectrum at $1.6 \times 10^{15}$ W/cm$^2$ in Fig. IV-16, the latter was cut into 100 psec time segments and the spectral intensities within the segment were added up along the time axis. This produced the approximate time integrated spectrum shown in Fig. IV-19 and showed 2.5 Å blue-shifted peak with 12 Å spectral width. Even though the backscatter spectrum was taken at 2.5 x the intensity of the specular one, a remarkable similarity in the spectral shape is seen between these two pictures. The backscatter spectrum has much larger width, consistent with higher laser intensity.

Figure IV-20 is the graph of backscattered energy (%) as a function of laser intensity. The backscattered energy here means the energy coming back through the f/12 focusing lens. The graph includes three cases: (a) target angle (TA) = 0 - $10^{o}$, pulse width (PW) = 450 psec, (b) TA $\geqq 20^{o}$, PW = 450 psec, and (c) TA = 0 - $10^{o}$, PW = 90 psec. Case (b) and (c) fall on the same line and exhibit small fractional backscatter slowly increasing with laser intensity. Case (a) is similar to the other

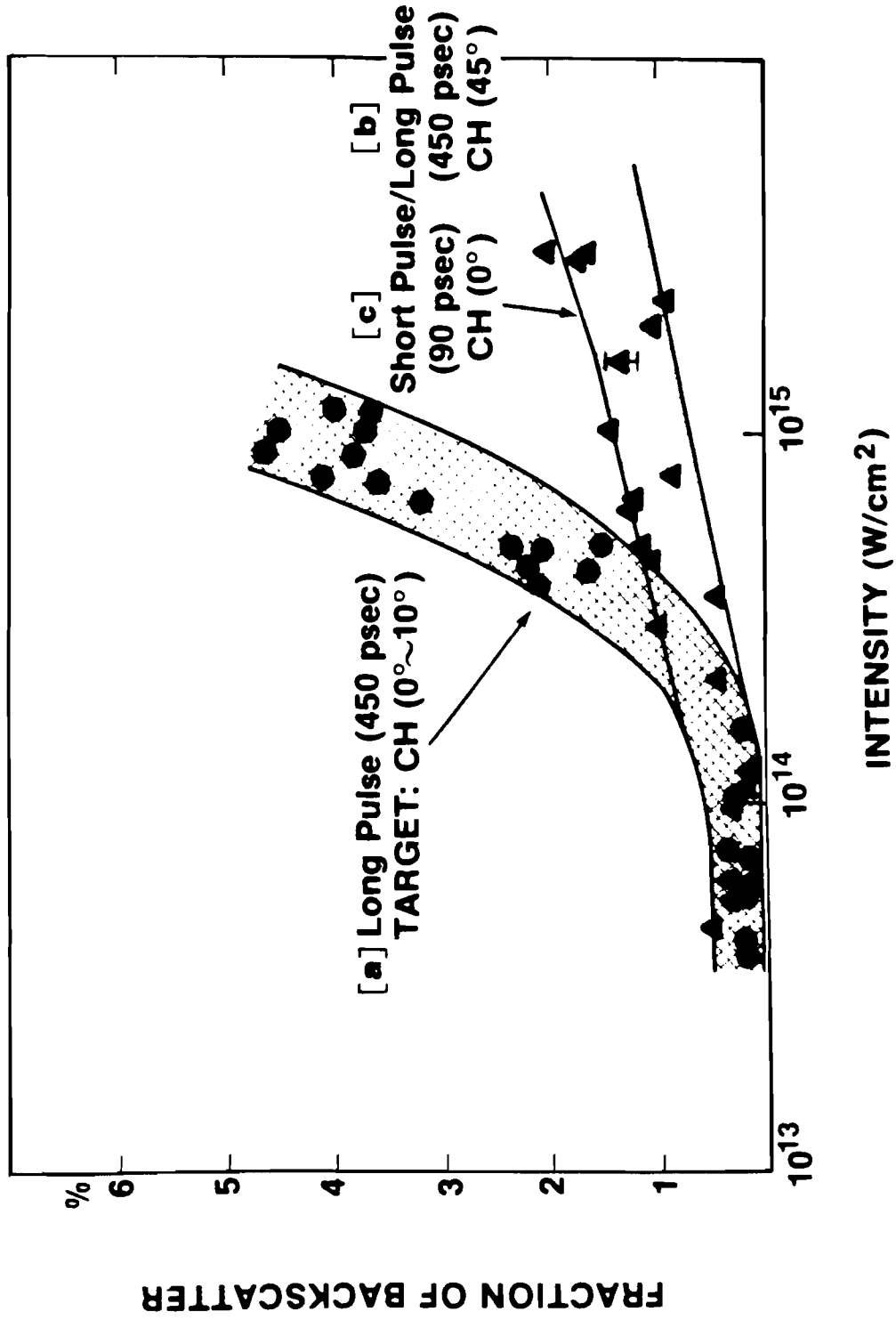


FIGURE IV-20 Backscatter energy (%) versus laser intensity

curves up to $10^{14}$ W/cm$^2$, at which point the backscatter starts increasing almost linearly with laser intensity. Curve (b) corresponds to the fractional backscatter of SBS, while curve (a) shows the backscatter, including both specular and SBS components. From this figure, SBS is seen to account for 1/3 of the total backscatter at $I_L = 2 \times 10^{15}$ W/cm$^2$.

## G. DISCUSSION : BRILLOUIN SCATTERING.

### 1. Doppler and SBS Shifts.

The red-shifted spectra in Fig. IV-13 and the strong collimation (see p 87) of the backscattered pulses were observed from the tilted targets above the laser intensity of $1 - 2 \times 10^{14}$ W/cm$^2$. These are characteristic of SBS. We compare the observed threshold value with the SBS theoretical threshold in Table II-1.

The SBS threshold in the table becomes then

$$I_{SBS} = \frac{1.72 \times 10^{12} T_e n_c}{\lambda_\mu L_\mu n_e}$$

$$= 2 \times 10^{14} \quad \text{W/cm}^2 \qquad (9)$$

for $T_e$ = 1 keV, $L_u$ = 50 μm and $n_e = 0.5\ n_c$. There is an uncertainty about the $n_e$ term, since we do not know where the SBS occurs in the plasma. Up till now no definitive experimental work has been conducted to determine the density at which SBS is most likely to occur. Thus the observed threshold value showed an approximate agreement with the SBS theoretical threshold.

Here we have used the average intensity instead of the peak intensiy as in the Raman part. We consider that the bulk of the SBS reflection occurs in the average intensiy region of the beam, not in the hot spots, since the hot spots carry little energy.[72]

As shown in Fig. IV-13, the SBS component could be differentiated from the specularly reflected laser light. Given backscatter spectra from the $0^{\circ}$ target, one may recognise the unshifted part as due to SBS, and the largely broadened blue-shifted part as a specular component. The Brillouin shift could be balanced by the blue-shift due to a Doppler effect, since the SBS occurs in the expanding plasma with a certain velocity.

First we examine the 9 Å blue-shift seen in the $0^{\circ}$ target in terms of a Doppler shift, and then evaluate the angular dependence of the Brillouin shift in Fig. IV-13. The amount of Doppler shift can be estimated by evaluating the time derivative of the phase integral[85,86]:

$$\Delta\omega = 2k_L v_c + 2k_L \frac{d}{dt}\int_{r_c}^{\infty}(1 - n)dr \qquad (10)$$

where n is the index of refraction, $v_c$ is the expansion velocity of the critical surface and $k_L$ is the vacuum wave number of the incident laser. The first term indicates the effect of the critical surface motion, while the second represents the modification of the plasma profile. According to Ref. 86, where an isothermal expansion was considered, the frequency shift due to both critical surface motion and density profile variation

variation led to

$$\frac{\Delta\lambda}{\lambda_L} \simeq 3\frac{v_c}{c} \quad , \quad (11)$$

Here $\lambda_L$ is the laser wavelength, and c is the velocity of light. In this model, $v_c$ is of the order of the ion acoustic (IA) velocity : $v_{IA}$, where

$$v_{IA} = \sqrt{\frac{Z\ T_e}{M}} \quad , \quad (12)$$

and Z,$T_e$, and M are the charge state, the electron temperature, and the ion mass. Substituting $\Delta\lambda$ for the observed value 9 Å, we have $v_c$ = 2.5 x $10^7$ cm/sec which implies $T_e$ = 1.2 keV.

Now we return to the Brillouin scattering in the flowing plasma. $\Delta\lambda$ = 9 Å could be the upper limit of a Doppler effect which contributes to the SBS, because SBS, occuring in lower density regions, may have the smaller second term in Eq. (10).

The net shift due to SBS combined with the Doppler effect leads to

$$\Delta\lambda_{NET} = \Delta\lambda_{SBS} - \cos\theta\ \Delta\lambda_{DP} \quad , \quad (13)$$

where $\Delta\lambda_{NET}$, $\Delta\lambda_{SBS}$, and $\Delta\lambda_{DP}$ are the net, the Brillouin, and the Doppler shifts.[87] $\theta$ is the incident angle of the laser light. In Eq. (12), $\Delta\lambda_{NET}$ is an experimentally determined value, while $\Delta\lambda_{SBS}$ and $\Delta\lambda_{DP}$ are unknown. We estimate $\Delta\lambda_{SBS}$ by applying a least square fit to the above equation with use of three experimental points at $\theta$ = 0, 22.5, 45° for

$\Delta\lambda_{NET}$. The net shifts used here are listed in Table IV-1 on a next page. Here we assume that the back-ground electron temperature, blow-off velocity, and plasma density where SBS takes place are not significantly different for each target angle. We have obtained $\Delta\lambda_{SBS}$ to be = 6 Å, which implies an electron temperature of $\cong$ 1.3 keV according to the following equation,

$$\frac{\Delta\lambda_{SBS}}{\lambda_L} = 2\frac{v_{IA}}{c} \propto \sqrt{\frac{Z\,T_e}{M}} \quad . \quad (14)$$

Since the Brillouin shift as well as the Doppler shift is dependent on the square root of temperature, the temperature implied from these shifts may not be accurate and should be taken as a qualitative value.

**Table IV-1.**

Net spectral centroid shift versus target angle

| $\theta$ [°] | $\Delta\lambda$ [Å] | $\cos\theta$ |
|---|---|---|
| 0 | 0 | 1 |
| 22.5 | 0.6 | 0.92 |
| 45 | 1.6 | 0.72 |

## 2. Threshold and Frequency Broadening in Modulational instability.

In Chap. IV - E, the backscattered spectra from targets oriented normal to the laser which included specular scattering, showed broadening above a cetain laser intensity. Similarly broadened spectra were observed in the specular reflection from targets tilted 45° as in Fig. IV-18, suggesting that similar process is responsible for both observations. Modulational instability seems to be an attractive candidate to explain this broadening without invoking enhanced reflection such as the case observed for the SBS.

We compare the observed threshold and the broadening with linear theory calculations in a homogeneous plasma. More detailed theory including plasma non-linearity and inhomogeneity is currently under development.[88] Frequency broadening in the specular component was observed above a laser average intensity of $1 - 2 \times 10^{14}$ W/cm$^2$, implying probable peak intensity of 4 to 5 times these values. From Table II - 1, we have the threshold form for modulational instability, $I_{MI}$ given by

$$I_{MI} = 1.67 \times 10^{15} \left(\frac{n_e}{n_c}\right) \frac{1}{\lambda_L T_e^{1/2}} \qquad (15)$$

where $n_e$ (cm$^{-3}$), $\lambda_L$ (um), and $T_e$ (eV) are the electron plasma density, the laser wavelength and the electron temperature, respectively where modulational instability occurs. $n_e = 0.8 \cdot n_c = 0.8 \times 10^{22}$, $\lambda_L = 0.35$ $\mu$m, and $T_e = 1 - 2$ keV are chosen as typical values. The temperature range

is the one suggested in Chapt. IV - C - (2) and IV - G - (1). However it remains unknown where the modulational instability occurs in the underdense region. Recalling that the spectrum of SBS has shown the order of 5 Å frequency broadening, the modulational instability, having a larger spectral width, may be considered to occur at above the plasma density of the SBS. If the SBS occurs above the density of the active region of modulational instability, the SBS spectral broadening should be at the order of the one observed for the specular component such as seen in Fig. IV-19. This seems consistent with the fact that a smaller Doppler effect has been estimated for the SBS component, compared to the one in the specularly reflected component as mentioned in Chap. IV - G - (1). This implies the Brillouin scattering is operative in a very underdense region. Even with the above arguments, the plasma density is still vague. This uncertainty could make the discussion regarding the threshold and broadening rather crude. Substituting $n_e$, $_L$, and $T_e$ for the quoted values in Eq. (15), threshold is

$$I_{MI} = 0.8 - 1.3 \times 10^{14} \text{ W/cm}^2. \qquad (16)$$

To predict the frequency broadening well above the threshold is virtually impossible in the linear theory, because the theory no longer applies, once the instability grows. However it may be able to suggest the possible modes which become unstable above this threshold.

The resulting spectral width is given in Eq. II-(61):

$$\frac{\Delta\lambda}{\lambda_L} = \frac{1}{4} \left(\frac{\omega_{pe}}{\omega_L} \frac{v_o}{v_e}\right)^2$$

Converting into a more convenient form, Eq. II-(61) becomes

$$\frac{\Delta\lambda}{\lambda_L} = 9.3 \times 10^{-14} \left(\frac{n_e}{n_c}\right) \frac{\lambda^2_L I_L}{T_e}$$

Here $I_L$ (W/cm$^2$) is the laser intensity. We observed a 9 Å broadening at a laser intensity of $I_L = 1.5 \times 10^{14}$ W/cm$^2$, and 12 - 15 Å at $1.6 \times 10^{15}$ W/cm$^2$ in the backscatter spectra as seen in Fig. IV-16. In the specularly reflected spectrum from a 45° target, a 5 Å broadening was observed at $6.3 \times 10^{14}$ W/cm$^2$ in Fig. IV-18. For a laser intensity near the threshold, $1.5 \times 10^{14}$ W/cm$^2$, we calculate $\Delta\lambda$ from Eq. (16) as

$$\Delta\lambda = 4 - 8 \text{ Å}$$

for $T_e = 1 - 2$ keV, $n_e = 0.8\ n_c$. The observed value of 9 Å is within the same order. For higher laser intensity of $1.6 \times 10^{15}$ W/cm$^2$, a possible frequency broadening becomes

$$\Delta\lambda = 40 - 80 \text{ Å}$$

This obviously disagrees with the observed value of 12 - 15 Å at the same intensity. The above frequency broadening based on the linear theory may not represent a real situatuion with non-linear saturation mechanisms, however. If pump depletion should occur, for example, the instability would not grow further, and the broadening stays unchanged. Finally for the specularly reflected light, the observed broadening is 5 Å at $6.3 \times 10^{14}$ W/cm$^2$. The calculated value becomes $\Delta\lambda = 6 - 12$ Å for n =

$0.5n_c$. For $45^o$ incidence, turning point is at $0.5n_c$, implying that incoming light might go through a less dense plasma and possibly result in a narrower frequency broadening due to modulational instability. A lower electron density raises threshold of the instability. These points may be consistent with the observed narrower broadening.

## H. CONCLUSION: BRILLOUIN SCATTERING

In the backscattered spectra, two components were identified clearly: a SBS and a specular component. Tilted targets experiments showed strongly collimated backscattered beams, whose spectra were red-shifted (1 - 3 Å) above a laser intensity of $2 \times 10^{14}$ W/cm$^2$. We attributed this component to SBS. The gradual increase of the red-shifts with target angle were consistent with the SBS from a flowing plasma with Mach 1 and a temperature of 1.2 keV.

The spectral peak blue-shift (9 Å) seen for the $0^{\circ}$ target at an intensity of $2 \times 10^{14}$ W/cm$^2$ was consistent with a Doppler effect in the plasma of a temperature 1.2 keV.

A specular component from the the $0^{\circ}$ targets showed the unusual spectral broadening around the blue-shifted peak. Similar broadening was observed for the specular component from the $45^{\circ}$ target. The linear theory of modulational instability in a homogeneous plasma accounted for the observed threshold of $1 - 2 \times 10^{14}$ W/cm$^2$ and frequency broadening of 9 Å near the threshold.

## V. SUMMARY

To complete this thesis, we summarize the results and discuss the significance of the results that we obtained through our experiments. We then present several suggestive remarks for further development of this work.

Theory has predicted three possible parametric instabilities: $2\omega_{pe}$ and, absolute and convective Raman instabilities at and below the quarter critical density region in a plasma, while no experimental work had clearly detected and separated these different phenomena. Our observations of these instabilities in U.V. laser produced plasmas showed clear threshold and saturation behavior. The $2\omega_{pe}$ instability was characterized by depolarization of $\omega_L/2$ light, which was postulated to occur from the two stage processes (see p 63). Both absolute and convective Raman instabilities showed strong polarization dependence in their spectra. The absolute Raman instability gave rise to scattered light at $\omega_L/2$, while the spectrum for convective Raman was between 4500 and 6200 Å. The measured saturated level of the scattered light at $\omega_L/2$ was found to be exceedingly small ($6 \times 10^{-6}$ of incident energy) under current experimental conditions. The experimental and theoretical verification of saturation mechanisms are imcomplete. These

instabilities occured in the hot spots of the laser (see p 67). Intensities there were, in fact, 4 - 5 times higher than the average intensity in the focal spot. It is important to investigate the behavior of the instabilities when the average intensity exceeds the threshold values.

Comparison between observed and theoretical thresholds indicated a density steepening near $n_c/4$. This could be due to the pondermotive force of electrostatic waves resonantly driven by the instabilities. Analyzing the experimental threshold values, the effective density scale lengths were found to be longer than those predicted from hydro-code calculations. These longer scale lengths may come from plateau regions caused by density modulations. These modulations could be formed in higher density regions and thus may propagate down the density gradient. This condition may cause the "flickering" of the instabilities, which could be measured by temporally resolving the scattered light spectrum.

SBS has been shown to be dangerous in infrared laser-plasma experiments. Since absorption was considerably higher (80 - 90 % at laser intensities of $10^{14}$ - $10^{15}$ W/cm$^2$) than the previous experiments at 1.06 um, the total amount of reflection was consequently smaller. The total backscatter was only 6 % of the incident energy at $10^{15}$ W/cm$^2$. SBS was found to be responsible for 1/3 of the backscatter, while the rest was due to specular reflection. The specular component showed a characteristic broadening above a threshold intensity of 1 - 2 x $10^{14}$ W/cm$^2$. We attributed these effects to modulational instability.

## REFERNCE


1. G.S. Fraley, E.J. Linnerbur, R.J. Mason, R.L. Morse, Phys. Fluids, 17, 474(1974)
2. J. Nuckolls, L. Wood, A. Thiessen, G. Zimmerman, Nature, 239, 135(1972)
3. N.G. Basov, O.N. Krokhim, Sov. Phys. JETP, 19, 123(1964); J.M. Dawson, Phys. Fluids, 7, 98(1964)
4. J.D. Lawson, Proc. Phys. Soc(London), B70, 6(1957)
5. J.R. Albritton, I.B. Bernstein, E.J. Valeo, E.A. Williams, Phys. Rev. Lett., 39, 1536(1977); D.W. Forslund, J.M. Kindel, K. Lee, E.L. Lindman, R.L. Morse, Phys. Rev. A., 11, 679(1974)
6. K. Estabrook, W.L. Kruer, Phys. Rev. Lett., 40, 42(1978); C.M. Armstrong, B.H. Ripin, F.C. Young, R. Decoste, R.R. Whitlock, S.E. Bodner, J. Appl. Phys., 50, 5233(1979); G.D. Enlight, M.C. Richardson, N.H. Burnett, ibid., 50, 3909, (1979)
7. D.T. Attwood, N.M. Ceglio, E.M. Campbell, J.T. Larsen, D.M. Mathews, S.L. Lane, UCRL-83541, 1980(unpublished); B. Yaakobi, D. Steel, E. Thorsos, A. Hauer, B. Perry, S. Skupsky, J. Geiger, C.M. Lee, S. Letzering, J. Rizzo, T. Mukaiyama, E. Lazarus, G. Halpern, H. Deckman, J. Delttrez, J. Soures, R.L. McCrory, Phys. Rev. A., 19, 1247(1979).
8. J.H. Orens, NRL, Report No.4167, 1980(unpublished).
9. C.E. Max, C.F. Mckee, W.C. Mead, UCRL-84019, 1980(unpublished).
10. V.L. Ginzburg, The Propagation of Electromagnetic Waves in Plasmas (Pregamon Press, 1970, NY).

11. F. Amiramoff, R. Benttar, R. Fabbro, E. Fabre, C. Garban, C. Popovics, J. Virmont, M. Weinfeld, Bull. Amer. Phys. Soc.24, 1069(1979); W. Seka, R.S. Craxton, J. Delettrez, L. Goldman, R. Keck, R.L. McCrory, D. Shvarts, J.M. Soures, R. Boni, to be published in Opt. Commun.

12. J.M. Soures, L.M. Goldman, M.C. Richardson, W. Seka, K. Tanaka, R. Bingham, E.A. Williams, Bull. Amer. Phys. Soc. 26, 970(1981)5U7.; L.M. Goldman, M.C. Richardson, W. Seka, K. Tanaka, R. Bingham, E.A. Williams, ibid., 26, 848(1981)1E10; T. Boehly, L.M. Goldman, M.C. Richardson, W. Seka, ibid.26, 848(1981)1E7; R. Keck, R.S. Craxton, L.M. Goldman, W. Seka, ibid., 26, 848(1981)1E9.

13. L.M. Goldman, J. Soures, M.J. Lubin, Phys. Rev. Lett., 31, 1184(1973)

14. C. Yamanaka, T. Yamanaka, T. Sasaki, J. Mizui, H.B. Kang, ibid., 32, 1038(1974)

15. B.H. Ripin, J.M. McMahon, E.A. McLean, W.M. Manheimer, J.A. Stamper, ibid., 33, 634(1974)

16. E. Jannit, A.M. Malvezzi, G. Tondello, J. Appl. Phys., 46, 3096(1975)

17. E.A. Burnov, G.M. Malyshev, G.T. Razdobarin, V.V. Semenov, I.P. Folomikin, Sov. Phys. JETP, 41, 55(1975)

18. K.B. Mitchel, T.F. Stratton, P.B. Weiss, Appl. Phys. Lett., 27, 11(1975)

19. T.P. Donaldson, M. Hubbard, I.J. Spalding, Phys. Rev. Lett., 37, 1348(1976)

20. J.J. Turechek, F.F. Chen, ibid., 36, 720(1976)

21. A.A. Offenberger, M.R. Cervenan, A.M. Yam, A.W. Pasternak, J. Appl. Phys., 47, 1451(1976)

22. R. Sigel, K. Eidmann, H.C. Pant, P. Sachsenmaier,
Phys. Rev. Lett., 36, 1369(1976)

23. B. Grek, H. Ripin, F. Rheault, ibid., 38, 898(1977)

24. D.W. Phillion, W.L. Kruer, V.C. Rupert, ibid., 39, 1529(1977)

25. R.A. Haas, W.C. Mead, W.L. Kruer, D.W. Phillion, H.N. Kornblum,
J.D. Lindl, D. MacQuigg, V.C. Rupert, K.G. Tirsell,
Phys. Fluids, 20, 322(1977)

26. B.H. Ripin, F.C. Young, J.A. Stamper, C.M. Armstrong,
R. Decoste, Phys. Rev. Lett., 39, 611, (1979)

27. H.D. Shay, R.A. Hass, W.L. Kruer, M.J. Boyle, D.W. Phillion, V.C. Ruppert,
H.N. Kornblum, F. Rainer, V.W. Silvinsky, L.N. Koppel, L. Richards,
K.G. Tirsell, Phys. Fluids, 21, 1634(1978)

28. L.M. Gorbunov, YuS. Kas'nov, V.V. Korbukin, A.N. Polyanichev,
A.P. Shevel'ko, JETP. Lett. 27, 226(1978)

29. K. Eidman, G. Brederlow, R. Brodmann, R. Petsch, R. Sigel, G. Tsakiris,
R. Valk, S. Witkowski, J. Phys. D., 12, L145(1979)

30. N.G. Basov, V.A. Boiko, V.A. Danilychev, V.D. Zvorykin, I.V. Kholin,
A.Yu. Chugunov, Sov. J. Plasma. Phys. 5(4), 407(1979)

31. A. Ng, L. Pitt, D. Salzmann, A.A. Offenberger,
Phys. Rev. Lett., 42, 307(1979)

32. M.J. Herbst, C.E. Clayton, F.F. Chen, ibid., 43, 1591(1980)

33. M.D. Rosen, D.W. Phillion, V.C. Rupert, W.C. Mead, W.L. Kruer, J.J. Thomson,
H.N. Kornblum, V.W. Slivinsky, G.J. Caporaso, M.J. Boyle, K.G. Tirsell,
UCRL-82146, 1979(unpublished)

34. B.H. Ripin, E.A. McLean, NRL.Report-3964, 1979(unpublished)

35. M.J. Herbst, C.E. Clayton, W.A. Peables, F.F. Chen,

Phys. Fluids, 23, 1319(1980)

36. H.E. Huey, A. Mase, N.C. Luhmann, W.F. DiVergilio, J.J. Thomson, Phys. Rev. Lett., 45, 795(1980)

37. S. Jackel, H.M. Loebenstein, A. Zigler, H. Zmora, S. Zweigenbaum, Appl. Phys. Lett., 36, 34(1980)

38. R.H. Lehmberg, K.A. Holer, Phys. Rev. A, 22, 2156(1980)

39. R. Turner, L.M. Goldman, Phys. Rev. Lett., 44, 400(1980)

40. L.L. Turechek, F.F. Chen, Phys. Fluids, 24, 1126(1981)

41. A. Ng, A.A. Offenberger, S.J. Karttunen, Opt. Commun.36, 200(1981)

42. R. Turner, L.M. Goldman, Phys. Fluid, 24, 184(1981)

43. K. Tanaka, L.M. Goldman, Phys. Rev. Lett. 45, 1558(1980)

44. J. Handke, S.A.H. Rizvi, B. Koronast, Appl. Phys. 25, 109(1981)

45. K.G. Estbrook, W.L. Kruer, B.F. Lasinski, A.B. Langdon, Phys. Fluids, 23, 1326(1980)

46. D.W. Phillion, D.L. Banner, UCRL-84854, 1980(unpublished)

47. R.G. Watt, R.D. Brooks, Z.A. Pietrzyk, Phys. Rev. Lett., 41, 170(1978)

48. N.A. Ebrahim, H.A. Baldis, C. Joshi, R. Benesch, ibid., 45, (1980)

49. E.A. Jackson, Phys. Rev. 153, 235(1966)

50. K. Nishikawa, J. Phys. Soc. Jap, 24, 916(1968)

51. M.N. Rosenbluth, Phys. Rev. Lett., 29, 565(1972)

52. C.S. Liu, M.N. Rosenbluth, R.B. White, ibid., 31, 697(1973)

53. M.N. Rosenbluth, R.B. White, C.S. Liu, ibid., 31, 1190(1973)

54. C.S. Liu, M.N. Rosenbluth, R.B. White, Phys. Fluids, 17, 1211(1974)

55. J.F. Drake, P.K. Kaw, Y.C. Lee, G. Schmidt, C.S. Liu, M.N. Rosenbluth ibid., 17, 778(1974)

56. D.W. Forslund, J.M. Kindel, E.L. Lindman, ibid., 18, 1002(1975)

57. P.K. Kaw, W.L. Kruer, C.S. Liu, K. Nishikawa in Advances in Plasma Physics ,
edited by A. Simon and W.B. Thompson (Wiley, N.Y. 1976), vol. 6.

58. R. Bingham, Nonlinear Laser-Plasma Interactions , Ph D. thesis, 1977 Oxford University (1977)

59. L. Landau, J. Phys X, 25(1946); J. Dawson, Phys. Fluids, 17, 869(1961); T. O'Neil, ibid., 8, 2255(1965)

60. J. Albritton, P. Koch, Phys. Fluids, 18, 1136(1975)

61. K. Etabrook, W.L. Kruer, B.F. Lasinski, Phys. Rev. Lett., 45, 1399(1980)

62. B. Lasinski, K. Estabrook, W.L. Kruer, B. Langdon,
UCRL-84827, 1980(unpublished)

63. C.E. Max, K.G. Estabrook, Comments.
Plasma Phys. Cont. Fusion. 5, 253(1980)

64. C.L. Tang, J. Appl. Phys.37, 2945(1966)

65. R. Bingham, C.N. Lashmore-Daies, Nucl. Fusion. 16, 67(1976)

66. W. Seka, J.M. Soures, S.D. Jacobs, L.D. Land, R.S. Craxton,
IEEE-J, Quantum Electron.QE-17, 1689(1981)

67. W. Seka, LLE, University of Rochester (private communication)

68. Polarized Light, Polaroid Corp. 1978(unpublished)

69. N.H. Schiller, R.R. Alfano, Opt. Commun. 35, 451(1980)

70. Yardeley Beers, Introduction to the theory of Error (Addison-Wesley Publishing Company, USA, 1962)

71. Pin Cusion Distortion, M. Born and E. Wolf, Principles of Optics, p217 (Pergamon Press, NY, 1975)

72. W. Seka, LLE, University of Rochester (private communication)

73. J. Delletrez, LLE, University of Rochester (private communication)

74. M.C. Richardson, L.M. Goldman, W. Seka, J.M. Soures, K. Tanaka, R. Bingham, E. Williams, Bull. Amer. Phys. Soc. 26, 955(1981)5G2

75. R.W. Means, L. Mushietti, M.Q. Tran, J. Vaclavik, Phys. Fluids, 24, 2197(1981)

76. S.J. Karttunen, Phys. Rev. A, 23, 2006(1981)

77. E.A. Williams, R. Bingham, R. Short, Bull. Amer. Phys. Soc. 26, 863(1981)1U21

78. J.M. Stone, Radiation and Optics, p460(McGraw Hill, NY, 1963)

79. H.A. Baldis, J.C. Samson, P.B. Corkum, Phys. Rev. Lett., 41, 1719(1978)

80. K. Mizuno, D.A. Rasmussen, J.S. DeGroot, W. Woo, B. Till, Bull. Amer. Phys. Soc. 26, 861(1981)

81. A.B. Langdon, B.F. Lasinski, W.L. Kruer, Phys. Rev. Lett., 43, 133(1979)

82. R.S. Craxton, LLE, University of Rochester (private communication)

83. B. Yaakobi, T. Boehly, P. Bourke, Y. Conturie, R.S. Craxton, J. Delletrez, J.M. Forsyth, R.D. Frankel, L.M. Goldman, R.L. McCrory, W. Seka, D. Shvarts, J.M. Soures, Opt. Commun. 39, 175(1981)

84. W. Seka, R.S. Craxton, J. Delletrez, L.M. Goldman, R. Keck, R.L. McCrory, D. Shavarts, J.M. Soures, R. Boni Opt. Commun. 40, 437(1982)

85. J.A. Tarvin, R.J. Schroeder, Phys. Rev. Lett., 47, 341(1981)

86. T. Dewandre, J.R. Albritton, E.A. Williams, Phys. Fluids, 24, 528(1981)

87. M.D. Rosen, D.W. Phillion, V.C. Rupert, W.C. Mead, W.L. Kruer, H.N. Kornblum,V.W. Slivinsky, G.J. Caporaso, M.J. Boyle, K.G. Tirsell. J.J. Thomson, ibid., 22, 2020(1979)

88. R. Bingham, Rutherford Laboratory, Oxon, UK (private communication)

## APPENDIX 1.

We derive the wavelength of refractive cut-off shown in Fig. IV-4. Raman scattered light generated at or below the quarter critical region is refracted, when it is coming out of a plasma. If we observe the backscattered Raman light from an angled target, we should see the cut-off due to this refractive effect on the longer wavelength side of the spectrum. This is seen in the figure. To estimate the cut-off wavelength, we use the dispersion relations of an electromagnetic wave both in a plasma and vacuum, assuming one dimensional plasma. The maximum refraction for the Raman scattered light is expected, when the light has only $\underline{k}$ vector (k:wavenumber) component perpendicular to a density gradient. The dispersion relation is given by

$$\omega_R^2 = \omega_{pe}^2 + c^2 k_\perp^2 , \qquad (1)$$

where $\omega_R$ is the frequency of a Raman scattered light, and $k_\perp$ is the wave vector component perpendicular to the density gradient.

After the refraction, the dispersion relation of the light at an observing point (vacuum) becomes

$$\omega_R^2 = c^2 k_{/\!/}^2 + c^2 k^2 = c^2 k_\perp^2 , \qquad (2)$$

where $k_{//}$ is the parallel component of the wave vector to the density gradient. Cosine of the cut-off angle for the Raman light is

$$\cos\theta = k_{//}/k \qquad (3)$$

Using Eq. (1) and (2), Eq. (3) can be modified to

$$\cos\theta = \omega_{pe}/\omega_R \qquad (4)$$

To relate an incident laser and the Raman scattered light wavelength in the above equation, we use a frequency matching condition for SRS ($\omega_L = \omega_R + \omega_{pe}$) and obtain

$$\cos\theta = \frac{\omega_L - \omega_R}{\omega_R} \quad , \qquad (5)$$

where $\omega_L$ is the laser wavelength.

Now Eq. (5) can be re-written in terms of the laser wavelength as:

$$\lambda_{SRS} = \lambda_L(1 + \cos\theta) \, . \qquad (6)$$

## APPENDIX 2.

The purpose in this section is to compare a film detection level and energy density emitted from a black body (BB) in the Rayleigh-Jeans limit,[78] and estimate our detection threshold.

In order to proceed to further calculation, we need to define the following terms:

$E_{BB}$ = total energy emitted at target (J)

$e_{BB}$ = BB energy density ($J/cm^2$)

$I_{BB}$ = BB spectral brightness ($W/cm^2$)

$= 2c(kT)\lambda^{-4}$,

where c is the speed of light ( = $3 \times 10^{10}$ [cm/sec] ), k is the Boltzman constant ( = $1.6 \times 10^{-12}$ [ erg/eV ] ), and $\lambda$ is the wavelength (cm).

$\Delta\Omega$ = solid angle defined by the f/12 focus lens.

$= 5.45 \times 10^{-3}$

$\alpha$ = transmission rate through the optical system

$A_F$ = focus spot area on target.

$= 7.85 \times 10^{-5}$ ($cm^2$)

$A_{F'}$ = focus area of transmitted BB light on spectrometer slit

$= 1.96 \times 10^{-1}$ $(cm^2)$.

$h_s$ = spectrometer slit height.

$w_s$ = spectrometer slit opening width = 25 $(\mu m)$.

$\Delta\lambda$ = spectral resolution

$= 10$ $(\text{Å})$

$w_{disp}$ = dispersion width of $\Delta\lambda$ by the grating

$= \Delta\lambda \times$ (dispersion of the grating)$^{-1}$

$= 10$ $(\text{Å}) \times (0.25$ $[\text{Å}/\mu m]$ $)^{-1}$

$= 40 (\mu m)$.

$e_{spec}$ = energy density of BB at the input slit of the spectrometer $(J/cm^2)$.

$e_{FLM\text{-}BB}$ = energy density of BB at a film plane $(J/cm^2)$

$e_{FLM}$ = film energy density required for an O.D. = 0.3 signal at $\lambda = 4800$ $(\text{Å})$

$= 5 \times 10^{-9}$ $(J/cm^2)$

We are going to follow the emitted light energy at target, transmitting through an optical system, focused on a spectrometer input slit. The light going into a spectrometer disperses its energy after a grating, then is sent to a camera film plane. As a first step, BB energy density at target is expressed as:

$$e_{BB} = I_{BB}\, \Delta\lambda\, \Delta T\, \Delta\Omega \qquad (1)$$

$$= 2c(kT)^{-4} \Delta\lambda\, \Delta T\, \Delta\Omega \qquad (1')$$

Here we use the temperature = 1 - 2 (keV), the spectral resolution $\Delta\lambda$ = 10 $(\text{Å})$ the pulse width $\Delta T = 450 \times 10^{-12}$ (sec), the wavelength of the

observed spectral peak $\lambda$ = 4800 (Å), and the solid angle of the f/12 focus lens $\Delta\Omega = 5.5 \times 10^{-3}$. After substituting these values in Eq. (1), we have

$$e_{BB} = 1 - 2 \times 10^{-6} \qquad (2)$$

Using the focusing area $A_F$ as a BB emission region, the total BB emitting energy becomes

$$E_{BB} = A_F \, e_{BB} \qquad (3)$$

When this BB energy, $E_{BB}$ is focussed onto the input slit of a spectrometer after transmitting the optical system with the loss factor $\alpha$ , the BB energy density at th input slit, $e_{spec}$ is given by:

$$e_{spec} = E_{BB} \times \alpha \times \frac{1}{A'_F} = \alpha \frac{A_F}{A'_F} \cdot e_{BB} \qquad (4),$$

where $A_{F'}$ is the focused area on the slit. Dispersed by the grating in a spectrometer, the energy density at a film plane is,

$$e_{FLM-BB} \equiv e_{spec} \times \frac{h_s w_s}{h_s (w_s + w_{disp})} \qquad (5),$$

where $h_s(w_s + w_{disp})$ is the dispersed area for $\Delta\lambda$ , and $h_s w_s$, the input slit area. Using $\alpha$ = 0.35, $A_{F'} = 2.0 \times 10^{-1}$, $w_s/(w_s + w_{disp})$ = 25/65, Eq. (5) now becomes,

$$e_{FLM-BB} = 7 - 14 \times 10^{-11} \quad J/cm^2 \qquad (6).$$

For the film used in this experiment, it requires $5 \times 10^{-2}$ $(erg/cm^2)$ (or $5 \times 10^{-9}$ $[J/cm^2]$) to have optical density (O.D.) = 0.3 as shown in Fig. III-3, Chap. III. Namely the required energy density $e_{FLM}$ for the film is

$$e_{FLM} = 5 \times 10^{-9} \quad J/cm^2 \qquad (7)$$

Thus the ratio of the film sensitivity $e_{FLM}$ to the BB thermal level at = 4800 A at a film plane, $e_{FLM\text{-}BB}$ is,

$$\frac{e_{FLM}}{e_{FLM\text{-}BB}} = 70 - 140 \qquad (8)$$

A realistic detection level may be half of the above value, because $e_{FLM}$ is the energy density for O.D. = 0.3, which corresponds approximately to a factor 2 for normal film response as O.D. = log E (E: exposed energy on film).

In the procedure so far, we have used several terms which may not be determined uniquely. For example $e_{FLM}$ at 5000 ± 200 (Å) is a sensitive function of the wavelength and can vary from $5 \times 10^{-9}$ $J/cm^2$ to $2 \times 10^{-8}$ $J/cm^2$, depending on the spectral peak position. Fluctuations of ± 200 Å in the spectral peak position were typically observed. Another possible uncertainty is the reciprocity failure of the film. When a very short time exposure is taken as in the present case ($\cong 10^{-9}$ sec), more energy flux may be required to obtain an equivalent O.D. in the case of longer exposure time. These factors could conceivably increase the number in

Eq. (8) by more than a factor of 6.

## ACKNOWLEDGEMENT

It is a great pleasure to express gratitude to the author's supervisor, Prof. L.M. Goldman, for his excellent guidance and sincere friendship throughout his research. The author is indebted to many colleagues in the Laboratory for Laser Energetics for their invaluable help. Especially he is grateful to R. Bahr, T. Boehly, R. Boni, J. Cooledge, R. Keck, T. Kessler, B. Flaherty, and Dr. S. Letzring. He acknowledges with thanks Dr. W. Seka for his precise guidance and suggestions. Without Dr. W. Friedman's help, some of data could not have been processed efficiently. He is indebted to Drs. E. Williams, R. Bingham, and R. Short for stimulating discussions and deep interest. He wishes to thank Drs. J. Soures and M.C. Richardson for their encouragement. He would like to express his appreciation to Drs. E. Thorsos and T. Kataoka for their friendship. He appreciates the careful reading of this work by B. Afeyan and B. Boswell.

For the deep understanding and encouragement by his parents, Kan'ichi and Sumiko Tanaka, he is most indebted.

# PARAMETRIC INSTABILITIES

# IN

# U.V. LASER-PRODUCED PLASMAS.

by

Kazuo Tanaka

Submitted in Partial Fullfilment

of the

Requirements for the Degree

DOCTOR OF PHILOSOPHY

Supervised by Professor Leonard M. Goldman

Department of Mechanical Engineering

College of Engineering and Applied Science

University of Rochester

Rochester, New York

1982